Group 12 metal chalcogenides as single source molecular precursors for the preparation of metal sulfide nanoparticles

By

OSUNTOKUN JEJENIJA (200907706)

B.Sc Chemistry (Ibadan), B.Sc (Hons) Chemistry (UFH)

Being a dissertation submitted to the Faculty of Science and Agriculture in fulfillment of the requirement for the award of degree of

Master of Science in Chemistry

of the

University of Fort Hare

Supervisor: Professor P. A. Ajibade

Department of Chemistry

University of Fort Hare

Private Bag X1314

Alice 5700

South Africa

January 2013

CERTIFICATION

This is to certify that this thesis is a record of original research carried out by Jejenija OSUNTOKUN under my supervision at the Department of the Chemistry, Faculty of Science and Agriculture, University of Fort Hare, South Africa in fulfillment of the requirement for the award of Masters of Science degree in Chemistry.

_____ _____

Date

Supervisor

Prof. P. A. Ajibade

BSc (Hons), MSc (Ibadan),

PhD (UZ), MRSC (London)

DEDICATION

To the memory of my late, father, Tomori Olawobi Moses Osuntokun

ACKNOWLEDGEMENTS

My sincere appreciation goes to almighty God who is the author and finisher of my faith, the "I am that I am" and the king of glory. He ordered my steps because he knows the best for me and I will forever be grateful. My deepest gratitude goes to my supervisor, Prof Peter A. Ajibade for this opportunity given to me to study for this degree and his approach to hard work. I pray that God will bless him beyond his imaginations. I am indebted to some of my colleagues in the laboratory although they graduated while I was still doing my research work however; they have made some contributions towards my experience in academics. Their names are; Dr Onwudiwe Damian, Dr Adewale Adeloye and Omoruyi Uyi gold.

In life one cannot but interact with people in his field or around him and on this note I want to appreciate the following people for their encouragements and contributions in my pursuit of this degree, there are; Dr David Katwire, Dr Tichagwa Lilian, Dr Yemi Oyedeji and Dr Mopelola Idowu. My heartfelt gratitude goes to my lovely younger sister; Mrs Temidola Obinomen and Tolulope Akinrogunde. They have been very supportive in their different capacities and they gave me a lot of encouragements. To my other siblings, Tanwa Osuntokun and Damilola Osuntokun I am sincerely grateful for their support and assistance too. They have been able to fill the vacuum created by my absence from home and that in itself has helped me a lot. During the course of this research I met guys like Mr Bhunu, Mr Nwamadi Mutshiyalo and Mr Vala they

were quite good to me and they were ever supportive in teaching me some basic things on computer skills. I wish to appreciate my mum Mrs Bimpe Osuntokun for her prayers, frequent calls, patience with me and her prayer points sent via phone. I am indeed very grateful for her understanding and support. To my late dad, I am sincerely grateful for the training he gave me, his advice of keeping something for a raining day and his preachings of being one's brother keeper. He is gone now but the memory of his good works lives in me. I am highly indebted to Govan Mbeki Development Centre (GMRDC) for their financial support and I pray that this initiative, for a long time will be sustainable. I will want to leave two quotes that I stumble upon in the course my research. "Too often we underestimate the power of a touch, a smile, a kind word, a listening ear, an honest compliment, or the smallest act of caring, all of which have the potential to turn a life around." Leo Buscaglia.

"I consider my ability to arouse enthusiasm among men the greatest asset I possess. The way to develop the best that is in a man is by appreciation and encouragement." Charles M. Schwab. Finally, and again I am very grateful to almighty God in an innumerable measure for his unconditional love, protection and favour. I must confess that I have experienced some hard times in the course of this study but his grace has sustained me all through.

Table of content

List of Figures

List of Tables

LIST OF ABRREVIATIONS

Chemical reagents

HDA	hexadecylamine
TOPO	tri-n-octylphosphine oxide
TOP	tri-n-octylphosphine
mtu	methylthiourea
dmtu	dimethylthiourea
detu	diethylthiourea
ecda	1-ethoxylcarbonyl-1-cyanoethylene- 2,2- dithiolate
tmtd	tetramethylthiuram disulfide

Intrumentation

IR	infrared spectroscopy
NMR	nuclear magnetic resonance spectroscopy
SEM	scanning electron microscopy
TEM	transmission electron microscopy
EDX	energy dispersive X-ray spectroscopy
TGA	thermogravimetry analyser
XRD	X-ray diffraction
XPS	X-Ray photoelectron spectroscopy
PL	photoluminescence
SAD	selected-area diffraction

UHV	ultra high vacuum
LEDs	light emitting diodes
OD	zero dimensional
1D	one dimensional
2D	two dimensional
3D	three dimensional
LAPW	linear augmented plane wave
NMTO	new generation muffin–orbital
COHP	crystal orbit hamilotonia population
TB	tight binding
ESCA	electron spectroscopy for chemical analysis
Eg	the bang gap of the material
α	absorption coefficient
n	depends on the type of trasition
A	constant
$h\nu$	photon energy
E_k	photo electron
ϕ	work function
m	Electron mass
q	Electron charge
v	Potential difference
h	Planks constant

λ	Effective electron wavelengh

Abstract

Twelve Zn(II), Cd(II) and Hg(II) complexes of mixed ligands: alkyl thiourea, 1-ethoxylcarbonyl-1-cyanoethylene-2,2-dithiolate and tetramethylthiuram disulfide were synthesized by the reaction between the ligands and the respective metal salts. The compounds were characterized by elemental analysis, infrared (IR), ^{1}H- and ^{13}C-NMR spectroscopy. Four coordinate geometries were proposed for the compounds based on elemental and spectroscopic analyses. The metal complexes were at best sparingly soluble in polar coordinating solvents such as DMSO and DMF and insoluble in most organic solvents. This makes it practically impossible to grow single crystals suitable for X-ray crystallographic analysis and also resulted in extremely poor ^{13}C-NMR spectra for some of the complexes. Thermogravimetric analysis on some of the complexes showed that they decomposed to their respective metal sulfides and thus suitable as single molecular precursors for the preparation of metal sulfide nanoparticles.

Nine of the complexes with good yield were thermolysed and used as single source precursors to synthesized hexadexylamine capped metal sulfide nanoparticles. The optical and structural properties of the nanoparticles were studied using UV-Visible, photoluminescence (PL), scanning electron microscopy (SEM), transmission electron microscopy (TEM), powder X-ray diffraction (XRD) and energy dispersive spectroscopy (EDX). The absorption and emission spectra of the nanoparticles show quantum confinement. The SEM showed the morphology of the particles as nearly spherical, the EDX spectra revealed peaks corresponding to respective metal and sulfur with traces of contaminants being phosphorus from tri-n-octylphosphine (TOP).

The TEM micrograph showed that particles were in nanometer regime with sizes ranging from 10-25 nm. The XRD was used to establish the nanoparticles crystalline phases and patterns are consistent with predominately hexagonal phase for ZnS while the CdS and HgS exhibited cubic phase nanoparticles. The broad peak pattern indicated the formation of small nanocrystals.

CHAPTER ONE

1. INTRODUCTION

1.1 Introduction

The National Nanotechnology Initiative (NNI) defines nanotechnology as involving research and development at the atomic, molecular, or macromolecular levels in the sub-100-nm range to create structures, devices and systems that have novel functional properties. At this scale, scientists can manipulate atoms to create stronger, lighter and more efficient materials (nanomaterials) with tailored properties [1, 2]. Nanotechnology can also be defined as the outcome of considerable scientific and commercial interest of nanocrystalline semiconductors owing to their tunable optical electronic properties and potential applications in a wide range of electronic devices [1]. A nanometer is a billionth of a meter and in a mental view it can be described that 10000 of these particles can fit well across human hair [3].

1.2 Semiconductor nanoparticle

Semiconductor nanoparticles are materials with diameter in the range of 1-20 nm. These materials most often referred to in literature as nanoparticles, nanocrystals, and quantum dots (QDs), Q-particles, nanoclusters or artificial atoms. They have small dimension with properties different from the corresponding bulk macro crystalline materials. They have unique properties which can be tailored through careful manufacturing processes and their applications are in areas such as electronics and non linear optics [4, 5]. Their unique properties make them one of the

hottest research topics in the past decades. The distinct properties of semiconductor nanoparticles originate from their size which is near the natural length of the exciton. Hence the energy bands of the bulk material are quantized due to the potential well made by the boundaries of the nanoparticles for the carriers. This phenomenon is known as the quantum-confinement effect.

1.3 Particle size effect

This is a phenomenon whereby small particles dissolve easier because of the increased surface area of particles under the same condition [6]. The interaction of small particles with the solvent is faster and hence faster dissolution of the particles. This is as a result of their larger surface area to volum ratio compared to the bulk particles.

1.3.1 Quantum confinement effect

The quantum confinement effect is defined as the increase in band gap of a semiconductor material as the particle size decreases. This occurs when the sizes of nanoparticles is in the order of dimension of Bohr exciton and causes the appearance of unique physical and chemical properties [7]. It is caused by localization of electrons and holes in a confined space resulting in observable quantization of the energy levels of the electrons and holes. For effective confinement, the particle sizes have to be less than 30 nm [8]. There are blue shifting of the spectra peaks as the particle sizes decreases and this has attracted special attention because the existing scope of this effect is fabricating novel electronic devices and solar cell for better efficiency. Quantum confinement describes nanocrytals according to their shapes and it comes in different forms; two dimensional (2-D) confinements are restricted in one dimension and are

extended in two. This can be found in thin film of macroscopic width and length and results in quantum wells or planes. They are the foundation blocks of most lasers. In the case of one dimensional (1-D), which are confined in two dimensions and extended in one which can also be described as nanometer size cylinders and are found in nanowires. 0-D (zero dimensional) is unidirectional nanosized spheres that are confined in all three dimensions and is found only in quantum dots [9].

In nature, 0-D confinement is found in atoms. A quantum dot exhibits 0-D confinement and in this system the exciton is confined in all three dimensions (x, y, z). Thus, a quantum dot can be loosely described as an artificial atom [10, 11] because of the discretization of conduction and valence bands caused by quantum confinement of charge-carriers. This achievement is very important since we cannot readily experiment on regular atoms because they are too small and too difficult to isolate in an experiment. Quantum dots, on the other hand, are big enough to be manipulated by magnetic fields, optically trapped and can even be moved around [12]. Quantum confinement is hugely important because it leads to new electronic properties that are not present in today's semiconductor devices. Density of states is the states in bands and their dependence on energy and plotting its function against energy levels for 3D, 2D, 1D, and 0D revealed a continuous energy for the bulk and discrete or quantized energy level for quantum dots as shown in Figure 1.1.

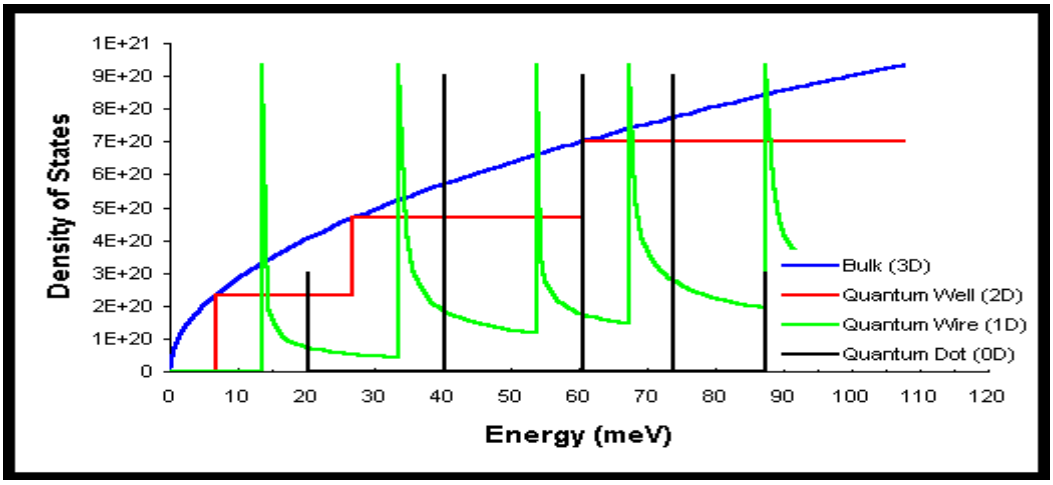

Figure 1.1: Density of states for bulk (3D blue), quantum well (2D red), quantum wire (1D green) and quantum Dot (0D black) [13].

1.3.2 Electronic properties

In a bulk crystal, the properties of the material are independent of the size but only dependent on chemical composition. The valence band is the lowermost band and is almost fully occupied band while the uppermost, almost unoccupied band is called the conduction band. These two bands are separated by an energy gap (Eg), the magnitude of which is a characteristic property of the bulk microcrystalline material (at a specific temperature). The energy gap separating the conduction and the valence band is one of the features of semiconductor and the gap width is a fixed parameter determined by the material's identity. When the size of crystal decreases to the nanometer regime, the properties of the crystals are modified by the sizes of the particle. There occurs a change in the electronic properties of material and as the size gets smaller the band gap increases because of quantum confinement effects. This phenomenon causes the continuous band of the solid to split into discrete, quantized electronic levels instead of the continuous band of the corresponding bulk crystal [14].

1.3.3 Optical band behaviour

Quantum confinement effect which occurs as the size of a semiconductor nanocrystal enters its nanometric domain is manifested as an increase in the band gap energy. The energy which the nanocrystal emits as luminescent photons as the electron fall back to the valence band from the excited conduction band is increased. The energy of the emitted photon thus serves as a direct measure of the band gap energy, Eg. The smaller the effective mass of charge carrier, the larger the quantum.

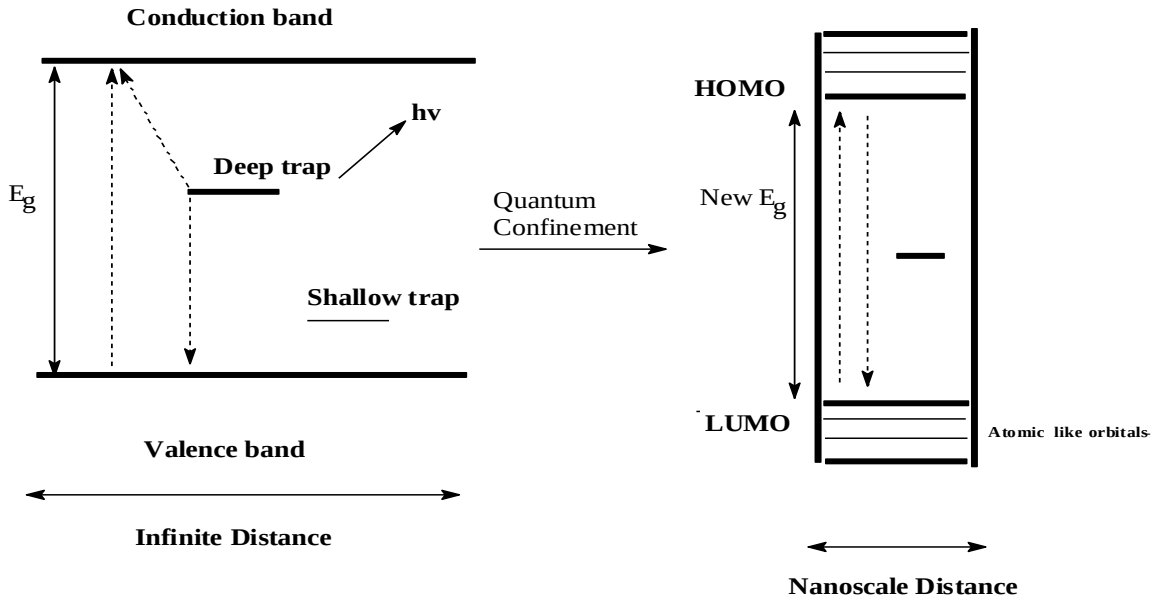

Figure 1.2: Spatial electronic state diagram showing quantum confinement (a) bulk semiconductor (b) nanocrystal [15].

There are two types of charge carriers in semiconductors; one of them carries negative electric charge electrons, the second one carries positive charge equal in magnitude to that of an electron and there are travelling vacancies in the valence electron band called hole. This hole is left in a semiconductor material when ionizing radiation strikes it and electrons are excited. When the

particle size is reduced to the nanosize regime, and the diameter of the particle approaches the exciton Bohr diameter, the charge carriers (electron-hole pair), which are usually delocalized over a length much longer than the lattice constant now, become confined in three dimensions with zero degrees of freedom (a). Because of geometry constraint, the electron feels the particle boundaries and responds to the particle sizes by adjusting its energy (b). Hence, this gives rise to discrete energy levels rather than continuous band observed in corresponding bulk material. Figure 1.2 shows the widening of the band gap energy as a bulk semiconductor reduces to the nanocrystaline size. The combination of the conduction band electrons and valence band holes contribute to electrical conductivity. This process is known as electron–hole pair generation and it can also be generated by thermal energy. Conservation of energy demands in a recombination event, those electrons lose an amount of energy larger than the band gap and such situation is accompanied by the emission of thermal energy or radiation in form of photons. Nanoparticles possess unique optical and electronic properties not observed for corresponding bulk materials. The increase in the band gap is observed by the blue shift in the absorption spectra as seen in many semiconductor nanoparticles.

1.3.4. Surface effects

There are substantial reconstructions in the atomic positions at the surface of pure semiconductor, and it is nearly inevitable that there exist energy levels (surface states) within the energetically forbidden gap of the bulk solid [16, 17] arising from the surface non-stoichiometry, unsaturated bonds. These surface states act as traps for electrons or holes and manifest themselves as a degradation of the electrical and optical properties of the material. In some cases,

the surface states can also be involved in radiactive transition. There is a strong influence of surface states on their optical properties [18] as a result of the relatively large surface to volume ratio in semiconductor particles. The fraction of the surface molecules aggregates also decreases with particle size [19]. This causes an imperfect surface which can act as traps for photo generated charge carriers. Surface atoms tend to find equilibrium positions to balance the forces resulting in surface reconstruction and defects because they have fewer bonds in comparison to the atoms in the bulk. There has been motivation for the experimentation with surface chemical modification in search for new materials with strong optical nonlinear behavior [20]. The band edge is due to the direct recombination of charge carriers from atom-like orbitals. Charge carriers in bulk semiconductor recombine from the deep shallow traps giving the emission at different wavelengths from the band edge [21]. This quantum-size effect causes structural and electronic changes that in turn induce other novel properties that largely dominate the behaviour of these materials and make them different from that of the bulk. The decrease in particle size leads to an extreme high surface area to volume ratio which leads to an increase in surface specific active sites for chemical reaction and photon absorption that enhance the reaction and absorption efficiency.

1.4 General approach to nanoparticles syntheses

1.4.1 Top-down approach

This approach involves division of a massive solid into smaller portions. It may involve milling or chemical methods, and volatilization of a solid followed by condensation of the volatilized

components. This approach uses traditional methods to guide the synthesis of nanoscale materials. The paradigm proper of its definition generally dictates that in the 'top-down' approach it all begins from a bulk piece of material, which is then gradually or step-by-step removed to form objects in the nanometer-size regime. Well known techniques such as photo lithography and electron beam lithography, anodization, ion- and plasma-etching, all belong to this type of approach. This approach for nanofabrication was first suggested by Feynman in his famous American Physical Society lecture in 1959 [22].

1.4.2 Bottom-up approach

Nanoparticles fabricated by this approach involve condensation of atoms or molecular entities in a gas phase or in solution. This approach is far more popular in the synthesis of nanoparticles and it involves the generation of particle from atomic level using a chemical process. In this way, instead of starting with large materials and cutting it off to reveal small bits of it, it all begins from atoms and molecules that get rearranged and assembled to larger nanostructures. It is the new idea for synthesis in the nanotechnology world as the 'bottom-up' approach allows the creation of diverse types of nanomaterials, and it is likely to revolutionize the way we make materials. It requires a deep understanding of the short-range forces of attraction such as *Van der Waals* forces, electrostatic forces, and a variety of interatomic or intermolecular forces. Since it is not possible to have various minute particles come together without some attractive force or active field of force in the region, having the fundamental forces "doing all the work" for you is the key principle underlying this approach This approach is far more popular in the synthesis of nanoparticles.

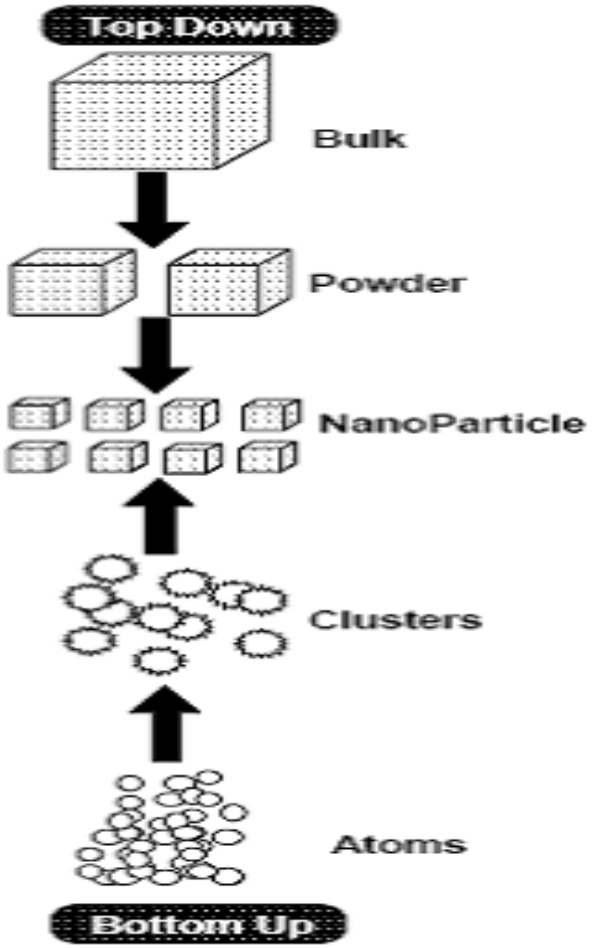

Figure 1.3: Diagramatic representation of a Top-down and Bottom-up approaches of synthesizing nanoparticle [23].

1.5 Nanoparticle classification

Nanoparticles are generally classified based on their dimensionality, morphology, composition, uniformity, and agglomeration.

1.5.1 One-dimensional (1D) nanomaterials

Materials with one dimension in the nanometer scale are typically thin films or surface coatings, and include the circuitry of computer chips and the antireflection and hard coatings on eyeglasses. Thin films have been developed and used for decades in various fields, such as electronics, chemistry, and engineering. Thin films can be deposited by various methods, [24] and can be grown controllably to be only one atom thick, a so-called monolayer.

1.5.2 Two-dimensional (2D) nanomaterials

Two-dimensional nanomaterials have two dimensions in the nanometer scale. These include 2D nanostructure films, with nanostructures firmly attached to a substrate, or nanopore filters used for small particle separation and filtration. Free particles with a large aspect ratio, with dimensions in the nanoscale range, are also considered 2D nanomaterials. Asbestos fibers are an example of 2D nanoparticles.

1.5.3 Three-dimensional (3D) nanomaterials

Materials that are nanoscaled in all three dimensions are considered 3D nanomaterials. These include thin films deposited under conditions that generate atomic-scale porosity, colloids and free nanoparticles with various morphologies.

1.6 Application of nanoparticles

The unique phenomenon of nanoparticles properties (novel electrical, optical, chemical,

mechanical, magnetic properties etc.) can be selectively controlled by engineering the size, morphology and composition of the particles. These new substances will have entirely different properties from their parent material. Hence industries can reengineer many existing products and design novel product or processes to function at unprecedented levels. Below are some of the applications of nanoparticles.

1.6.1 Catalytic Applications

The field of nanocatalysis (in which nanoparticles are used to catalyze reactions) has undergone an exponential growth during the past decade. Two types of studies have been carried out; homogeneous catalysis in solution and heterogeneous catalysis in which the nanoparticles are supported on a substrate [25]. Furthermore, the changes in electronic properties arising due to quantum confinement in small nanocyrstals also bestow unusual catalytic properties on these particles because nanoparticles have a large surface-to-volume ratio compared to bulk materials and they are also used as catalysts [26]. This potential shape dependent catalysis adds to the advantage of using nanoparticles as catalysts. In the course of catalysis, the fact that nanoparticles are small with corners and edges could make their surface atoms unstable during the chemical reaction they catalyze and shape changes could occur. Yates *et al*. [27] showed that there is a decrease in catalytic activity per unit surface area of nickel with the increase in particle size in the hydrogenation reaction of ethene. Modified nanocatalysts have been explored to enhance selectivity and stability and this show that the role of catalysts is more than speeding up reaction rates [28]. Also nanoparticles used as catalysts in combustion engines, have shown properties that render the engine more efficient and therefore more economic.

1.6.2 Biological application

Nanoparticles were studied earlier because of their size-dependent physical and chemical properties but recently they have entered a commercial exploration period [29]. The capability of control of production and preparation of specific sizes and shapes of the nanoparticles has attracted investments from developed countries. Nanotechnology is expected to influence and further revolutionize the practice of medicine and may well have important applications spanning all aspects of diseases, diagnosis, prevention and treatment. Quantum dots probes can be used to track molecules and cells over extended period of time without introducing too much of interference or in a better way they can be used as very small probes that will allow us to spy at cellular machinery [30].

1.6.3 Cancer therapy

The osteoblasts cells responsible for the growth of the bone matrix that are found on the advancing surface of the developing bone are stimulated by creating nano-sized features on the surface of the hip or knee prosthesis because if the surface of artificial bones are left smooth the body will reject it. This layer reduces the bone-implant contact, which may result in the loosening of the implant and further inflammation [31]. Nanoparticles could be engineered and used for anti-reflection product coatings, producing a refractive index for various surfaces, and also providing light based sensors for use in cancer diagnosis.

1.6.4 Energy

Due to their tiny size, nanoparticles are inherently poised to enhance the production of high

performance delicate electronics; they may provide not only materials with a high rate of conductivity, but also sleeker parts for small consumer electronics like cell phones. And when it comes to advertising, nanoparticle electronics can create digital displays that are more electricity-efficient, less expensive to produce, brighter in colour, and also bigger [32].

1.6.5 Thermal application

Specifically engineered particles could improve the transfer of heat from collectors of solar energy to their storage tanks. They could also enhance the coolant system currently used by transformers in these types of processes with a wide range of active self-assembly mechanisms for nanoscale structures that start from a suspension of nanoparticles in fluid. Addition of nanoparticles in a liquid remarkably enhances the energy transport process of the base liquid [33].

1.7 Shape control of nanoparticle

The shapes of nanoparticles have a significant effect on their electronic, magnetic, catalytic and electrical properties. Metal chalcogenides such as CdSe, CdS remain materials of interest in shape control. For a given solution in nanocrystal synthesis, one could obtain a variety of shapes; dot, rod, spindle and tetrarod. As the size of the nanoparticles diminish to the Bohr magneton all the electronic properties become dependent not only on the size but on the shape. Quantum dot are formed in an electron-hole pair exciton with zero degree of freedom. In this system, the exciton is confined in all three dimensions (x, y, and z). For particles elongated along c –axis the exciton formed will be confined in x and y direction (a & b) but can be transported along z axis

and display the rod-like structure. These are referred to as 2D structures for the exciton's motion are confined in one direction and propagated along x and y [34].

1.7.1 Critical parameter for shape control

There are several critical parameters that influence the type of growth regime and they are; monomer concentration, reaction temperature and capping group. A thermodynamics growth regime is governed by sufficient supply of thermal energy (high reaction temperature) and low monomer concentration yielding stable isotropic-shaped nanocrystals (e.g. dots, cubes). On the contrary, nonequilibrium kinetic conditions are enhanced by low reaction temperatures and high monomer concentration yielding selective anisotropic structures (e.g. rods, tetrapods) [35, 36].

1.7.2 Effect of temperature

The growth and size of nanoparticle is greatly influenced by temperature. The shape evolution from sphere to rod is evident with an increase in reaction temperature. It was reported also found in a study using cadmium complexes of thiourea, *N*,*N*'-dioctyl thiourea, *N*,*N*'-dicyclohexyl thiourea, and *N*,*N*'-diisopropyl thiourea for the preparation of tri octyl phosphine oxide (TOPO) capped CdS nanoparticles that at higher temperature there appear to be the formation of more well defined rod-shaped particles than at lower temperature [37].

1.7.3 Effect of capping agent

The capping group or surfactant plays an important role in the nanocrystal growth [38]. The surfactant molecules are dynamically absorbed to the surface of growing crystals, thereby stabilizing the particles in solution and mediating their growth. The hexadexyl ammine (HDA) and other organic capping groups such as tri-n-octylphosphine oxide (TOPO) and 4-ethylpyridine have been used in stabilizing the metal chalcogenide nanoparticles [37, 39]. TOPO has been the original choice as capping group, pioneered by Bawendi *et al*. [40]. It has been discovered that a variation of capping groups causes changes in particle morphology. Nair *et al*. [41] reported the synthesis of spherical TOPO capped CdS nanoparticles using a cadmium ethylxanthate as a precursor. Li *et al*. [42] used the same precursor in HDA to obtain rod shaped particles. The mode of interaction of the capping group is a crucial factor that tends to drive growth of particles along a particular plane making them more orientated towards a particular shape.

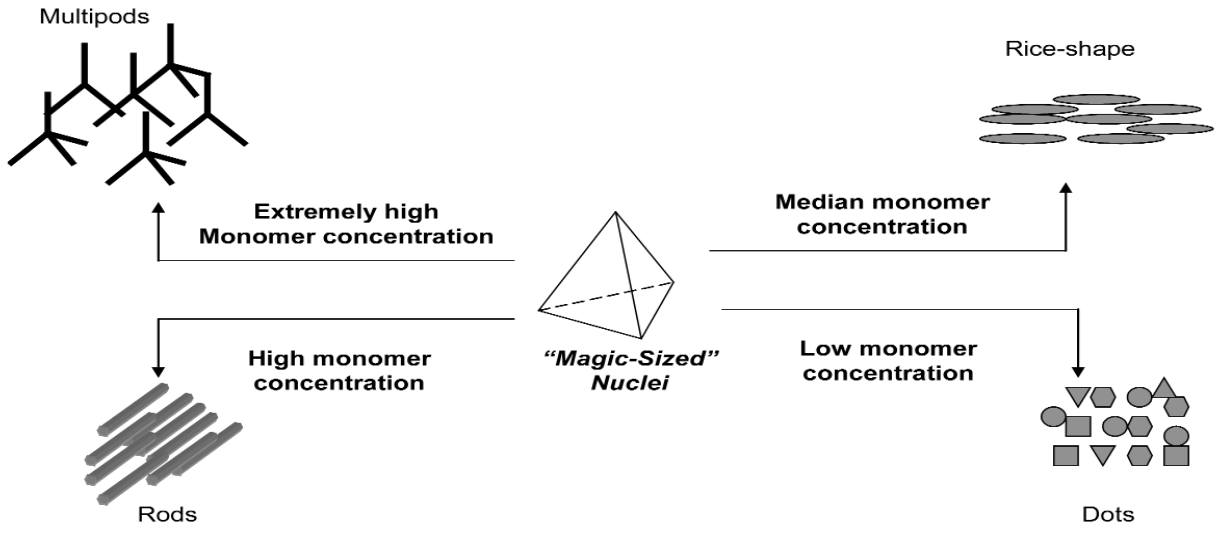

Figure 1.4: Monomer concentration-dependent growth patterns of nanocrystals [44].

It has also been shown by Alivisatos *et al*. [43] that by changing the surface energies through adjustment of the types and ratios of organic surfactants the shape of CdSe nanoparticles could be controlled.

1.7.4 Optoelectronic and light emitting diodes (LEDs).

One of the most important parts of optoelectronic devices are light emitting diodes (LEDs) and several factors are driving their development. The most important of theses are; brightness, efficiency, flexibility, lifetime, rugged construction, low power consumption and suitable driving voltage. These properties are contributing to growth in markets such as traffic lights, automotive brake signal display, decorative signs and the many uses of the new white LED-based products. Conventional LEDs includes GaAsP (yellow to red) and GaP (green to red) device. It has been established that when quantum dots are incorporated into the active region of optoelectronic devices, the device performance is drastically improved. Primarily, this is due to enhanced carrier density of states. A large density of states is highly desirable for optoelectronic devices such as lasers and detectors [45].

1.8 Preparation methods

1.8.1 Colloidal routes

Colloidal access to nanoparticles can be carried out successfully by the precipitation reaction in a homogenous solution in the presence of stabilizers whose role is to prevent agglomeration and enhance growth [46, 47]. Colloidal quantum dots synthesis is based on precursor organic surfactants and solvents. When heating a reaction medium to a sufficiently high temperature, the

precursors are chemically transferred to a monomer. Nanocrystal growth starts with a nucleation process once the monomers reach a high enough supersaturated level. One of the critical factors determining optimal condition for nanocrystal growth is the temperature during the growth process. It must be high enough to allow for rearrangement and the annealing of atoms during the synthesis' process while being low enough to promote crystal growth. The colloidal stability of the crystal can be improved using solvents with low dielectric constant stabilizers such as styrene/maleic acid as copolymer. The reaction between an aqueous solution of $CdSO_4$ and $(NH_4)_2S$ is a typical example for the precipitation synthesis of CdS nanoparticle [48]. The colloidal route is an efficient one for the preparation of nanosized semiconductor particles. However, certain types of semiconductors such as CdSe, GaAs, InP and lnAs, cannot be synthesized easily using this route. Annealing of the colloidal particle is also a problem as these tend to be a low temperature process. Such aqueous prepared nanoparticles are not sufficiently stable at higher temperature and thus makes annealing of the particle difficult, thereby making the material poorly crystalline.

1.8.2 Precursor routes

This route was pioneered by Bawendi *et al*. [40, 49] and it employs an organometallic or metal organic compound under anaerobic conditions. It overcomes the problem of low temperature that is encountered in colloidal routes and it uses a volatile metal alkyl (dimethylcadmium) and a chalcogen source, tri-n-octylphosphine selenide (TOPSe) for sulfur-containing particles which are dispersed in tri-n-octylphosphine (TOP) and is then injected into hot tri-n-octylphosphine oxide (TOPO). The sudden injection of TOPSe leads to super saturation and the formation of

nuclei. This is followed by slower particle growth, with the resulting particles being passivated by TOP and TOPSe coordinating to the surface metal atoms on the particle. This is consistent with Oswald ripening [50]. Particles produced by this route were monodispersed and crystalline. The nanoparticles were passivated by a monolayer of the solvent ligand and hence could be isolated or purified by solvent or non-solvent interactions. Purified nanocrystals undergo size selective precipitation to provide powders of nearly monodispersed nanocrystals which can be dispersed in a variety of solvents. The particle size can be controlled by varying the temperature and the time of the reaction. At higher temperature the surfactant molecules are forcefully adsorbed on the surface of the growing crystal, thereby stabilizing the particles in solution and mediating their growth [51]. Other organic molecules with different functional groups and polarity can be exchanged with the surfactant. Examples of high boiling point coordinating solvents used include alkyl phosphates, pyridines, long-chain alkyl amines and furan [52].

1.8.3 Single molecule precursor

The use of a single-source molecular precursor containing both metal and the chalcogen source has been studied as an effective route to semiconductor nanoparticle production. Brenman *et al*. [53] introduced the single source precursor (SSP) approach as an alternative synthetic route for metal chalcogenide semiconductor nanocrystals at the end of the 1980s, performing the pyrolysis of $Cd[Se(C_6H_5)]_2$ in a high boiling point solvent (4-ethylpyridine). Since then, the compounds Hthat have found greatest dissemination as single-source precursors for II-VI and IV-VI semiconductors are the dialkyl–dithiocarbamate complexes. Trindade and O'Brien [54, 55] investigated cadmium dithio- and diselenocarbamate complexes as precursors for the preparation

of TOPO-capped II/VI semiconductor nanoparticles. This method of preparation involves the dispersion of the precursor in TOP followed by injection into hot TOPO. The formation of the nanoparticles is consistent with the La Mer mechanism for colloids [56]. The decomposition of the precursor drives the formation of the nanoparticles with termination of growth occurring when the precursor supply is depleted. After the initial injection there is rapid nucleation, followed by controlled growth of the nuclei. When the nanoparticles reach a desired size, further growth is arrested by quickly cooling the solution. The nanocrystals are isolated from the growth solution by adding another solvent that is miscible with the initial solvent, but has an unfavourable interaction with the capping groups, thereby reducing the barriers to aggregation resulting in flocculation. The resultant turbid solution is centrifuged, and the nanoparticles are isolated in the form of a powder. The capped nanoparticles can be dispersed in a variety of solvents for optical or physical measurements.

1.9 Review of relevant literature

The advancement of technologies to the nano-level and development of real nanotechnologies require efficient simple and environmental friendly approaches. Single-source precursors for thin films and nanocrystals have several key advantages over other routes. For example, the existence of preformed bonds can lead to a material with fewer defects and better stoichiometry [57]. Substituted thioureas are important precursors for the preparation of metal sulfide nanoparticles. Besides focusing on the applications of these ligands, special attention has been placed on their coordination chemistry to different metal atoms because of the various potential donor sites that these ligands possess and their high selectivity for the separation of metal ion [58, 59].

Rosenheim and Meyer [60] reported the complexation of Fe(II) with thiourea and concluded that the coordination was through the sulfur atom, using infrared spectroscopy and X-ray diffractions to determine the coordination. In addition, complexes prepared using the alkyl thiourea, such as methylthiourea, were confirmed through infrared spectroscopy, that the coordination to the metal ions was through the sulfur atoms [61]. Thiourea and its derivatives were used as sulfur sources due to their stability for a long time, ease of synthesis, inexpensive and yield good quality crystalline semiconductor particles.

Tetramethyl thiuram disulfide is also used as a ligand to form coordination complexes with some metal ions for the preparation of II-IV semiconductor nanoparticles. The thiuram disulphide unit consists of four sulfides groups and hence the binding to the metal centre upon formation of complexes would most likely be through the sulfides. The stability of the complexes is enhanced by the chelating ability of the ligand to the metal ions. This resulted in an interest in tetramethylthiuram disulfide complexes of cadmium as potential single source precursors for the synthesis of CdS nanoparticles [62]. There have been many studies on substituted thioureas which are coordinated to metal ions through the sulfur atom. For example, Shumbula *et al*. [59] reported the reaction between a number of N-alkyl substituted thioureas with lead, copper and cadmium. Thiourea complexes have been used as starting materials in chemical spray pyrolysis (CSP) processes which are used to produce thin films of binary and tertiary sulfides [39, 63]. The use of thiourea and their substituted constituents for the preparation of metal sulfide nanoparticles have also been reported by Moloto *et al*. [64].

A series of metal(II) di- and tri-alkylthiourea complexes have been synthesized and characterized. Their bondings through sulfur atoms make these complexes useful as single molecule precursor for the preparation of metal sulfide nanoparticles. Most of the studies on thiourea metal complexes have been on the trace analysis of platinum metal in complex matrices and the biological activities of the metal complexes [65-68]. Tetramethyl thiuram disulfides containing compounds are used mainly in vulcanization of rubber or as fungicides [69]. The single X-ray structures of the thiosemicarbazide complexes, $[Cd(NH_2CSNHNH_2)Cl_2]n{\cdot}H_2O$ and $[Cd(NH_2CSNHNH_2)_2Cl_2]n$ was reported by Mlondo *et al*. [70]. Both compounds were found to be effective as single source precursors for the preparation of CdS nanomaterials. The thermolysis of the precursors in hexadecylamine (HDA) resulted in the formation of nanorods with different dimensions.

Bruce *et al*. [71] reported the synthesis of cadmium complexes of *N*, *N*-diethyl-*N*'-benzoylthiourea and *N*, *N*-diethyl-*N*'-benzoylselenourea as single source precursors for HDA capped CdS and CdSe nanoparticles that occurred in a predominantly cubic phase respectively. Both types of particles show quantum confinement effects which is very close to band edge luminescence. Spherical CdS nanoparticles of 3.9-4.2 nm in diameter were obtained, from cadmium ethylxanthate through a single source precursor route [72]. This same precursor was extensively studied by Li *et al*. [73] and hexagonal phase rods, bipodal and tripodal structured CdS naoparticles were prepared. It was discovered that balancing the thermodynamic and kinetic control of conditions like temperature, concentrations and time determines the morphology of the resultant nanoparticles. For example, thiourea have been used as sulfur

sources in the synthesis of the cadmium complexes, [$Cd(NH_2CSNHNHCSNH_2)Cl_2$], as a precursor for CdS nanoparticles [61]. The precursor was thermoysed in tri-n-octylphosphine oxide (TOPO) to obtain CdS nanoparticles which showed good quantum confinement effects and characteristic close to band edge luminescence.

The morphology of CdS nanoparticles was found to be influenced by the alkyl chain length of the precursors. This was investigated in Cd(II) complexes *N*,*N*–dialkyl thiourea of *N*,*N*–dioctyl, N,N–dicylo hexane and *N*,*N*- diisopropylthiourea complexes [74]. An air stable precursor, [(2,2-bpy)$Cd(SC\{O\}Ph)_2$] whose molecular structure has been determined by X-ray crystallography have also been used to prepare a CdS water soluble quantum dots via a refluxing single precursor [75]. The prepared nanocrystals have fairly uniform sizes and exhibit a quantum size effect. The synthesis of ZnS nanoparticles from low cost single source precursor in a continuous spray pyrolysis reactor was reported by Liu *et al*. [76] giving particles with diameter ranging from 2 - 7 nm were produced. Tiwari *et al*. reported the synthesis of polyphosphate capped ZnS nanoparticles by a simple aqueous method using thiourea as sulfur source. X-ray diffraction (XRD) indicated that the ZnS nanoparticles were 1.38 nm in size with a zinc blende structure [77]. ZnS nanoparticles have also been prepared from zinc nitrate and thiourea in an ethyl alcohol solution using electrostatic assisted aerosol jet decomposition techniques, but a mixture of cubic sphalerite and hexagonal wurtzite structures were obtain depending on the Zn/S ratio [78].

1.8.1 Aims and objective of this dissertation

1. To synthesize and characterize Zn(II), Cd(II), and Hg(II) complexes of substituted thiourea, 1-ethoxylcarbonyl-1-cyanoetheylene-2,2-dithiolate and tetremethylthiuram disulfide.

2. To use the metal complexes prepared as single source precursors for the preparation of metal sulfide semiconductor nanoparticles.

3. To characterize the metal sulfide nanoparticles with UV-Vis, PL, XRD, TEM and SEM.

References

1. Baker, S.; Aston, A.; Buss: The business of Nano technology, Business *Week* **2005**, Feb 14, 64-67.

2. Bawa, R.M.S.; Bawa, S.R; Stephen, B.; Maebius, J.D.; Flynn, T.; Wei, C. Protecting new ideas and inventions in nanomedicine with patents Nanomedicine. *Nanotechnology, Biology and medicine* **2005**, 1, 150-158.

3. Australian Government department of health and ageing; *NICNAS information sheet, Nanomaterials,* September **2006**, 1-8.

4. Kamat, P.V.; Meisel, D. Semiconductor nanoclusters studies in surface science and catalysis. *Elsevier Amsterdam* **1997**, 103-105.

5. Huynh, W.U.; Dittmer J.J.; Alivasatos A.P. Nanocrystal solar cells. *Sci*. **2002**, 295, 2425-2427.

6. Kaptay, G. On the size and shape dependence of the solubility of nano-particles in solutions. *Int. J. Pharm*. **2012**, 430, 253-257.

7. Nanda, K.K.; Kruis, F.E.; Fissan, H.; Acet, M. Band-gap tuning of PbS nanoparticles by in-flight sintering of size classified aerosols. *J. Appl. Phys*. **2002**, 91, 2315-2315.

8. Ring Surf: Nanotechnology structures-quantum confinement, 2003-2007 http://www.ringsurf.com**.**/online/2003.structures.html.

9. Murphy, C.J. Protein-sized quantum dot luminescences can distinquish quantum dots. *Anal. Chem*. **2002**, 74, 520A-526A.

10. Jinesh, K.B.; Kartha, C.S.; Vijayakumar, K.P. Effects of size quantization in the I-V Characteristics of CdS bulk-nano junctions. *Appl*. *Surf*. *Sci*. **2002**, 195, 263-269.

11. Bratschitsch, R.; Leitenstofer, A. Quantum dots: Artificial atoms for optics. *Nat*. *Mat*. **2006**, 5, 855-856.

12. Goryca, M.; Kazimierczuk, T.; Nawrocki, M.; Golnik, A.; Gaj, J.A.; Kossacki, P.; Wojanr, P.G.; Karczewski, G. Optical manipulation of a single Mn spin in a CdTe-based quantum dot. *Phys*. *Rev*. *Lett*. **2009**, 103(8), 08740-087404.

13. Semiconductor Physics: Density of States, http://britneyspears.ac/physics/dos/dos.html**.**

14. Haug, H.; Koch, S.W. Quantum theory of the optical and electronic properties of Semiconductors. Second edition. **2004**, 56-61.

15. Revaprasadu, N.; Mlondo, S.N. Use of metal complexes to synthesize nanoparticles. *Pure Appl*. *Chem*. **2006**, 78, 1691-1702.

16. Guo, L.; Wu, Z.; Ai, X.; Li, Q.; Zhu, H.S.; Yang, S. The influence of surface modification on the femtosecond optical Kerr effect of PbS nanoparticles. *Opt*. *Mat*. **2000**, 3, 247-250.

17. Rama, J.; Pino, I.R. Physical chemistry: energy meliorum technologies Inc., Band theory and quantum confinement. N. Y, USA 14607. *http://www.meliorum.com/Meliorum***.**

18. Tang, H.; Xu, G.; Weng, L.; Pan, L.; Wang, L. Luminescence and photophysical properties of colloidal ZnS nanoparticles. *Acta Mater*. **2004**, 52, 1489-1494.

19. Chakraborty, I.; Moulik, S.P. Preparation and characterization of PbS nanoparticles in AOT

micellar medium. *J*. *Nano*. *Res*. **2004**, 6(2), 233-240.

20. Wang, Z.L. Transmission electron microscopy of shape controlled nanocrystals and their assembly. *J*. *Phys*. *Chem*. *B*, **2000**, 104, 1160-1175.

21. Wang, Y.; Liu, H.; Toshima, H. Nanoscopic naked Cu/Pd Powder as air-resistant active catalyst for selective hydration of acrylonitrile to acrylamide. *J*. *Phys*. **1996**, 100, 15533-15537.

22. Feynman, R.P.; Leighton R.B.; Sands M. The Feynman lectures on physics, Reading MA: Addison Wesley Publishers; **1961**, (1).

23.http://www.gitam.edu/eresource/nano/nanotechnology/role_of_bottomup_and_topdown_a_files/image002.gif

24. Handbook of thin-film deposition processes and techniques equipment and applications, edited by Seshan K. William Andrew Publishing /Noyes. **2002**, 1-657.

25. Burda, C.; Chem X.; Narayanan, R.A.; Mostafa, E.L., Chemistry and properties of nanocrystals of different shapes. *Chem*. *Rev*. **2005**, 105, 1025-1102.

26. Narayanan, R.; El-Sayed, M.A. Effect of nanocatalysis in colloidal solution on the tetrahedral and cubic nanoparticle shape: Electron-transfer reaction catalyzed by platinum nanoparticles. *J*. *Phys*. *Chem*. *B*, **2004**, 108(18), 5726-5733.

27. Yates, D.J.C.; Sinfelt, J.H. The catalytic activity of rhodium in relation to state of dispersion. *J*. *Catal*. **1967**, 8, 348-358.

28. Gellman, J.A.; Shukla N. Nanocatalysis; More than speed. *Nat*. *Mater*. **2009**, 8, 87-88.

29. Mazzola, L. Commercializing nanotechnology. *Nat. Biotechnol.* **2003**, 21, 1137-1143.

30. Taton, T.A. Nanostructures as tailored biological probes. *Trends Biotechnol*. **2002**, 20, 277-279.

31. Puckett, S.; Pareta, R.; Webster, T.J. Nano rough micron patterned Titanium for directing osteoblast morphology and adhesion. *Int. J. Nanomed*. **2008**, 3(2), 229-241.

32. Hu, J.; Li, L.S.; Wang, L.W.; Manna, L.; Alivisatos A.P. Linearly polarized emission from colloidal semiconductor quantum rods. *Sci*. **2001**, 292(5524), 2060-2063.

33. Singh, A.K. Thermal Conductivity of Nanofluids. *Defence Sci. J*., **2008**, 58(5), 600-607.

34. Harris, P.J.F. Carbon nanotubes and other graphitic structures as contaminants on evaporated films. *J. Microscopy*, **1997**, 186, 88-90.

35. Peng, Z.A.; Peng, X.G. Nearly monodisperse and shape-controlled CdSe nanocrystals via alternative routes: Nucleation and growth. *J. Am. Chem. Soc*. **2002**, 124, 3343-3353.

36. Dan, L.; Kaner, R.B. Shape and aggregation control of nanoparticles: Not Shaken, Not Stirred J. Am. Chem. Soc. **2006**, 128, 968-975.

37. Scher, E.; Manna L.; Alivisatos A.P. Shape control and applications of nanocrystals. *Philos. Trans. R. Soc. London, Ser. B*, **2003**, 361, 241-255.

38. Moloto, M.J.; Revaprasadu, N.; O'Brien, P.; Malik, M.A. N-alkylthioureacadmium(II) complexes as novel precursors for the synthesis of CdS nanoparticles. *J. Mater. Sci. Mat. Electr*. **2004**, 15, 313-316.

39. Moloto, M.J.; Revaprasadu, N.; Kolawole, G.A.; O'Brien P.; Malik, M.A. The synthesis and characterization of CuS and PbS from alkyl thiourea and lead and copper complexes. *S. Afr. J. Sci*. **2005**, 101, 463-465.

40. Murray, C.B.; Norris, D.J.; Bawendi, M.G. Synthesis and characterization of nearly monodispersed CdE (E = sulphur, selenium, tellutium nanocrystsalite crystals). *J. Am.Chem. Soc*.**1993**, 155, 8706-8715.

41. Nair, P.S.; Radhakrishnan, T.; Revaprasadu, N.; Kolawole, G.A. Cadmium ethylxanthate .A novel single-source precursor for the preparation of CdS nanoparticles. *J. Mater. Chem*. **2002**, 12, 2722-2725.

42. Li, Y.; Li, X.; Yang, C., Li, Y. Some affects of single molecule precursors on the synthesis of CdS nanoparticles. *Chem. Mater*. **2003**, 13, 2461-2648.

43. Peng, X.G.; Manna, L.; Yang, W.D.; Wickham, J.; Scher E., Kandavich E.A.; Alivisatos A.P. Shape control of CdSe. *Nature*, **2000**, 404(6773), 59-61.

44. Peng, X.G. Mechanism of shape control and shape evolution of nanocrystals of colloidal *Adv. Mater*. **2003**, 15, 459-463.

45. Grice, A.W.; Bradley, D.D.C.; Bernius, M.T.; Inbasekaran, M.; Wu, W.W.; Woo, E.P. High brightness and efficiency blue light-emitting polymer diodes. *Appl. Phys. Lett*. **1998**, 73, 629-631.

46. Peng, X.G. Mechanism of shape control and shape evolution semiconductor nanocrystal colloidal. *Adv. Mater*. **2003**, 15, 459-463.

47. Tao, A.R.; Habas, S.; Yang, P. Shape control of colloidal metal nanocrystals. *Small*, **2008**, 4, 310-325.

48. El-sayedm, M.A. Small is different: Shape-size and composition-dependent properties of some colloidal semiconductor nanocrystals. *Acc. Chem. Res*. **2004**, 37, 326-333.

49. Murray, C.B.; Kagan, K.R.; Bawendi, M.G. Synthesis and characterization of monodisperse nanocrystals and close-packed nanocrystal assemblies. *Ann. Rev. Mater. Sci.* **2000**, 30, 545-610.

50. Pickett, N. L.; O' Brien, P. Synthesis of semiconductor nanoparticle using single molecular precursor. *The Chem. Rec*. **2001**, 470, 467-479.

51. Nath, S.; Jana, S., Pradhan, M.; Tarasankar, P**.** Ligand-stabilized metal nanoparticles in organic solvent. *J.colloid. Interface Sci.* **2010**, 341, 333-352.

52. Scher, E.C.; Manna, L.; Alivisatos, A.P. Shape control and application of nanocrystals. *Philos. Trans. R. Soc. Lond. Ser. A*, **2003**, 361, 241-251.

53. Brenmam, J.G.; Siegrist, T.; Carrol, P.J.; Stuczinsky, M.; Brus, L.E.; Steigerwald, M.L. The preparation of large semiconductor clusters via the pyrolysis of molecular precursor. *J. Am. Chem. Soc*. **1989**, 111, 4141-4143.

54. Trindade, T.; O'Brien, P. Novel single molecule precursor routes for direct synthesis of CdSe nanocrstallite. *Adv. Mater*. **1996**, 8, 161-163.

55. Trindade, T.; O'Brien, P. Synthesis of CdS and CdSe nanocrystallite using a novel single source molecule precursor approach. *Chem. Mater*. **1997**, 9, 523-530.

56. Jonson, T.; La Mer, V.K. Theory production and mechanism of formation of monodispersed hydrosols. *J. Am. Chem. Soc.* **1947**, 69, 1184-1192.

57. Maji, S.K.; Mukerjee, N.; Mondal, A.; Adhikary B.; Karmakar, B.; Dutta S. Synthesis and characterization of nanocrystalisation of zinc sulfide via zinc thiobenzoate-lutidine single source precursor. *Inorg. Chim. Acta*, **2011**, 371, 20-26.

58. Moloto, M.J.; Revaprasadu, N.; O'Brien P.; and Malik, M.A. N-alkylthioureacadmium(II) complexes as novel precursors for the synthesis of CdS nanoparticles. *J. Mater. Sci.-Mater. Electron*, **2004**, 15, 313-316.

59. Shumbula, M.P.; Moloto, M.J.; Tshikhudo, T.R.; Fernades, T.M. Dichloro-(bis[diphenylthiourea] cadmium complex as a precursor for HDA-capped Cd nanoparticles and their solubility in water. *S. Afr. J. Sci*. **2010**, 106, 1-7

60. Rosenheim A., Meyer, VJZ. Bonding of thiocarbamates to divalent metal salt. *Anorg Chem. German*, **1906**, 49, 13-27.

61. Nair, P.S.; Radhakrishnan, T.; Revaprasadu, N.; Kolawole, G.A.; O'Brien, P. $Cd(NH_2CSNHNHCSNH_2)Cl_2$: A new single source precursor for the preparation of CdS nanoparticle *Polyhedron*, **2003**, 22, 3129-3135.

62. Bailey, R.A.; Peterson, T.R. Some complexes of Fe(I1) with thiourea ligands. *Can. J. Chem.* **1967**, 45, 1135-1142.

63. Moloto, N.; Revaprasadu, N.; Moloto, M.J.; O'Brien, P.; Heiwell, M. *N,N′*-Diisopropyl and N,N′-dicyclohexylthiourea cadmium(II) complexes as precursors for the synthesis of CdS

nanoparticles. *Polyhedron*, **2007**, 26, 3947-3955.

64. Phuong, T.; Khac-Minh, T.; Van Hal, N.T.; Phuong, H.T. Synthesis and antifungal activities of phenylenedithioureas. *Bioorg. Med. Chem. Lett.* **2004**, 14, 653-656.

65. Moloto N.; Revaprasadu N.; Moloto M.J.; O' Brien, P.; Raffery, J.N. N'-diisopropylthiourea and N,N'-dicyclohexylthiourea Zinc(II) complexes as precursors for the synthesis of ZnS nanoparticles, *S. Afri. J. Sci.* **2009**, 105, 258-263

66. Huebhr, O.F.; Marsh J.L.; Mizzoni, R.H.; Mull, R.P.; Schroeder, D.C.; Troxell, H.A.; Scholz, C.R. *J. Am. Chem. Soc.* **1953**, 75, 2274-2275.

67. Arslan, H.; Ulrich, Florke U.; Kulcu, N. The Crystal and Molecular structure of 1-(2-chloro-benzoyl)-3-*p*-tolyl-thiourea. *Turk. J. Chem.* **2004**, 28, 673-678.

68. Sarkis, G.Y.; Faisal, E.D. Synthesis and spectroscopic properties of some new *N, N'*-disubstituted thiorueas of potential biological interest. *J. Hetercycl. Chem.* **1985**, 22, 137-140.

69. Adamczyk, D. The effect of thiuram on the uptake of lead and copper by Melissa Officinalis. *Environ. Eng. Sci.* **2006**, 23, 610-614.

70. Mlondo, S.N.; Revaprasadu, N.; Christian, P.; Helliwell, M.; O'Brien, P.; Cadmium thiosemicarbazide complexes as precurors for the synthesis of nanodimensional crystal of CdS. *Polyhedron*, **2009**, 28, 2097-2102.

71. Jocelyn C.B.; Revaprasadu N.; Koch, K.R. Cadmium(II) complexes of *N,N*- diethyl-*N'*-benzoylthio(seleno)urea as single-source precursors for the preparation of CdS and CdSe

nanoparticles. *New J. Chem*. **2007**, 31, 1647-1653.

72. Nair, P.S.; Radhakrishnan, T.; Revaprasadu, N.; Kolawole, G.A. Cadmium ethylxanthate: A novel single source precursor for the preparation of CdS nanoparticles. *J. Mater. Chem*. **2002**, 12, 2722-2725.

73. Li, Y.; Li, X.; Yang, C.; Li, Y. Some effect of single molecule precursors on the synthesis of CdS nanoparticles. *Chem. Mater*. **2003**, 13, 2461-2648.

74. Nair, P.S.; Chilli, M.M.; Radhakrishnan, T.; Revaprasadu, N.; Christian, P.; O'Brien, P. Some effect of the nature of the ligand and temperature of the decomposition on the formation of the CdS nanoparticles from Cadmium complexes of alkyl substituted thioureas. *S. Afr. J. Sci*. **2005**, 101, 466-470.

75. Zhang, Z.H.; Chin, W.S.; Vittal, J.J. Water-soluble CdS quantum dots prepared from a refluxing single precursor in aqueous solution. *J. Phys. Chem. B*, **2004**, 108, 18569-18574.

76. Liu, S.H.; Zhang, H.; Swihart, M.T. Spray pyrolysis synthesis of Zn nanoparticles from a single-source precursor. *Nanotechnology*, **2009**, 20, 1-9.

77. Tiwaria, A.; Khanb, S.A.; Kherc, R. Surface characterization and optical properties of polyphosphate capped ZnS nanoparticles. *Adv. Appl. Sci. Res*. **2011**, 2, 105-110.

78. Jayalakshimi, M.; Rao, M.M. Synthesis of zinc sulphide nanoparticles by thiourea and their characterization for electronchemical capacitor application. *J. Power Sources*, **2006**, 157, 624-629.

CHAPTER TWO

2. CHARACTERIZATION OF SEMICONDUCTOR NANOCRYSTALS

2.1 Size, composition, optical and electronic properties

The synthesis of size-confined systems must include the characterization as well. This is necessary to understand the fundamental properties of the materials at this nanometer or atomic level. Integrating the nanoscale components would provide the macroscale functions or properties since many phenomena observed in bulk inorganic materials ultimately derive from structures or processes that emerge on length scales spanning several atoms to hundreds of atoms. The characterization/studies of the different properties of semiconductor nanocrystals can be broadly divided into two: theoretical and experimental method of study. However, since this work is based on empirical data, brief description of the different experimental techniques that were employed in the study and characterization of the different nanocrystal systems reported in this thesis will be made; while highlighting a few methods which are based on theoretical perspective. Theoretical methods: Involves the calculational techniques employed for determining the electronic structure of bulk solids and nanocrystals.

The methods used for the determination of the electronic structure for nanocrystals are [1]:

- The Lanczos method
- The method of least-square-error fitting while the electronic structure of the bulk solids is determined using [2-4]:
- Linearized augmented plane wave (LAPW) method

- New generation muffin-tin orbital (NMTO) method
- Crystal orbital Hamiltonian population (COHP) computation
- Tight-Binding (TB) method

The experimental methods are divided into chemical and structural characterization.

2.2 Chemical characterization

Chemical characterization techniques determine both the surface and interior atoms of compounds and give relevant information on the spatial distributions. The techniques can be generally grouped into various optical, electron spectroscopy and ion spectrometry [5]. Optical spectroscopy of nanocrystals probes how both conduction and valence band change in quantum confinement, how the conduction band and the valence band change separately must be measured by electronic spectroscopy.

2.2.1 Optical spectroscopy

2.2.2 UV-Visible absorption spectroscopy

One of the most extensively studied properties of a semiconductor particle within the nanometer regime is the systematic changes in its electronic structure as a function of its size. UV-Visible spectroscopy is used to probe the quantum confinement effect and also for calculating the optical band gap of semiconductor nanostuctured materials.

The reduction in particle size of a semiconductor material to the nanometric regime confines the wavefunction of electrons and holes to nanometric dimension and modifies the structure of the electronic levels. This gives unique optical and electrical properties to the material. The UV absorption spectra of semiconductor nanocrystal show a characteristic blue shift as a result of the widening of the band gap E_g between the highest occupied electronic states and the lowest unoccupied states [6]. The absorption is dominated by the features corresponding to the transition across the band gap and the exciton formation. The possible transitions of electrons in a crystal across the band gap are band to band and between sub bands between impurities and band. Fundamental absorption in this study refers to the transition of electrons between band to band and excitonic transitions.

According to Beer-Lambert [7], in the absorption process, a photon of energy excites an electron from a lower to a higher energy. The intensity I_o of the photon of energy $h\nu$ is absorbed by the material according to the equation.

$$I = I_o \, exp\,(\alpha CL) \quad \ldots\ldots\ldots\ldots\ldots\ldots\ldots\ldots\ldots\ldots\ldots\ldots\ldots\ldots\ldots\ldots \quad (2.1)$$

Where, α is the absorption coefficient, C is the concentration of the absorbing material in moles per liter and L is the thickness of the cuvette traversed by the light, in centimeters. The fundamental absorption manifest itself by a rapid rise in the absorption spectra and this can be used to determine the energy gap of the semiconductors [8]. The energy band gap of the nanoparticles can be calculated by using the relationship between absorption coefficient and incident energy ($h\nu$) known as Tauc relation, equation 2.1, [9]. This is obtained with the help of reflection spectra.

$$\alpha h\nu = A\left(h\nu - E_g\right)n \qquad \text{……………………………………………….. (2.2)}$$

Where A = Constant

E_g = the band gap of the material

n depends on the type of transition. If the transition is allowed direct, n = ½; for allowed indirect, $n = 2$; for forbidden direct $n = 3/2$; and for forbidden indirect $n = 3$. The absorption coefficient α is proportional to $Ln\ [(R_{max} - R_{min})/(R - R_{min})]$, where the reaction falls from R_{max} to R_{min} due to the absorption by the material and R is the reflectance for any intermediate energy photons. So α is used in terms of reflectance as $[(R_{max} - R_{min})/(R - R_{min})]$. After calculating the absorption coefficient α, the nature of the transition can be determined by plotting $d\{ln(\alpha h\nu)\}/\ dh\nu$ versus $h\nu$ [10]. The graph will give a divergence at an energy value equal to $E1$ where the transition takes place. The slope of the plot $ln(\alpha h\nu)$ versus $(h\nu - E_g)$ will give the value of $n1$. The exact value of the band gap can be determined by plotting $(\alpha h\nu)^{1/2}$ versus $h\nu$ graph and extrapolating the straight line portion of the graph to $h\nu$ axis (or $(\alpha h\nu)^2 = 0$) [11].

2.2.3 Photoluminescence spectroscopy

Photoluminescence spectroscopy is a simple, contactless, nondestructive method of probing the electronic structure of materials [12]. It involves a process of photon excitation followed by photon emission. The crystal to be characterized when irradiated with photons of energy greater than the band-gap energy of that material causes the electrons within the material to move into

permissible excited state. When these electrons and holes recombine, the excess energy is released and may include the emission of light (a radiative process) or may not (a nonradiative process). Figure 2.1 is a schematic representation of this mechanism. The information obtainable from the analysis of the released energy makes photoluminescence (PL) a vital instrument in the characterization of nanoparticles.

Photoluminescence can be said to involve three main phases [13]:

- Excitation: Energizing the electrons by some external means. The electrons can absorb energy from external sources, such as lasers, arc discharge lamps, and tungsten-halogen bulbs, and be promoted to higher energy levels. In this process electron-hole pairs are created.
- Thermalisation: Excited pairs relax towards quasi-thermal equilibrium distributions.
- Recombination: The energy can subsequently be released in the form of a lower energy photon, when the electron falls back to the original ground state. This process can occur radiatively or non-radiatively.

The intensity and spectral content of photoluminescence is a direct measure of various important material properties. Hence, photoluminescence can be used to probe the properties of semiconductor nanocrystals [14].

2.2.4 Optical band gap behaviour

Quantum confinement effect which occurs as the size of a semiconductor nanocrystal enters its nanometric domain is manifested as an increase in the band gap energy. Thus the energy which the nanocrystal emits as a luminescent photon as the electrons fall back from the bottom of the

excited state conduction band to the top of the valence band is increased. The energy of the emitted photon thus serves as a direct measure of the band gap energy, E_g. The increase in the band gap energy results in an increase in the photoluminescence peak energy. The smaller the effective mass of charge carriers, the larger the quantum confinement effects and the more the shift in the photoluminescence peak energy. Hence, when the size of nanocrystals is reduced the effective band gap increases and therefore the photoluminescence peak shifts to the blue side. From the shifting in the photoluminescence peak, the increase in effective band gap can be estimated, which is then drelated to the size of the particles [15].

2.2.5 Quantum confinement effects studies

Photoluminescence is directly related to the electronic structure and transition of charge carriers. Because of this direct relationship, it is a good technique for studying the dynamic processes occurring in semiconductor nanocrystals and the quantum confinement effects. The difference in behavior between bulk and low dimensional semiconductors can be related to the difference in their electron density of states, g (E) [16]. As shown earlier, the g(E) of bulk semiconductor has continuous dependence of energy E as $g(E) \approx E^{1/2}$; in two dimensional semiconductors it has a step like dependence on energy. In 1D semiconductor structures it diverges as $E^{1/2}$ and for zero dimensional semiconductors it is a delta function of energy. In a bulk semiconductor, where there is no quantum confinement, the frequency of photoluminescence peak (ω_o) corresponds to its band gap. But, in low dimensional systems in which the energy levels in the conduction band and valence band are quantized, the frequency of photoluminescence emission, ω_{PL} corresponds to the transition of excited electrons from the lowest state in the conduction band to the lowest

state in the valence band. Because $\omega_{PL} < \omega_o$, the photoluminescence peak in low dimensional system shifts towards blue compared to that in the corresponding bulk material [17]. The change in band gap as a result of quantum confinement effect can be studied from the blue shift in the photoluminescence peak position.

2.2.6 Recombination mechanisms

The underlying dynamics of the recombination mechanism of electron and hole could be understood by the analysis of photoluminescence. This is because when an electron-hole pair is generated upon photon excitation, their return to equilibrium could involve both radiative and nonradiative processes. The degree of photoluminescence and its dependence on the level of photo-excitation and temperature are directly related to the dominant recombination process [18].

2.2.7 Impurity levels and defect detection.

Radiative transitions in semiconductors also involve localized defect levels. The photoluminescence energy associated with these levels can be used to identify specific defects.

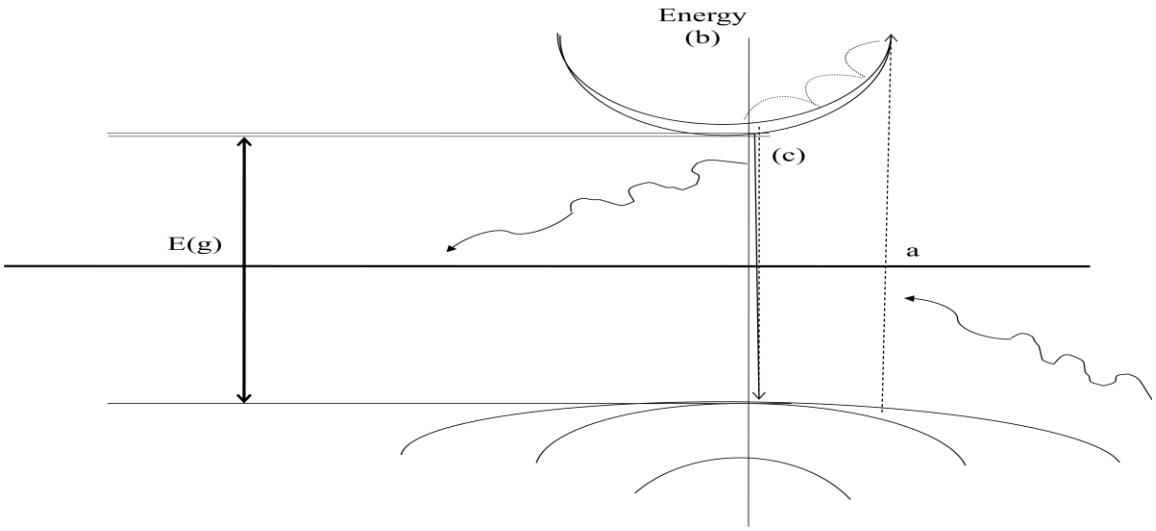

Figure 2.1: Photoluminescence schematic. (a) An electron absorbs a photon and is promoted from the valence band to the conductance band (b) The electron cools down to the bottom of the conduction band. (c) The electron recombines with the hole resulting in the emission of light with energy *hv*

2.3 Electron spectroscopy

2.3.1 X-ray photoelectron spectroscopy

X-Ray photoelectron spectroscopy (XPS) is a surface sensitive analytical technique. It is used to obtain chemical information about the surfaces of solid materials and measures the elemental composition, chemical state and electronic state of the elements that exist within a material [19].

XPS requires an ultra high vacuum (UHV) environment. X-rays are used to eject the electrons from the core shell of a sample atom and emitted electrons are analyzed according to their kinetic energies. The energy of a photoemitted core electron is a function of its binding energy and is characteristic of the element from which it was emitted.

When an X-ray beam is directed towards the sample surface, the energy of the X-ray photon is

adsorbed completely by the core electron of an atom. If the photon energy $h\nu$, is large enough, the core electron will then escape from the atom and emit from the surface. The emitted electron with the kinetic energy of E_k is referred to as the photoelectron. Energy analysis of the emitted photoelectrons is the primary data used for XPS [20]. The binding energy of the core electron is give by the Einstein relationship:

$$E_b = h\nu - E_k - \phi \quad \text{..... (2.3)}$$

Where $h\nu$ is the X-ray photon energy (for monochromatic Al Ka, $h\nu$ = 1486.6eV); E_k is the kinetic energy of photoelectron, which can be measured by the energy analyzer; and ϕ is the work function induced by the analyzer, about 4~5eV. Since the work function, ϕ, can be compensated artificially, it is eliminated, giving the binding energy as follows:

$$E_b = h\nu - E_k \quad \text{..... (2.4)}$$

The core electron of an element has a unique binding energy. This seems like a "fingerprint" because each element produces a unique set of electrons with specific energies. By measuring the number of these electrons as a function of kinetic (or binding) energy, an XPS spectrum is obtained. Thus almost all elements except for hydrogen and helium can be identified *via* measuring the binding energy of its core electron [21]. Furthermore, the binding energy of the core electron is very sensitive to the chemical environment of element. The same atom is bonded to the different chemical species, leading to the change in the binding energy of its core electron. The variation of the binding energy results in the shift of the corresponding XPS peak. This ranges from 0.1eV to 10eV [22]. This effect is termed as "chemical shift", which can be applied to studying the chemical status of element in the surface. Therefore, XPS is also known as electron spectroscopy for chemical analysis (ESCA). Since it supplies information about the

atomic composition of the surface and chemical environments (i.e. binding states, oxidation states) of elements, it is therefore a key research method for nanostructured materials where the nano-effect is related with surface activity.

2.4 Structural characterization

2.4.1 X-Ray Diffraction

X-rays are electromagnetic radiation with typical photon energies in the range of 100eV-100keV. Beign an electromagnetic radiation, they create diffraction effects when they impinge on periodic structures with geometric variations on the length scale of the wavelength of the radiation. Crystals and molecules have an interatomic distance of 0.15-0.4 nm and this corresponds with the wavelength of X-rays in the electromagnetic spectrum. For diffraction application, only short wavelength X-rays (hard X-rays) of wavelength in the range of few angstroms to 0.1 angstroms (1 keV-120keV) are used [23].

X-ray analysis provides information on the crystal structure, the structural phase of the nanocrystal and also an estimate of the size of the nanocrystals. X-ray diffraction broadening is of great value for nanocrystallites because the finite size of the crystallites has a marked effect on X-ray diffraction lines. Scherrer formular [24] is used for the estimation of the particle size of the crystallites from the width of the diffraction line corresponding to a particular (*hkl*). To understand the origin of the broadenings of the diffraction peaks due to the finite size effect, it is necessary to consider the effect of diffraction from a finite number of planes as shown schematically in Figure 2.2.

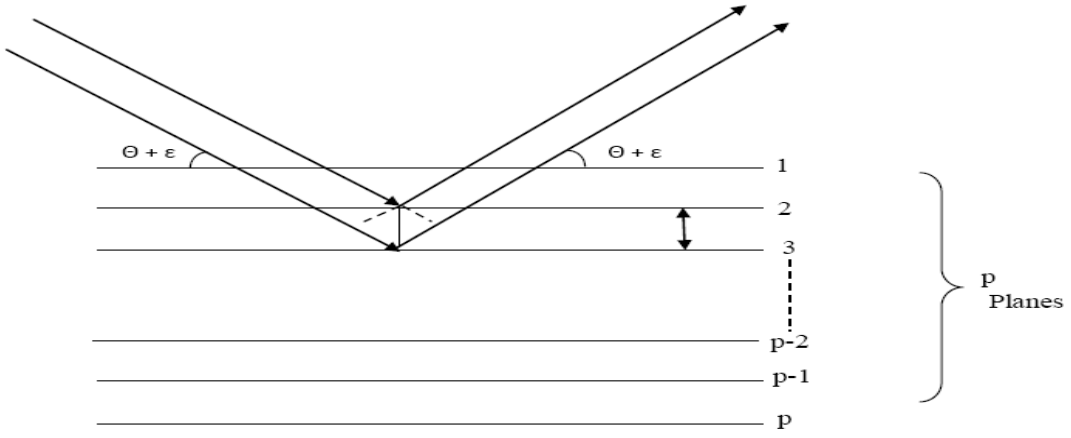

Figure 2.2: The effect of diffraction from a finite number of planes

If we consider an ideal crystal having p atomic (hkl) planes of spacing d parallel to the surface, the approximate thickness of the crystal is close to pd. The amplitude of a diffracted ray will be maximum when the path difference between the rays reflected from successive planes is equal to a multiple of the wavelength

$$\delta l = 2d\sin\theta = n\lambda \quad \ldots\ldots\ldots\ldots\ldots\ldots\ldots\ldots\ldots\ldots\ldots\ldots\ldots\ldots\ldots\ldots\ldots\ldots \quad (2.5)$$

When the incident angle differs from θ by a small amount ϵ, the resulting path difference is given by

$$\delta l = 2d\sin(\theta+\epsilon) = 2d\,sin\theta\,cos\epsilon + 2d\,sin\epsilon\,cos\theta = n\lambda\,cos\epsilon + 2d\,sin\epsilon\,cos\theta \quad \ldots\ldots\ldots (2.6)$$

Since, ϵ is small, the above expression can be written as

$$\delta l = n\lambda + 2\epsilon d\cos\theta \quad \ldots\ldots\ldots\ldots\ldots\ldots\ldots\ldots\ldots\ldots\ldots\ldots\ldots\ldots\ldots\ldots\ldots\ldots \quad (2.7)$$

The corresponding phase difference between the first and the pth plane is given by

$$\emptyset = \frac{4\pi p\epsilon d\,cos\theta}{\lambda} \quad \ldots\ldots\ldots\ldots\ldots\ldots\ldots\ldots\ldots\ldots\ldots\ldots\ldots\ldots\ldots\ldots\ldots\ldots \quad (2.8)$$

The resultant amplitude of the reflected wave is given by the vector sum of the amplitude of each of the p vectors successive differing by increasing phase of $\emptyset$, by

$$A = \frac{\alpha p \sin\,(2\pi p\epsilon d\cos\,\theta/\lambda}{2\pi p\epsilon d\cos\theta/\lambda} \quad \ldots\ldots\ldots\ldots\ldots\ldots\ldots\ldots\ldots\ldots\ldots\ldots\ldots \quad (2.9)$$

The amplitude of the reflected ray is maximum when $= 0$; in this case $A_O = \alpha p$. The full width at half the maximum intensity can be calculated by

$$\frac{A^2}{{A_O}^2} = \frac{\sin^2(\emptyset/2)}{(\emptyset/2)^2} = \frac{1}{2} \quad \ldots\ldots\ldots\ldots\ldots\ldots\ldots\ldots\ldots\ldots\ldots \quad (2.10)$$

The above equation holds when

$$\frac{\emptyset}{2} = \pm\, 1.4$$

or using equation 2.6,

$$\frac{4\pi p\epsilon d\cos\,\theta}{2\lambda} = 1.40 \quad \ldots\ldots\ldots\ldots\ldots\ldots\ldots\ldots\ldots\ldots\ldots\ldots \quad (2.11)$$

The full width at half maximum, β_{hkl}, for the diffraction peak at an angle 2θ, is then given by

$$\beta_{hkl} = 4\epsilon = \frac{0.89\,\lambda}{pd\,\cos\theta} = \frac{0.89\lambda}{L_{hkl}\cos\theta} \quad \ldots\ldots\ldots\ldots\ldots\ldots \quad (2.12)$$

The above expression is known as Scherrer formula. The grain size of the nanoparticle could be determined from the X-ray diffraction pattern using the Scherrer equation [24].

2.5 Microscopic analysis

Microscopic analysis is critical to the analysis and studies of nanoparticles. Among many characterization techniques, it should and will play an important role in understanding the nature of nanosystems. It is almost always the first method used to determine the size and size distribution of nanoparticles and provides the most direct proof for the formation of nanocrystals [25]. Microscopy and the associated analytical techniques can provide information on the physicochemical properties of individual nanocomponents as well as the spatial relationships among these nanocomponents [30].

2.5.1 Transmission electron microscope (TEM)

Transmission electron microscopy (TEM) is used to determine the shape, size and size distribution of nanoparticle samples. It is almost always the first method used for this determination [26]. The advantages that TEM offers are the high magnification of the spatial information in the signal by as little as 50 times to as much as a factor of 10^6, and also the ability to provide both image and diffraction information from a single sample. The high magnification or resolution of all TEM is a result of the small effective electron wavelengths, λ, which is given by the de Broglie relationship:

$$\lambda = \frac{h}{\sqrt{2mqv}} \quad \ldots\ldots\ldots\ldots\ldots\ldots\ldots\ldots\ldots\ldots\ldots\ldots\ldots\ldots\ldots\ldots \quad (2.13)$$

Where m and q are the electron mass and charge, h is Planck's constant, and v is the potential difference through which electrons are accelerated. The signal in TEM is obtained from both undeflected and deflected electrons that penetrate the sample thickness [27], which therefore

must be very thin. The scattering processes experienced by electrons during their passage through the specimen determine the kind of information obtained. Elastic scattering involves no energy loss and gives rise to diffraction patterns. Inelastic interactions between primary electrons and sample electrons at heterogeneities such as grain boundaries, dislocations, second-phase particles, defects, density variations, etc., cause complex absorption and scattering effects, leading to a spatial variation in the intensity of the transmitted electrons.

One shortcoming of TEM is its limited depth resolution. Electron scattering information in a TEM image originates from a three dimensional sample, but is projected onto a two-dimensional detector. The collapse of the depth scale onto the plane of the detector therefore implies that structural information along the beam direction is superimposed at the image plane [27].

In addition to the capability of TEM for structural characterization and chemical analyses, TEM has been also explored for other applications in nanotechnology. Example of these is in the determination of melting points of nanocrystals, in which, an electron beam is used to heat up the nanocrystals and the melting points are determined by the disappearance of electron diffraction [28]. High resolution TEM (HRTEM) provides lattice-resolved images of the nanocrystals and can be used to study the defects in the nanocrystals or phase transitions, if any, in the nanocrystals. A unique capability to determine the crystal structure of individual nanomaterials, such as nanocrystals and nanorods, and the crystal structures of different parts of a sample is found in selected-area diffraction (SAD). Here, the condenser lens is defocused to produce parallel illumination at the specimen and a selected-area aperture is used to limit the diffracting volume. SAD patterns are often used to determine the Bravais lattices and lattice parameters of

crystalline materials by the same procedure used in XRD [29].

2.5.2 Scanning electron microscopes (SEM)

Scanning electron microscopes (SEM) is used for inspecting the topographies of sample materials and also provide the chemical composition information near the surface. It possesses a magnification range that encompasses that of optical microscopy and extends it to the nanoscale. Thus SEM is one of the most widely used techniques in characterization of nanomaterials and nanostructures [30].

Signal generation in SEM is a result of the interaction between the incident electron beam and a thin surface layer of the sample, which depends on the beam energy. When an electron beam strikes a sample, a number of interactions occur that result in the emission of a variety of electrons, photons and phonons. Other signals can also be generated (Fig. 2.3). The principle images produced in the SEM are of three types: secondary electron images, backscattered electron images and elemental X-ray maps (Fig. 2.3). The interaction is due to the fact that the primary electrons are charged particles which can interact strongly with the electrically charged particles of the atoms in the sample, i.e. both with negatively charged electron clouds and positively charged nuclei. The interaction is said to be *inelastic* if some of the energy of the primary electron is lost during the interaction. If no energy is lost the interaction is said to be *elastic* [31].

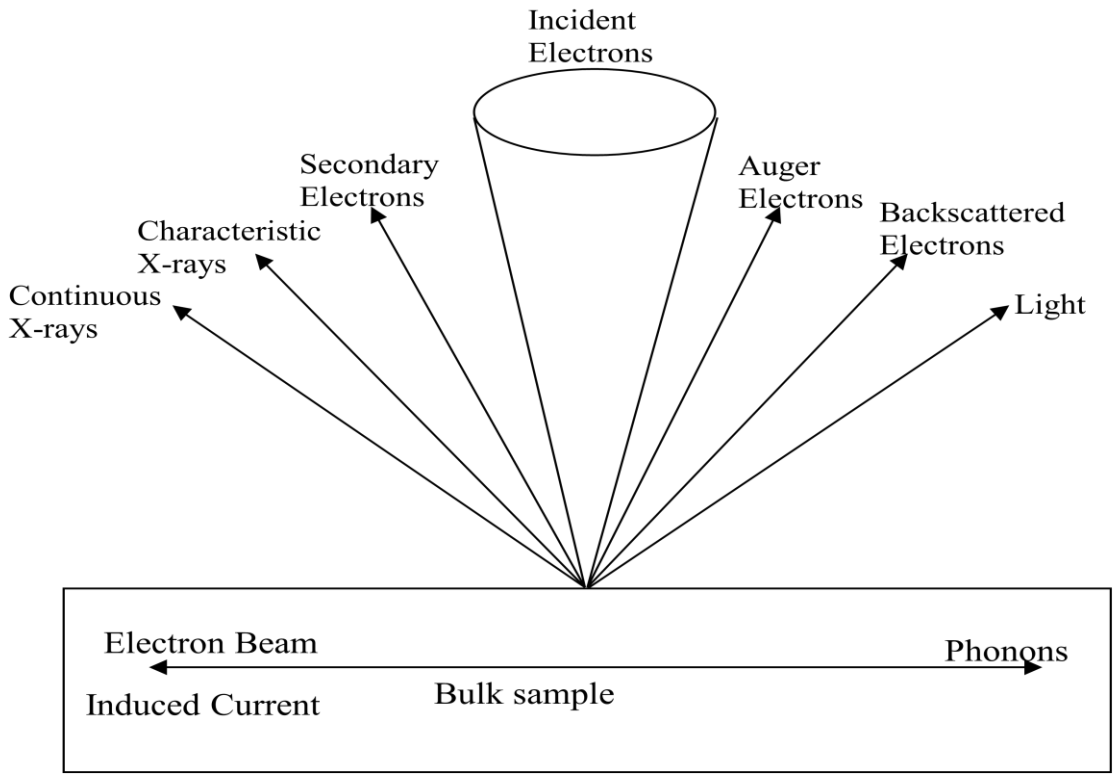

Figure 2.3: Schematic drawing illustrating the signals generated inside a scanning electron microscope when an electron beam interacts with a specimen [30]

SEM gives the following information on the nanoparticles:

Topography: The surface features of the nanoparticles or "how they look", their texture; detectable features limited to a few nanometers

Morphology: The shape, size, arrangement of the particles and the sample composition that is on the surface or has been exposed.

Composition: SEM can also provide detailed information on the chemical composition and distribution vis-a-vis the elements and compounds that the sample is composed of and their

relative ratios. When an inner-shell electron makes a transition from a higher to a lower energy level, an x-ray photon is emitted, whose energy ($hf = hc/\lambda$) is equal to the difference in the two quantum levels. By identifying the wavelengths or photon energies present, the chemical (more correctly: elemental) analysis of the sample could be performed. The electrons that are useful for analytical purpose are not the outer (valence) electrons but rather the inner-shell electrons. Because the latter do not take part in chemical bonding, their energies are unaffected by the surrounding atoms and remain indicative of the nuclear charge and therefore atomic number [32].

References

1. Walker, B.G.; Hendy, S.C.; Gebauer, R.; Tilley, R.D. Application of Lanczos-base timedependent density-functional theory approach to semiconductor nanoparticle quantum dots. *Eur*. *Phys*. *J*. *B*. **2008,** 66, 7-15.

2. Blaha, P.K.; Schwarz, P.; Sorantin, A.; Trickey, S.B. Full-potential, linearize augmented plane wave programs for crystalline systems. *Comput*. *Phys*. *Commun*. **1990**, 59, 399-415.

3. Andersen, O.K.; Saha-Dasgupta, T. Muffin-tin orbitals of arbitrary order. Phys Rev. B **2000**, 62, R16219-R16222.

4. Dronskowski, R.; Blochl, P.E. Crystal orbital Hamilton populations (COHP): Energy resolved visualization of chemical bonding in solids based on density-functional calculations. *J. Phys. Chem*. **1993**, 97, 8617-8624.

5. Cao, G. Nanostructures & nanomaterials synthesis, properties and applications. *Imperial College Press.* **2004**.

6. Alivisatos, A.P. Perspectives on the physical chemistry of semiconductor nanocrystals. *J. Phys*. *Chem*. **1996**, 100, 13226-13239.

7. Rohatgi-Mukherjee, K.K. Fundamentals of Photochemistry, Wiley Eastern Ltd.**1986**.

8. Pankove, J.I. Optical processes in semiconductors, New York: Dover Publications. **1975**.

9. Sirohi, S.; Kumar, V.; Sharma, T.P. Optical, structural and electrical properties of CdTe sintered films. *Opt.Mater*. **1999**, 12, 121-125.

10. Saha, S.; Pal, U.; Chaudhuri, A.K; Rao, V.V.; Banerjee H.D. *Phys*. *Stat*. *Sol*. A 14, **1989**, 14, 721-729.

11. Davies, J.H. The physics of low dimensional semiconductors. Cambridge University Press, Cambridge, **1989**.

12. Vijayan, N.; Bhagavannarayana, G.; Budakoti, G.C.; Kumar, B.; Upadhyaya, V.; Subhasis, D. Optical, dielectric and surface studies on solution grown benzimidazole single crystals. *Mater*. *Lett*. **2008**, 62, 1252-1254.

13. Yu, P.Y.; Cardona, M. Fundamentals of semiconductors: physics and materials properties, third, revised and enlarged edition, springer, Berlin, **1995**.

14. Singha, A.; Dhar, P.; Anushree, R. A non-destructive tool for nanomaterials: Raman and photoluminescence spectroscopy. *Am. J. Phys.* **2005**, 73, 224-233.

15. Vishwakarma, K.; Vishwakarma, O.P.; Ramrakhiani, M. Synthesis and photoluminescence studies on nanocrystalline content Cds film. *Int. J. Nanotech*. Appl. **2010**, 4, 1-5.

16. SuryaNarayana, C. Institute for materials and advance process, University of Idaho, Moscow, **1994**.

17. Yoffe, A.D. Low-dimensional systems: quantum size effects and electronic properties of semiconductor microcrystallites (zero-dimensional systems) and some quasi-two-dimensional systems. *Adv*. *Phys*. **2002**, 51, 799-890.

18. Khan, A. Synthesis, characterization and luminescence properties of ZnO nanostructures,

Ohio University, **2006**.

19. Handbook of Analytical Methods for Materials. Mater. Evaluat. Eng. Inc. **2001**.

20. Moulder, J.F.; Stickle, W.F.; Sobol, P.E.; Bomben, K.D. Handbook of X-ray photoelectron Spectroscopy, Physical electronics. Inc. Eden prairie, Minnesota, **1995**.

21. Grant, J. T.; Briggs, D. Surface analysis by Auger and X-ray photoelectron spectroscopy, ed. IM publications, Chichester, UK, **2003**.

22. Baláž, P. Selected identification methods. Mechanochemi. *in Nanosci. and Miner Eng*. **2008** 133-175.

23. Warren, B.E. X-Ray Diffraction, Addison-Wesley, Reading, MA, **1969**.

24. Cullity, B.D. Elements of X-ray diffraction, Addison-Wesley publishing company Inc. **1978**.

25. Baker, T.N. Microstructure of high temperature materials, 5, **2001**, 161-189.

26. Miller, B.V.; Lines R.W. Recent advances in particle size measurements: a critical review. *Crit*. *Rev. Anal*. *Chem*. 20, **1988**, 75-116.

27. William, D.B.; Carter, B.C. Transmission electron microscopy. A text book for material science *Springer*, **1996**, Plenum Press, New York. 3-16.

28. Sickafus, K. Transmission electron microscopy in encyclopedia of material Characterization by Butxetworch-Heinemann, (USA) Inc. **1992**.

29. Goldstein, A.N.; Echer, C.M.; Alivisatos, A.P. Melting in semiconductor nanocrystals. *Sci.*

1992, 256, 1425-1427.

30. Cullity, B.D.; Stock S.R. Elements of X-ray Diffraction, 3rd Edition, Prentice

Hall, Upper Saddle River, N J. **2001**.

31. Yao, N.; Wang, Z.L. Handbook of microscopy for nanotechnology. Kluwer Academic Publishers **2005**.

32. Michler, G.H. Electron microscopy of polymers. Springer-Verlag Berlin Heidelberg. **2008**.

CHAPTER THREE

3. EXPERIMENTAL

3.1 Chemicals and solvents

Commercial reagents were used as acquired. 1,4-dioxane, diethyl ether, methanol and ethylcyanoacetate were purchased from Sigma Aldrich. The diethyl ether procured from Merck were of analytical grade and used without further purification. Anhydrous KOH, $ZnCl_2$ and $HgCl_2$ were purchased from Sigma Aldrich chemicals and were used as received. Potassium salt of 1-ethoxylcarbonyl-1-cyanoethylene-2,2-dithiolate was prepared according to literature procedure [1].

3.2 Physical measurements

3.2.1 Melting point determination

Melting point was determined using a Gallenkcamp electrothermal melting point apparatus.

3.2.2 Elemental analysis

Elemental analysis for the components was performed on a Fission elemental analyser.

3.2.3 Infrared spectroscopy

Infrared spectroscopy was collected (4000-370 cm^{-1}) as KBr discs on a Perkin Elmer Paragon 2000 spectrophotometer equipped with CSI window and beamsplitter.

3.2.4 ^{1}H and ^{13}C-NMR spectroscopy

Nuclear Magnetic Resonance (NMR) spectra were run on a Bruker EMX 400 MH_2 spectrometer for ^{1}H and 100 MH_2 for ^{13}C. The chemical shift values were reported in parts per million (ppm) relative to tetramethyl silane (TMS) as internal standard. Chemical shifts were also reported with respect to DMSO d_6 at δc 40.98 and DMSO d_6 at δ_H 2.50 or $CDCl_3$ at δc 77.30 and δ_H 7.24 ppm.

3.2.5 UV-Visible spectroscopy

The electronic spectra of the complexes in solution were run in the range 180-1100 nm on Perkin Elmer Lamda 25 spectrophotometer. The sample were placed in quarts cuvettes of 1 cm path length. The solvents used varied and it depends on the solubility of the complexes in a particular solvent and its stability. In all cases, HPLC grade solvents were used for solution measurements.

3.2.6. Thermogravimetry analysis

Thermogravimetry/differential thermal analysis (TGA/DTA) was carried out using Perkin Elmer thermogravimetry analyzer (TGA 7) equipped with a thermal analysis controller (TAC7/DX) and under a dynamic N_2 atmosphere at a flow rate of 50 mL/min and heating rate 20 ºC/min.

3.3 Synthesis of the potassium salt of 1-ethoxylcarbonyl-1-cyanoethylene-2,2-dithiolate, [K_2ecda]

Pulverized potassium hydroxide (0.01 mol, 0.5611g) was suspended in dioxan (50 mL) and a solution of ethyl cyanoacetate (0.005 mol, 5.406 mL) and carbon disulfide (0.005mol, 3.02 mL) in dioxan (25 mL) was added with stirring and cooling to maintain a temperature of 15-20 ºC. The suspension was stirred for another 20 mins and diluted with 125 mL of diethyl ether. The yellow precipitate was filtered, washed with dioxan-ether (1:1) and dried in vacuo over NaOH and P_2O_5.

Equation of the reaction:

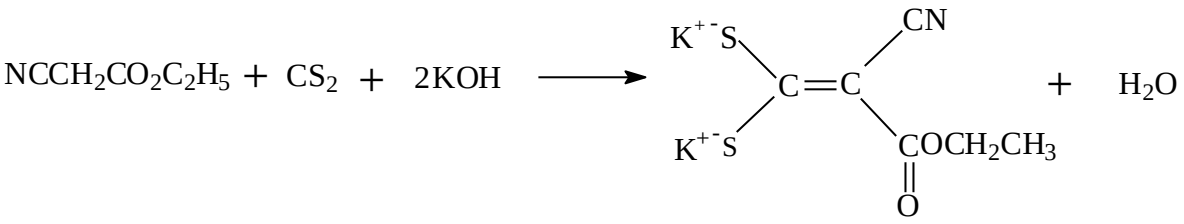

Yield: 13.70 g (99.8 %). Selected IR, ν(cm^{-1}): 2165 (C≡N), 1681 (C=O), 1441 (C=S_2).

3.4. Synthesis of metal complexes of methylthiourea and 1-ethoxylcarbonyl-1-cyanoethylene-2,2-dithiolate [M(mtu)$_2$ecda] where (M= Zn, Cd and Hg)

3.4.1 Synthesis of [Zn(mtu)$_2$ecda]

$ZnCl_2$ (0.6814 g, 0.005 mol) was dissolved in 40 mL of absolute methanol and refluxed for 3 h with (0.9015 g 0.01 mol) of methylthiourea dissolved in 40 mL of methanol. K_2ecda (1.417 g,

0.005 mol) was dissolved in 20 mL of methanol and added to the refluxing mixture. The initial colourless mixture changes to milky yellow and the reaction was further refluxed for 8h. The milky yellow product obtained by filtration was washed twice with ice cold methanol, water and diethyl ether. It was also re-dissolved in acetone and filtered to remove KCl which is the by - product of the reaction. The acetone was concentrated in vacuo to obtain the product.

Yield: 1.31 g (60.98 %), m.p. 208-210 ^{o}C.

^{1}H-NMR (DMSO) δ = 1.15 (t, 3H-CH_3), 2.79 (q, 3H-CH_2),

^{13}C-NMR (DMSO) δ = 206.20 (C=S), 163.90 (C=O), 120.74 (C≡N), 90.88 (C=C), 58.35 (-OCH_2), and 14.54 (-CH_3)

Selected IR, ν(cm^{-1}): 2205 (C≡N), 1412 ($C=S_2$), 396 (M–S), 1671(C=O).

3.4.2 Synthesis of [Cd(mtu)$_2$ecda]

$CdCl_2$ (0.916 g, 0.005 mol) was dissolved in 40 mL of methanol and added to methylthiourea (0.9015 g, 0.01 mol) dissolved in 20 mL of methanol. The solution was refluxed for 3 h after which K_2ecda (1.417 g, 0.005 mol) dissolved in methanol was added to the mixture. The reaction was further refluxed for 8 h. The product was filtered and washed twice with ice cold methanol, water and ether. The product was re-dissolved in acetone and KCl removed with filteration after which the acetone was removed in vacuo to obtain the precipitate.

Yield: 1.9 g (91.6 %), m. p. 217-219 ^{o}C.

^{1}H-NMR (DMSO) δ = 1.15 (t, 3H-CH_3), 4.34 (q, 3H-OCH_3), 2.80 (t, 3H-OCH_2CH_3)

^{13}C-NMR (DMSO) δ = 208.57 (C=S), 164.74 (C=O), 121.65 (C≡N), 90.27 (C=C), 58.26 (-

OCH_2) and 14.58 CH_3.

Selected IR, $\nu(cm^{-1})$: 2199 (C≡N) ,1489 ($C=S_2$), 388 (M–S), 1652(C=O).

3.4.3 Synthesis of [Hg(mtu)$_2$ecda]

$HgCl_2$ (1.3575 g, 0.005 mol) in 40 mL of methanol was added to methylthiourea (0.9015 g, 0.01 mol) dissolved in 20 mL of methanol and refluxed for 3h. The mixture gave a colourless clear solution which turned initially to brown on addition of K_2ecda (1.417 g, 0.005 mol) dissolved in 20 mL of methanol. After a period of 15 mins the colour of the mixture changed to grey and finally changed to black. The reaction was stirred further for 8 h, filtered and washed twice with ice cold methanol, water and diethyl ether. It was further re-dissolved in acetone and filtered to remove KCl by-product. The acetone was removed in vacuo to obtain analytical pure products.

Yield: 1.7 g (60.28 %), m. p. 247-249 ^oC.

^{1}H-NMR (DMSO) δ = 1.27 (t, 3H-CH_3), 4.31 (q, 2H, -OCH_2).

^{13}C-NMR (DMSO) δ = NA (Not available due to insolubility problem).

Selected IR, $\nu(cm^{-1})$: 2199 (C≡N),1489 ($C=S_2$), 388 (M–S), 1652 (C=O).

3.5 Synthesis of metal complexes of diethylthiourea and 1-ethoxylcarbonyl-1-cyanoethylene-2,2-dithiolate complexes. ($M(detu)_2ecda$) where (M= Zn, Cd and Hg)

3.5.1 Synthesis of [$Zn(detu)_2ecda$]

$ZnCl_2$ (0.681 g, 0.005 mol) was dissolved in 40 mL of methanol and added to diethylthiourea (1.3223 g, 0.01 mol) dissolved in 40 mL of methanol. The mixture was refluxed for 3 h and it gave a white yellowish colour on the addition of K_2ecda (1.417 g, 0.005 mol) in 20 mL of methanol. The mixture was further refluxed for 8 h, washed twice with ice cold methanol, water and diethyl ether. The product was re-dissolved in acetone, filtered to remove KCl as by-product and the solvent removed in vacuo to obtain the products.

Yield: 1.42 g (54.9 %), m. p. 227-229 ^oC.

^{1}H-NMR (DMSO) δ = 2.78 (s, 3H -NH-CH_3), 1.16 (t, 3H -OCH_2CH_3), 3.97 (q, 2H, -OCH_2)

^{13}C-NMR (DMSO) δ = 206.23 (C=S), 163.87 (C=O), 120.76 (C≡N), 90.84 (C=C), 58.32 (-OCH_2) and 14.53 (-CH_3).

Selected IR, ν(cm^{-1}): 2200 (C≡N), 1462 ($C=S_2$), 373 (M–S), 1681 (C=O).

3.5.2 Synthesis of [$Cd(detu)_2ecda$]

$CdCl_2$ (0.917 g, 0.005 mol) was dissolved in 40 mL of methanol and added to diethylthiourea (1.322 g, 0.01 mol) dissolved in 40 mL of methanol. The mixture was refluxed for 3 h. The clear solution gave a yellow colour on the addition of K_2ecda (1.417 g, 0.005 mol) which was dissolved in 20 mL of methanol. The mixture was refluxed further for 8 h, filtered and the product dissolved in acetone to obtain KCl which was the by-product of the reaction and the acetone evaporated leaving the precipitate as the product.

Yield: 2.00 g (77.3 %), m. p. 231-233 ^{o}C.

^{1}H-NMR (DMSO) δ = 1.16 (t, 3H -OCH_2CH_3), 3.99 (q, 2H, -OCH_2)

^{13}C-NMR (DMSO) δ = 208.15 (C=S), 121.57 (C≡N), 90.25 (C=C), 58.49 (-OCH_2) and 14.57 (-CH_3).

Selected IR, ν(cm^{-1}): 2206 (C≡N), 1463(C = S_2), 372 (M–S), 1651 (C=O).

3.5.3 Synthesis of [Hg(detu)2ecda]

$HgCl_2$ (1.358 g, 0.005 mol) was dissolved in 40 mL of methanol which was added to diethylthiourea (1.042 g, 0.01 mol) in 40 mL of methanol and refluxed for 3 h. The mixture gave a clear colourless solution which turned initially to brown on addition of K_2ecda (1.417 g, 0.005 mol) in 40 mL methanol. After a period of 15 mins the colour of the mixture changed to grey and finally changed to black. The product was filtered and the filterate re-dissolved in acetone to remove KCl. The product was obtained as precipitate on evaporation of the acetone.

Yield: 2.1 g (64.0 %), m. p. 344-346 ^{o}C.

^{1}H-NMR (DMSO) δ = 1.13 (t, 3H -OCH_2CH_3),

^{13}C-NMR (DMSO) δ = NA.(Not available due to insolubility problem)

Selected IR, ν(cm^{-1}): 2188 (C≡N), 1458 (C=S_2), 375 (M–S), 1458 (C=S_2), 1651 (C=O).

3.6 Synthesis of dimethylthiourea $(dmtu)_2$ and 1-ethoxylcarbonyl-1-cyanoethylene-2,2-dithiolate(ecda) complexes. ($M(dmtu)_2ecda$) where (M= Zn, Cd and Hg)

3.6.1 Synthesis of $[Zn(dmtu)_2ecda]$

$ZnCl_2$ (0.681 g, 0.005 mol) was dissolved in 40 mL of methanol and added to dimethylthiourea (1.042 g, 0.01 mol) in 40 mL of methanol. The clear solution turned milky colour on adding K_2ecda (1.417 g, 0.005 mol) which was dissolved in 20 mL of methanol. The reaction was refluxed further for 8 h and filtered. The product was re-dissolved in acetone, filtered to remove KCl and the filterate concentrated in vacuo to obtain the final product.

Yield: 1.421 g (61.65 %), m. p. 210-212 ^oC.

^{1}H-NMR (DMSO) δ = 1.04 (s, 3H -NH-CH_3), 1.15 (t, 3H -CH_3), 3.98 (q, 2H -OCH_2).

^{13}C-NMR (DMSO) δ = 206.24 (C=S), 163.85 (C=O), 120.79 (C≡N), 90.83 (C=C), 58.31 (-OCH_2), and 14.54 (-CH_3).

Selected IR, ν(cm^{-1}): 2209 (C≡N), 1458 ($C=S_2$), 375 (M–S), 1656 (C=O).

3.6.2 Synthesis of $[Cd(dmtu)_2ecda]$

$CdCl_2$ (0.917, 0.005 mol) was dissolved in 40 mL of methanol and added to dimethylthiourea (1.042, 0.01mol) in 40 mL of methanol. The mixture was refluxed for 3 h. The clear solution gave a yellow colour on adding K_2ecda (1.417 g, 0.005 mol) which was dissolved in 20 mL of methanol. The reaction mixture was refluxed further for 8 h, filtered and the product re-dissolved in acetone to remove KCl by product. The filtrate was concentrated in vacuo to obtain the product.

Yield: 1.62 g (67.55), m. p. 221-223 ^{o}C.

^{1}H-NMR (DMSO) δ = 2.79 (s, 3H-NH-CH_3), 1.15 (t, 3H -CH_3), 3.99 (q, 2H, -OCH_2)

^{13}C-NMR (DMSO) δ = 207.79 (C=S), 165.49 (C=O), 121.40 (C≡N), 90.44 (C=C), 58.63 (-OCH_2) and 14.54 (-CH_3).

Selected IR, ν(cm^{-1}): 2209 (C≡N), 1473(C=S_2), 377 (M–S), 1629 (C=O).

3.6.3 Synthesis of [Hg(dmtu)$_2$ecda]

$HgCl_2$ (1.358 g, 0.005 mol) was dissolved in 40 mL of methanol and added to dimethylthiourea (1.042 g, 0.01 mol) dissolved in 40 mL of methanol. The reaction mixture was refluxed for 3 h. K_2ecda (1.417 g, 0.005 mol) dissolved in methanol was added to the clear colourless solution. After a period of 15 mins the colour of the mixture changed to grey and finally to black. The reaction was refluxed further for 8 h, filtered and the product dissolved in acetone to remove KCl. The filterate was concentrared in vacuo to give obtain the product.

Yield: 1.6 g (53.67 %), m. p. 210-212 ^{o}C.

^{1}H-NMR (DMSO) δ = 1.15 (t, 3H -CH_3),

^{13}C-NMR (DMSO) δ = NA (Not available due to partial insolubility problem)

Selected IR, ν(cm^{-1}): 2202 (C≡N), 1459 (C=S_2), 378 (M–S), 1649 (C=O).

3.7 Synthesis of metal complexes of tetramethylthiuram disulfide, (tmtd), and 1-ethoxylcarbonyl-1-cyanoethylene-2,2-dithiolate (M(tmtd)ecda) where (M= Zn, Cd and Hg)

3.7.1 Synthesis of [Zn(tmtd)ecda]

$ZnCl_2$ (0.681 g, 0.005 mol) was dissolved in 30 mL of methanol was added to tetramethyl thiuram disulfide (1.202 g, 0.005 mol) dissolved in 30 mL of methanol. The mixture was refluxed for 4 h. It gave a colourless solution and K_2ecda (1.417 g, 0.005 mol) dissolved in 30 mL methanol was added. The colour changed immediately to whitish yellow and the reaction was refluxed further for 8 h. The product was filtered hot and re-dissolved in acetone to remove KCl by-product. The precipitate was recovered by allowing the acetone to evaporate at room temperature and the product was washed with methanol and diethyl ether.

Yield: 1.59 g (75.1 %), m. p. 315-317 ^{o}C.

^{1}H-NMR (DMSO) δ = 1.05 (t, 3H -NH-CH_3) 4.02 (q, 2H, -OCH_2)

^{13}C-NMR (DMSO) δ = 203.69 (C=S), 168.68 (C=O), 122.94 (C≡N), 59.29 (-OCH_2).

Selected IR, ν(cm^{-1}): 2245(C≡N), 1455 (C=S_2), 382 (M–S), 1732 (C=O).

3.7.2 Synthesis of [Cd(tmtd)ecda]

$CdCl_2$ (0.917 g, 0.005 mol) dissolved in 30 mL of methanol and added to tetramethyl thiuram disulfide (1.202 g, 0.005 mol) dissolved in 30 mL of methanol. The mixture was refluxed for 4 h. K_2ecda (1.417 g, 0.005 mol) dissolved in 30 mL methanol was added. The colour changed immediately to yellow and the reaction was refluxed further for 8 h. The product was filtered hot and the residue dissolved in acetone to remove the KCl. The filterate was concentrated in vacuo

and the final yellow product was washed with methanol and diethyl ether.

Yield: 1.58 g (72.8 %), m. p. 337–339 ^{o}C.

^{1}H-NMR (DMSO) δ = 1.27 (t, 3H, -OCH_2CH_3), 4.09 (q, 2H, -OCH_2)

^{13}C-NMR (DMSO) δ = 208 (C=S), 164 (C=O), 121.37 (C≡N), 90.6 (C=C), 14.6 (-CH_3), 58.5 (-OCH_2).

Selected IR, ν(cm^{-1}): 2233 (C≡N), 1512 (C=S_2), 384 (M–S), 1600 (C=O).

3.7.3 Synthesis of [Hg(tmtd)ecda]

$HgCl_2$ (1.357 g, 0.005 mol) was dissolved in 40 mL of methanol and was added to tetramethyl thiuram disulfide (1.202 g, 0.005 mol) dissolved in 30 mL of methanol and refluxed for 4 h. The resultant a colourless solution changed to brown on adding of K_2ecda (1.417 g, 0.005 mol) dissolved in 30 mL of methanol. The brown colour changed to grey and finally to black. The reaction was further refluxed for 8 h, filtered and the product dissolved in acetone to remove KCl by-product. The solvent was concentrated in vacuo, filtered and the final product washed with methanol and diethyl ether.

Yield: 1.9 g (91.6 %), m. p. 309-311 ^{o}C.

^{1}H-NMR (DMSO) δ = 1.23 (t, 3H-CH_3), 4.35 (q, 2H, -OCH_2).

^{13}C-NMR (DMSO) δ = NA (Not available because the compound settles down in the course of running the ^{13}C-NMR).

Selected IR, ν(cm^{-1}): 2244 (C≡N), 1492 (C=S_2), 449 (M–S), 1738 (C=O).

References

1. Jensen, K.A.; Henriksen, L. Studies of thioacids and their derivatives *Acta Chem. Scand*. **1968**, 22 (4), 1107-1128.

CHAPTER FOUR

4. CHARACTERIZATION AND THERMAL STUDIES OF THE METAL COMPLEXES

4.1 Introduction

Dithiolate ligands are unsaturated bidentate ligands where the two donor atoms are sulfur. They react with transition metals to form dithiolene complexes and some investigations have been done in this area of research [1, 2]. Metal complexes of dithiolene have excellent electronic functions as a result of their intermolecular charge transfer from ligand to ligand [3]. The ligand 1-ethoxylcarbonyl-1-cyanoethylene-2,2 dithiolate, ($ecda^{2-}$), is an anologue of maleonitriledithiolate(mnt^{2-}) which has electronic and material applications and the only difference between them is the substitution of the nitrile group with a large ester group in iso-maleonitriledithiolat,e (i-mnt^{2-}) [4]. This is expected to influence the magnetic and conducting properties of the ecda complexes. But despite the ease of synthesis, the molecular and material properties of the complex are limited. The high-nuclearity cluster possessing asymmetrically substituted 1, 1-dithiolate, $S_2CC(X)(Y)^{2-}$ are seldom characterize satisfactorily because of the difficulty in producing good quality crystals ammendable for X-ray diffraction which result in the presence of several isomeric species in solution caused by the asymmetrical 1, 1- dithiolate ligands and this impedes the subsequent detailed characterization for the isolated complexes [5]. The ligand shows exciting coordination properties by virtue of chelating and bridging behaviours which have been demonstrated in its binary and heterobimetallic complexes [6]. It exhibits strong π-delocalization and its complexes will probable display fascinating structural and solid state properties. The transition metal complexes of 1, 1-dithioligands form four-membered strained chelate rings while 1, 2-dithiolenes form less strained five-membered ring system. The

interest in dithiolate ligands is as a result of their stabilization of transition metal ions in their oxidation states, facile redox behaviour, and stabilization of a square planar geometry around the transition metal ions as well as interesting spectral and magnetic properties in catalysis [7]. This dithiolate ligand is used in the formation of chelate compounds in which the metal salts of transition metals are reacted with organic sulfur containing ligands. The chelate compounds contain ($M\text{-}S_n$) fragments that arise from the use of sulfides which also have applications in modern electronics and material science. The dithiolate chemistry of the Group 12 elements is limited to the +2 oxidation state. The ease and stability of the complexation reaction is due to the fact that Group 12 metals act as strong Lewis acids, and hence readily reacts with electron-rich sulfur containing ligands in the principle of hard–soft [Lewis] acid-base [8]. Structures of the ligands used in the present study are shown in Scheme 4.1, 4.2 and 4.3 are shown in Figures 4.1 and 4.2.

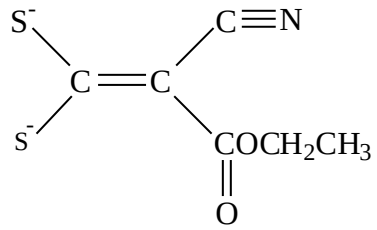

1-ethoxycarbonyl-1-cyanoethylene-2,2-dithiolate ($ecda^{2-}$)

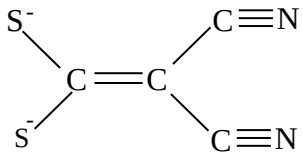

1, 1-dithio ligand, iso-maleonitriledithiolate ($i\text{-}mnt^{2-}$)

Figure 4.1: Structure of the dithiolate based ligands.

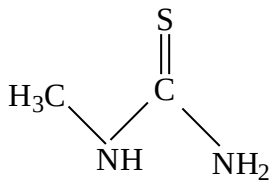

methylthiourea

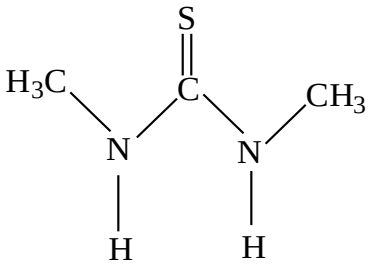

dimethylthiourea (dmtu)

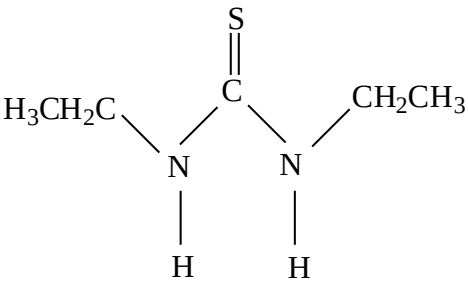

diethylthiourea (detu)

Figure 4.2: Structures of the thiourea ligands.

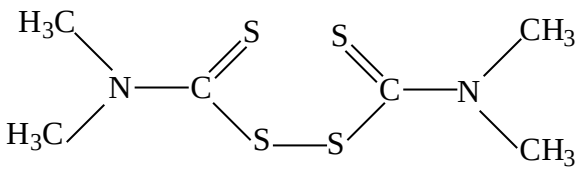

Figure 4.3: Structure of tetramethylthiuram disulfide (tmtd).

4.2 Results and discussion

4.2.1 Synthesis

Zn(II), Cd(II) and Hg(II) mixed ligands complexes were prepared by reacting the ligands (methylthiourea, dimethylthiourea or diethylthiourea) and 1-ethoxycarbonyl-1-cyanoethylene-2,2-dithiolate or tetramethylthiuram disulfide with the respective metal salts in 2:1:1 mole ratios. The complexes were isolated in good yield and are stable under ambient conditions. The complexes were characterized by elemental analyses, IR and NMR spectroscopy. The complexes were insoluble in most common solvents and thus made recrystallization and growing of suitable crystals for single crystals X-ray crystallography almost impossible. The analytical data for the complexes are presented in Table 4.1.

Table 4.1: Analytical data of synthesized compounds

Complex	Colour	M pt ^{o}C	Elemental analysis: Found/ (Calc.)			
			C	H	N	S
[Zn(mtu)$_2$ecda]	White	208-210	27.75 (28.09)	3.96 (4.15)	16.18 (16.22)	7.39 (7.43)
[Cd(mtu)$_2$ecda]	Yellow	247-249	24.95 (25.13)	3.56 (3.21)	14.59 (14.32)	26.72 (27.09)
[Hg(mtu)$_2$ ecda]	Black	236-238	21.41 (20.99)	3.02 (3.41)	12.33 (11.90)	22.57 (22.79)
[Zn(dmtu)$_2$ ecda]	Yellowish White	240-242	31.27 (31.52)	4.59 (5.07)	15.19 (15.26)	27.82 (27.79)
[Cd(dmtu)$_2$ecda]	Yellow	221-223	28.37 (28.14)	4.17 (4.10)	13.79 (13.82)	6.30 (6.28)
[Hg(dmtu)$_2$ecda]	Black	291-293	24.18 (24.21)	3.55 (3.45)	21.51 (21.52)	5.37 (5.43)
[Zn(detu)$_2$ecda]	Yellowish White	227- 229	37.28 (37.31)	5.67 (5.70)	13.59 (13.63)	24.83 (24.55)
[Cd(detu)$_2$ecda]	Yellow	231-233	34.07 (34.11)	5.18 (4.92)	12.42 (12.90)	22.73 (22.81)
[Hg(detu)$_2$ecda]	Black	278-280	29.46 (29.87)	4.48 (4.81)	10.74 (10.52)	19.66 (19.51)
[Zn(tmtd)ecda]	Yellowish White	230-232	29.33 (29.44)	3.49 (3.55)	8.56 (9.01)	39.08 (38.97)
[Cd(tmtd)ecda]	Yellow	322-324	26.62 (26.35)	3.17 (3.29)	7.77 (8.13)	35.47 (35.40)
[Hg(tmtd)ecda]	Black	325-327	22.90 (22.95)	2.72 (2.76)	6.68 (6.64)	30.50 (30.44)

4.3 Metal complexes of methylthiourea (mtu) and 1-ethoxylcarbonyl-1-cyanoethylene-2,2-dithiolate (ecda), [M(mtu)$_2$(ecda)]

The complexes were isolated by reacting metal salts of Zn(II), Cd(II) and Hg(II) with methylthiourea and ecda. Four coordinate geometries in which the metal ions are coordinated to two molecules of methylthiourea acting as monodentate ligand and one molecule of ecda acting as chelating bidentate ligand through the sulfur atoms is postulated for these complexes. A representative equation for the formation of the complexes is shown in Scheme 4.1. The complexes were characterized by melting point determination, elemental analyses, IR, ^{1}H- and ^{13}C-NMR spectroscopy. The complexes are not soluble in methanol, ethanol, hexane, chloroform, benzene and diethyl ether but they are sparingly soluble in acetonitrile and DMF and DMSO.

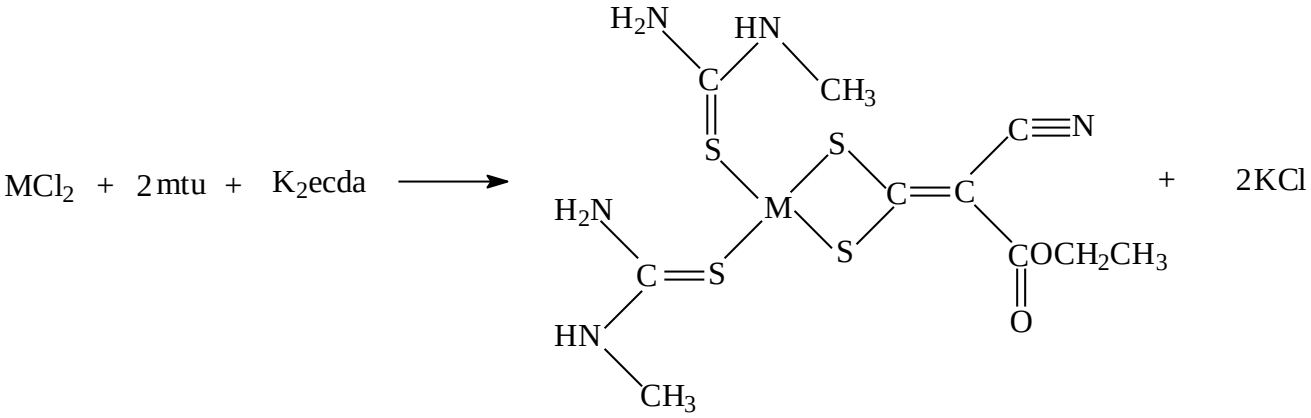

Scheme 4.1: Synthesis of [M(mtu)$_2$(ecda)], M = Zn, Cd, Hg.

4.3.1 Infrared spectra studies of the metal complexes: [M(mtu)$_2$(ecda)]

In order to clarify the mode of bonding and the effect of the coordination of the metal ions on the ligands, the IR spectra of the free ligands and their respective metal complexes were assigned on careful comparison. Relevant IR spectra for the ligands and the complexes were presented in

Table 4.2. The N-H stretching vibrations that occur at 3235 cm^{-1} in the methylthiourea shifted to about 3290 cm in the complexes. The shift might be due to hydrogen bonding in the complexes. Four main regions are of interest in 1-ethoxylcarbonyl-1-cyanoethylene-2,2-dithiolate complexes are: the 2188-2244 cm^{-1} due to ν(C≡N); 1645-1700 cm^{-1} due to ν(C=O); 1412-1492 cm^{-1} due ν(C=CS_2) and 1165-1116 cm^{-1} due to ν(C-S) of the chealted $ecda^{2-}$ [9]. In the uncoordinated $ecda^{2-}$ ligand these stretching vibrations were observed around 2161, 1680, 1441 and 1148 cm^{-1} while in the metal complexes, they were observed at 2198, 1630 , 1459 and 1148 cm^{-1} for [$Zn(mtu)_2ecda$] ; 2199, 1652, 1412 and 1174 cm^{-1} for [$Cd(mtu)_2ecda$] and 2232 , 1732 , 1489, 1201 cm^{-1} for [$Hg(mtu)_2ecda$]. The stretching vibrations that appear at 672 cm^{-1} in the free methylthiourea shifted to about 662 cm^{-1} in the metal complexes. The red shifting of the ν(C=S) bond of the free ligand confirm that methylthiourea is coordinated to the metal ions via the sulfur with a reduction of π-electron density of the ν(C=S) bond [10, 11]. The complexes show medium to weak ν(M-S) bands between 420 and 250 cm^{-1}.

Table 4.2: Relevant IR spectra of [$M(mtu)_2ecda$]

Complexes	ν(N-H)	ν(C≡N)	ν(C=O)	ν(C=S_2)	ν(C–S)	ν(C=S)	ν(M–S)
[$Zn(mtu)_2ecda$]	3274	2198	1630	1459	1148	671	376
[$Cd(mtu)_2ecda$]	3363	2199	1652	1412	1174/ 1148	671	396/ 461
[$Hg(mtu)_2ecda$]	3310	2232	1732	1489	1201	670	388

The υ(M-S) was observed at 376, 396 and 388 in [Zn(detu)$_2$ecda], [Cd(detu)$_2$ecda] and [Hg(detu)$_2$ecda] respectively. The presence of bands confirms the coordination of the ions to the sulfur atoms [10, 11].

4.3.2 NMR spectra of [Zn(mtu)$_2$ecda]

The ethoxyl proton is found at δ 3.96 ppm (predicted δ 4.20 ppm). A broad singlet peak at δ 2.80 ppm can be assigned as a methyl peak. At the upfield region of 1.15 ppm, was assigned to the methyl group attached to the -CH_2 of the ester group. The solvent peak (dmso) and moisture (H_2O) peaks are very conspicuous at 2.50 ppm and 3.40 ppm respectively. A peak observed at δ 7.45 ppm can be assigned to the NH protos of the thiourea group. The ^{13}C-NMR spectra of the complex show signals for C-S (206.20), C=O (163.90), C≡N (120.74), C=O (90.88), -OCH_2 (59.32) and CH_3 (δ 14.54 ppm) for the carbons of ecda^{2-} and methylthiourea group.

4.3.3 NMR spectra of [Cd(mtu)$_2$ecda]

The ^{1}H-NMR of this compound is devoid of singlet peak expected of the -CH_3 attached to the azo-nitrogen group. The spectrum only shows the -OCH_2 (quartet peak at approximately δ 3.98 ppm) and a triplet at δ 1.15 ppm) for -CH_3 of the OCH_2CH_3 group.

The ^{13}C-NMR spectra of this show signals for C-S (208.57), C=O (164.70), C≡N (121.64), C=O (90.26), -OCH_2 (58.26) and CH_3 (δ 14.58 ppm) for the carbons of ecda^{2-} and methylthiourea ligands.

4.3.4 NMR spectra of [Hg(mtu)$_2$ecda]

The ^{1}H-NMR spectra of the mercury complex exhibit very weak signal because of it is springly soluble in DMSO. A peak observed at δ 1.27 ppm can be assigned to the methyl group attached to the CH_2 hydrogen atoms of the ester group in the ecda^{2-}. Another peak observed at δ 3.78 can be assigned to the methyl hydrogen atoms of the methylthiourea. Attempts to run the solid state ^{13}C-NMR was not successful because the instrument could not be caliberated.

4.4 Metal complexes of dimethylthiourea (dmtu)$_2$ and 1-ethoxylcarbonyl-1-cyanoethylene-2,2-dithiolate: [M(dmtu)$_2$ecda].

Zn(II), Cd(II) and Hg(II) complexes of dimethylthiourea (dmtu) and ecda have been synthesized by the reaction between the metal salts and the ligands in methanol. The complexes are air stable and formulated as [M(dmtu)$_2$ecda] based on the analytical and spectroscopic data. The formation of the compound can be represented as shown in Scheme 4.2.

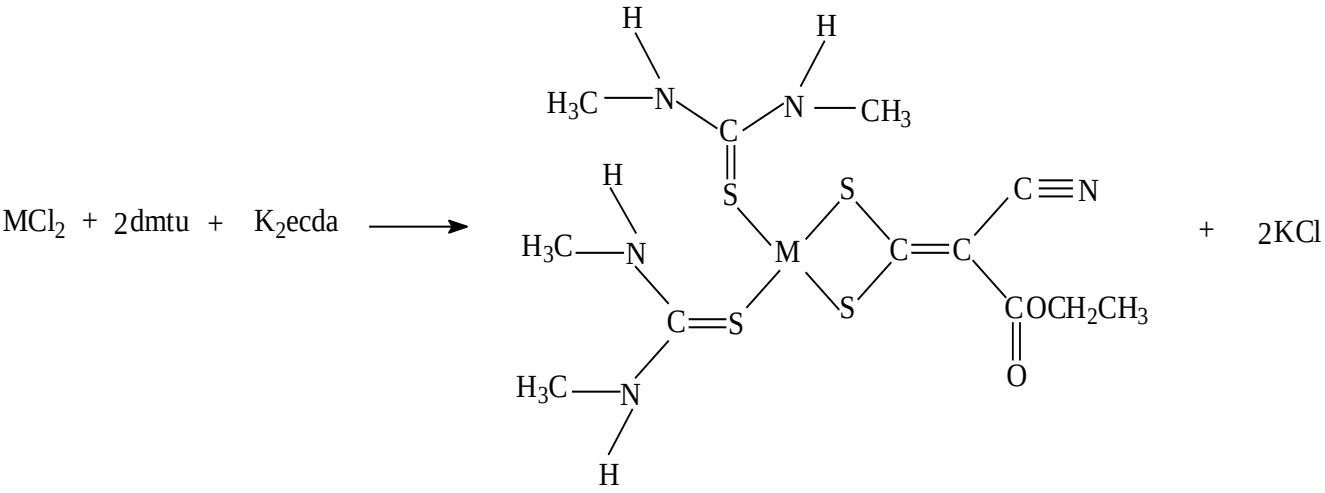

Scheme 4.2: Synthesis of metal complexes of dmtu and ecda.

The complexes are stable and decompose at temperature range 150-240 ºC and insoluble in most common solvents. They were characterized by elemental analysis, IR and NMR spectroscopic techniques.

4.4.1 Infrared spectra studies of [M(dmtu)$_2$ecda]

The IR spectra of these complexes show several absorption bands similar to the ones that were discussed previously. Relevant IR spectra for the ligands and the complexes were presented in Table 4.3. The N-H stretching vibrations that occur at 3233 cm^{-1} in the dimethylthiourea shifted to about 3244 in the complexes. The shift might be due to hydrogen bonding in the complexes. Four main regions are of interest in 1-ethoxylcarbonyl-1-cyanoethylene-2,2-dithiolate complexes are: the 2188-2244 cm^{-1} due to ν(C≡N); 1645-1700 cm^{-1} due to ν(C=O); 1412-1492 cm^{-1} due ν(C=CS$_2$) and 1116-1165 cm^{-1} due to ν(C-S) of the chelated ecda^{2-} [9]. In the metal complexes, these stretching vibrations were observed at 2209, 1705, 1448 and 1188 cm^{-1} for [Zn(dmtu)$_2$ecda]; 2209, 1629, 1473 and 1165 cm^{-1} for [Cd(dmtu)$_2$ecda] and 2241, 1649, 1459, 1191 cm^{-1} for [Hg(dmtu)$_2$ecda]. The stretching vibrations that appear at 720 cm^{-1} in the free dimethylthiourea shifted to about 670 cm^{-1} in the metal complexes. The red shifting of the ν(C=S) bond of the free ligand confirm that methylthioures is coordinated to the metal ions via the sulfur with a reduction of π-electron density of the ν(C=S) bond [10, 11]. The complexes show medium to weak ν(M-S) bands between 424 and 377 cm^{-1}. The ν(M-S) was observed at 376, 396 and 388 in [Zn(dmtu)$_2$ecda], [Cd(dmtu)$_2$ecda] and [Hg(detu)$_2$ecda] respectively. The presence of bands confirms the coordination of the ions to the sulfur atoms [10, 11].

Table 4.3: Relevant IR spectra of [M(dmtu)$_2$ecda]

	v(N–H)	*v*(C≡N)	*v*(C=O)	*v*(C=S$_2$)	*v*(C–S)	*v*(C=S)	*v*(M–S)
[Zn(dmtu)$_2$ecda]	-	2209	1705	1448	1188	671	394
[Cd(dmtu)$_2$ecda]	3244	2209	1629	1473	1165	670	377
[Hg(dmtu)$_2$ecda]	3362	2241/ 2202	1599/ 1649	1459/ 1457	1191/ 1156	670	424/ 378

4.4.2 NMR spectra of [Zn(dmtu)$_2$ecda]

The singlet peak at δ 7.37 ppm in the ^{1}H-NMR can be assigned to the proton of the NH of the thiourea group. Other peaks at δ 3.98, 1.15, and 1.04 ppm are due to protons of (OCH_2), (CH_3) and for (NH)-CH_3) respectively. Other prominent peaks are for at 2.5 and 3.5 ppm are due to solvent (dmso) and moisture (H_2O). The ^{13}C NMR spectra of [Cd(dmtu)$_2$ecda] shows resonance signals corresponding to ecda for; C-S (206.24), C=O (163.85), C≡N (120.79), C=O (90.83), -OCH_2 (58.31) and CH_3 (δ 14.54 ppm) for the carbons of ecda and thiourea group. A marginal coordination induced downfield shift of the C-S carbon is indicative of the (S, S) coordinated nature of the ecda^{2-} [1].

4.4.3 NMR spectra of [Cd(dmtu)$_2$ecda]

A peak observed at δ 7.34 ppm can be assigned to the NH protons of the thiourea group.The

peaks at δ 3.99, and 1.15 ppm in the ^{1}H-NMR of the complex can be assigned to the protons of OCH_2 and CH_3 respectively. The singlet peak at δ 2.79 ppm maybe assigned to the CH_3-$(NH)_2$. The ^{13}C NMR of this compound, [Cd(dmtu)$_2$ecda], shows a peak at δ 207.79 ppm, characteristic of a C-S functionality. The peak at δ 165.49 and 121.40 can be assigned to the carbon atoms of (C=O) and (C=N), respectively. The peak at 90.44 ppm may be assigned to -C=C attached to the CN (triple bond). The -OCH_2 is assigned to peak at δ 58.63 ppm and at 14.54 ppm show the presence of -CH_3.

4.4.4 NMR spectra of [Hg(dmtu)$_2$ecda]

There is conspicuous absence of a triplet and quartet peaks in the ^{1}H-NMR which could be assigned -CH_3 and -OCH_2 protons of the ecda^{2-}, this compound due to poor solubility of the compound.

4.5 Metal complex of diethylthiourea (detu)$_2$ and 1-ethoxylcarbonyl-1-cyanoethylene-2,2-dithiolate (ecda)

These complexes are formulated as [M(detu)$_2$ecda] (where M = Zn, Cd and Hg). The synthetic method used in the preparation is the same as in the previous complexes. The complexes were characterized with elemental analysis, IR, ^{1}H- and ^{13}C-NMR spectroscopy. The substituted thiourea in this complex is the diethylthiourea which is a monodentate ligand and the second ligand, 1-ethoxylcarbonyl-1-ethylene-2,2-dithiolate, is a bidentate chelating ligand. The mode of coordination to the central metal is through four sulfur atoms. The complexes are formulated as

four coordinate species consisting of two molecules of monodentate diethythiourea and one molecule of bidentate ecda. Substituted thiourea compounds are known to form stable complexes and have been reportedly used as single source precursors for the preparation of semiconductor nanoparticles [12, 13]. Formation of the complexes can be represented as shown in Scheme 4.3. All the three complexes are not soluble in the common organic solvents although they are sparingly soluble in DMF, DMSO, and acetonitrile. They also decompose in the temperature range of 200-400 ^{o}C.

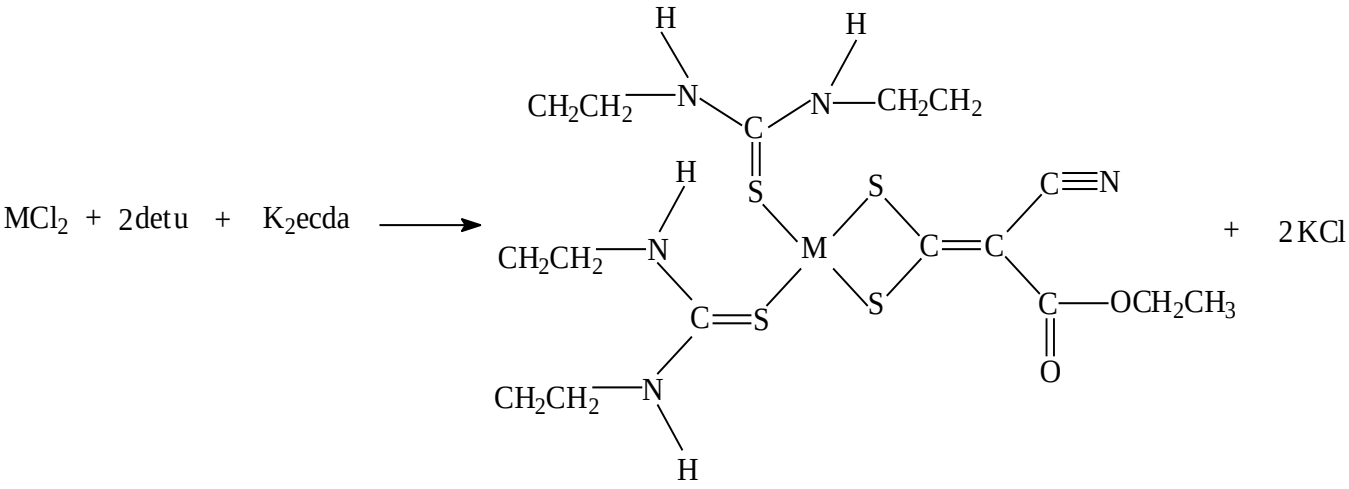

Scheme 4.3: Synthesis of [M(detu)$_2$(ecda)], M= (Zn, Cd and Hg)

4.5.1 Infrared spectra studies of [M(detu)$_2$ecda].

In order to clarify the mode of bonding and the effect of the coordination of the metal ions on the ligands, the IR spectra of the free ligands and their respective metal complexes were assigned on careful comparison. Relevant IR spectra for the ligands and the complexes are compiled in Table 4.4. The N-H stretching vibrations that occur at 3219 cm^{-1} in the diethylthiourea shifted to about

3275 cm^{-1} in the complexes. The shift might be due to hydrogen bonding in the complexes. The most important vibrational modes of the 1-ethoxylcarbonyl-1-cyanoethylene-2,2-dithiolate ligands are ; 2161 cm^{-1} due to ν(C≡N); 1681 cm^{-1} due to ν(C=O); 1360 cm^{-1} due ν(C=CS_2) and 1160 cm^{-1} due to ν(C-S). The assingnment of these vibrations frequencies are based on literature source [1, 2, 9]. These were observed in the metal complexes at 2200, 1681, 1462 and 1193 cm^{-1} for [Zn(detu)$_2$ecda] ; 2206, 1651, 1463 and 1176 cm^{-1} for [Cd(detu)$_2$ecda] and 2188, 1656 , 1458, 1191 cm^{-1} for [Hg(detu)$_2$ecda] characteristic of ecda complexes in a chealating and bidentate bridging mode [14]. The stretching vibrations that appear at 794 cm^{-1} in the free diethylthiourea shifted to about 670 cm^{-1} in the metal complexes. The red shifting of the ν(C=S) bond of the free ligand confirm that diethylthiourea is coordinated to the metal ions via the sulfur with a reduction of π-electron density of the ν(C=S) bond [9, 10].

Table 4.4: Relevant IR spectra of [M(detu)$_2$ecda]

Complexes	ν(N–H)	ν(C≡N)	ν(C=O)	ν(C=S_2)	ν(C–S)	ν(C=S)	ν(M–S)
[Zn(detu)$_2$ecda]	-	2200	1681	1462	1193	670	373
[Cd(detu)$_2$ecda]	3275	2206	1651	1463	1176	666	372
[Hg(detu)$_2$ecda]	3362	2188	1656	1458	1191	669	375

The complexes show medium to weak ν(M-S) bands between 420 and 250cm^{-1}. The ν(M-S) was observed at 373, 372 and 375 in [Zn(detu)$_2$ecda], [Cd(detu)$_2$ecda] and [Hg(detu)$_2$ecda] respectively. The presence of bands confirms the coordination of the ions to the sulfur atoms [9,

10].

4.5.2 NMR spectra of [Zn(detu)$_2$ecda]

The ^{1}H-NMR of [Zn(detu)$_2$ecda] show sharp well resolved signals at δ 7.29 which can be assigned to the NH proton the thiourea group. The peak at δ 2.78 can be assigned to CH_3-$(NH)_2$. The quartet at δ 3.97 ppm can be assigned to OCH_2 and peak at δ 1.16 can be ascribed to CH_3 of the ester group. The ^{13}C NMR spectra of this metal complex show peaks at C-S (206.23), C=O (163.87), C≡N (120.76), C=O (90.84), -OCH_2 (58.32) and CH_3 (δ 14.53 ppm) of the ecda^{2-} carbon group.

4.5.3 NMR spectra of [Cd(detu)$_2$ecda]

The ^{1}H-NMR show two triplet peaks at δ 1.16 and 1.05 ppm which were assigned to the CH_3 groups. There is also a quartet peak at δ 3.99 ppm which is due to the CH_2 of the OCH_2 of the ecda^{2-} group. The ^{13}C-NMR spectra of this complex, [Cd(detu)$_2$ecda], show signals for C-S (208.15), C=O (163.85), C≡N (121.57), C=O (90.25), -OCH_2 (58.49) and CH_3 (δ 14.57 ppm) for the carbons of ecda^{-2} and thiourea group. The downfield shift observed for the protons compared to K_2ecda clearly indicates the de-shileding of the ethoxyl protons in this complex.

4.5.4 NMR spectra of [(Hg(detu)$_2$ecda]

The ^{1}H-NMR of this complex is difficult to assign due to poor solubility.

4.6 Metal complexes of tetramethylthiuram disulfide (tmtd) and 1-ethoxylcarbonyl-1-cyanoethylene-2,2-dithiolate (ecda), [M(tmtd)ecda]

The complexes were formed by the reaction between the metal salts and the ligands. The four coordinate geometries around the metal ions consist of one molecule of tetramethylthiuram disulfide and one molecule of ecda ligand. The general reaction equation is shown below.

MCl_2 + 2tmtd + K_2ecda ⟶

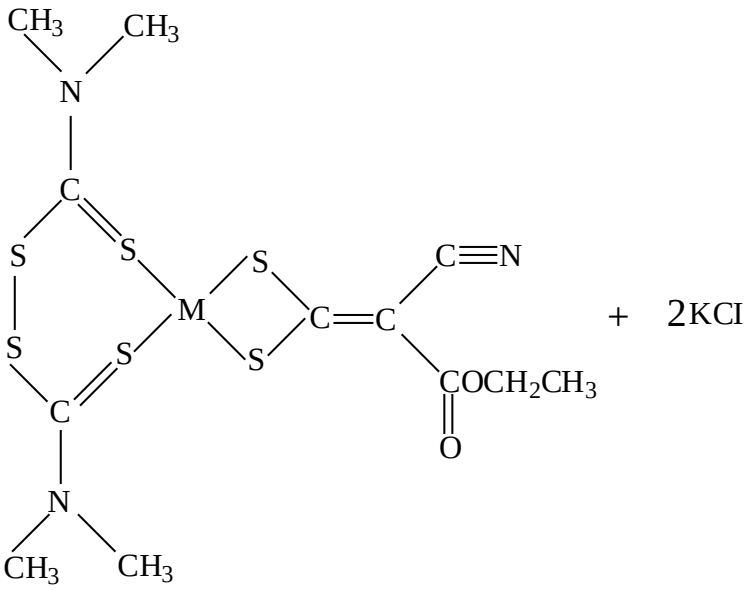

Scheme 4.4: Synthesis of [M(tmtd)(ecda)], M = Zn, Cd, Hg.

4.6.1 Infrared spectra studies of [M(tmtd)ecda]

The IR of the metal complexes synthesised from ecda and tetramethylthiuram disulfide exhibit characteristic changes in the functional group when compared with the spectra of the ligands. Relevant IR bands for [M(tmtd)ecda] the complexes are presented in Table 4.5.The ecda has four important absorptions frequencies which are; 2161 cm^{-1} due to ν(C≡N); 1681 cm^{-1} due to

v(C=O); 1360 cm^{-1} due *v*($C=CS_2$) and 1160 cm^{-1} due to *v*(C-S) [15]. These stretching vibrations were observed in the metal complexes at; 2245, 1732, 1438 and 1142 cm^{-1} for [Zn(tmtd)ecda] ; 2233, 1600, 1512 and 1147 cm^{-1} for [Cd(tmtd)ecda] and 2244 , 1738 , 1492, 1191 cm^{-1} for [Hg(tmtd)ecda] respectively. There are four vital bands of thiuram disulfide in the metal complexes and they appear in the region of 800-1510 cm^{-1}; (i) there is strong thioureide C-N band, (ii) the band at 1200 cm^{-1} which is due to C-N vibration of the alkyl group, (iii) the band responsible for the C=S stretching mode around 973 cm^{-1} and (iv) the band around 822 cm^{-1} that can be assigned to the stretching C-S mode.

Table 4.5: Relevant IR spectra of [M(tmtd)ecda]

	v(C≡N)	*v*(C=O)	*v*($C=S_2$)	*v*(C–S)	*v*(C=S)	*v*(M–S)
[Zn(tmtd)ecda]	2245	1732	1138	1142	970	382
[$Cd(tmtd)_2$ecda]	2233	1600	1512	1147	957	384
[$Hg(tmtd)_2$ecda]	2244	1738	1492	1170	-	449

All these band are observable in the following complexes, [Zn(tmtd)(ecda)], [Cd(tmtd)(ecda)] and [Hg(tmtd)(ecda)] at vibration frequencies of ; (i)1520 cm^{-1}, 1512 cm^{-1} , 1530 cm^{-} (ii) 1200 cm^{-1}, 1209 cm^{-1}, 1201 cm^{-1} (iii) 973 cm^{-1}, 957cm^{-1} , 965 cm^{-1} and (iv) 822 cm^{-1} , 820 cm^{-1}, 830 cm^{-1} respectively. The absorption bands assigned to M-S in these complexes are observed at 384cm^{-1}, 449 cm^{-1} and 416 cm^{-1} for [Zn(tmtd)(ecda)], [Cd(tmtd)(ecda)] and [Hg(tmtd)(ecda)] respectively.

4.6.2 NMR spectra of [Zn(tmtd)ecda]

The ^{1}H NMR of this complex show a triplet at δ 1.05 and a quartet at δ 4.02 ppm which can be assigned to CH_3 and OCH_2 of the $ecda^{2-}$. The ^{13}C-NMR spectrum of this complex, [Zn(tmtd)ecda], show peaks around δ 203.69, 168.68, 122.94, 59.29, and 18.51 ppm corresponding to C-S, C=O, C≡N, -OCH_2, and CH_3 respectively for carbon of the $ecda^{2-}$.

4.6.3 NMR spectra of [Cd(tmtd)ecda]

The ^{1}H-NMR spectra of the above named complex yield a triplet at δ 1.27 for the -CH_3 protons of the tetramethylthiuram disulfide (tmtd) and the ester group of the ecda ligand which is mixed together. The protons of the -OCH_2 group are observed as a quartet at 1.27- 4.09 ppm.

4.6.4 NMR spectra of [Hg(tmtd)ecda]

The ^{1}NMR spectra of this complex, [Hg(tmtd)ecda], show triplet peaks at δ 1.05 and 4.35 for –CH_3 protons of the tetramethylthiuram disulfide and $ecda^{2-}$ The other peaks at δ 2.5 and 3.4 are due to solvent peaks of dmso and water. The complex is partially soluble in dmso and hence the spectrum was very weak. The complex was run for solid state NMR on 600 MHz machine but the complex could not be used for calibration and all effort to do it proved abortive. As a result of this, the ^{13}C-NMR was not reported.

4.7 Thermal studies of selected metal complexes

In order to be able to use metal chalcogenide as single source precursors [16, 17], it is necessary to carry out thermogravimetry analysis (TGA) of the complexes. Thermal analysis of metal complexes using TGA is a characteristic technique that measures the mass change of a substance as a function of temperature while the substance is subjected to control heating [18]. The technique is very important because it allows the evaluation of the injection temperature which is primarily decided by the decomposition temperature of the precursors since injection of the precursor is usually done at a temperature below the decomposition point of the precursor. The TGA therefore serves as a guide in deciding the temperature at which the precursors should be dispersed into the hot coordinating solvents. The second important reason is that it is a means of verifying the final decomposition products for the metal complexes and their usefulness as single molecule precursors. A two-step decomposition profile has been proposed by Jona *et al.* [19] for thiourea metal complexes based on thermogravimetry analysis. The study concluded that ammonia thiocyanate and guanidine thiocyanate were intermediate and thiocyante was the residue.

In other studies, thermal decompsition of copper, zinc, cadmium and tin metal complexes of alkylthiourea in static air led to the formation of metal sulfide as a main decomposition product between 200-300 ºC. Four different thiourea metal complexes were comparatively studied simultaneously in thermoanalytical apparatus and it was observed that the main degradation step lead to the formation of digenite, zinc blende and berndite which are respective metal sulfides of

Cu, Zn and Sn [20]. Baily and Tangredi [21] investigated the thermal decomposition of methyl and dimethyl thiourea complexes of many transition metal complexes with thiourea and urea. The dimethyl thiourea complex decomposed to give a mixture of metal chloride and metal sulfide. Merdivan *et al*.[22] studied several metal complexes of thiourea and suggested two step decomposition process for compounds of N,N-dialkyl-N'-benzoylthiourea with Cu(II), Ni(II), Pd(II), Pt(II), Cd(II), Ru(III) and Fe(III). The metal complexes decomposed with elimination of diaklylbenzamide and total decomposition to metal sulfide. The thermal properties of the metal complexes were studied by TGA in the temperature ranging from 20 to 800 ºC under nitrogen atmosphere. The changes in the composition and the structure of a particular complex can be determined using the percentage mass loss in the thermogravimetry plot of the complex. The themal decomposition data for eight of the twelve complexes synthesized are presented in Table 4.6.

Table 4.6: Percentage weight loss of thermal decomposition of the mixed ligand complexes give corresponding metal sulfide (MS).

Compounds	Decomposition Ranges (°C)	Peak temperature(°C)	Expected Products	Percentage Weight loss (%) Found (Calc.)
[Zn(dmtu)$_2$ecda]	194-293	231	ZnS	54.03 (58.05)
[Cd(dmtu)$_2$ecda]	222-334	248	CdS	66.93 (66.78)
[Cd(mtu)$_2$ecda]	247-319	273	CdS	65.07 (65.15)
[Hg(detu)$_2$ecda]	278-460	423	volatilize	99.20 (100)
[Hg(dmtu)$_2$ecda]	291-467	441	volatilize	98.76 (100)
[Zn(tmtd)ecda]	229 - 378	346	ZnS	47.78 (47.73)
[Cd(tmtd)ecda]	264-420	384	CdS	43.72 (43.10)
[Hg(tmtd)ecda]	329-471	447	volatilize	99.40 (100

4.7.1 Thermal analysis of [Cd(dmtu)$_2$ecda]

The TG and DTG of this complex, [Cd(dmtu)$_2$ecda], is presented in Figure 4.4. It showed that compound start decomposing at about 222 ºC and this decomposition continued till about 335 ºC. The decomposition is associated with percentage loss of the organic part of the complex. At the temperature range of 250-320 ºC, about 66% of weight loss occurred and this correspond to the decomposition of the organic moeity of the complex leaving behind the metal sulfide [23]. The peak temperature point was 248 ºC. The percentage weight loss is close to the expected stoichiometry formation of metal sulfide: Found (calc.) (%), 66.93 (67.78).

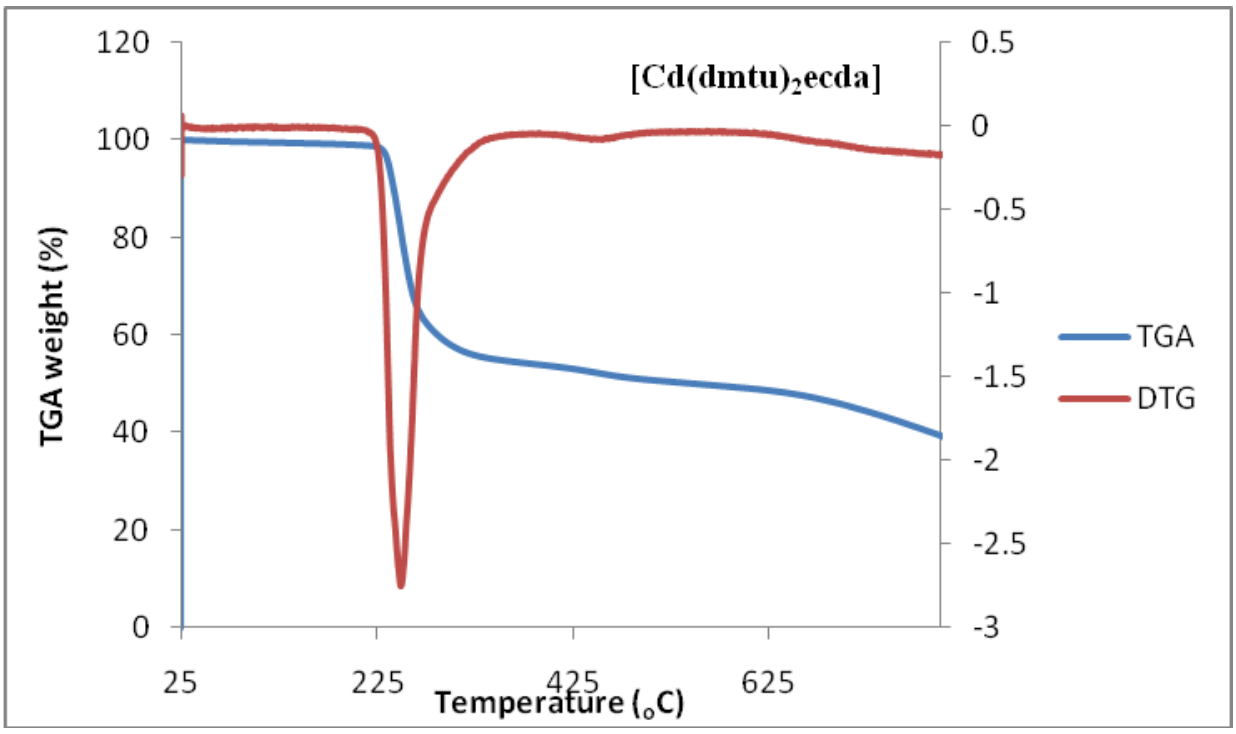

Figure 4.4: Superimposed TG/TGA of [Cd(dmtu)$_2$ecda].

4.7.2 Thermal analysis of [Cd(mtu)$_2$ecda]

The TG and DTG of this complex, [Cd(mtu)ecda], are shown in Figure 4.5. It showed that decomposition in this complex started around 247 ºC and terminated around 319 ºC The peak decomposition temperature was at 273 ºC after which the weight loss was about 65.00 % which was due to loss of the organic part of the metal complex. The percentage weight loss in this complex, [Cd(mtu)$_2$ecda], are close to values expected for stoichiometry formation of CdS; Found (Cal) % 65.07 (65.15).

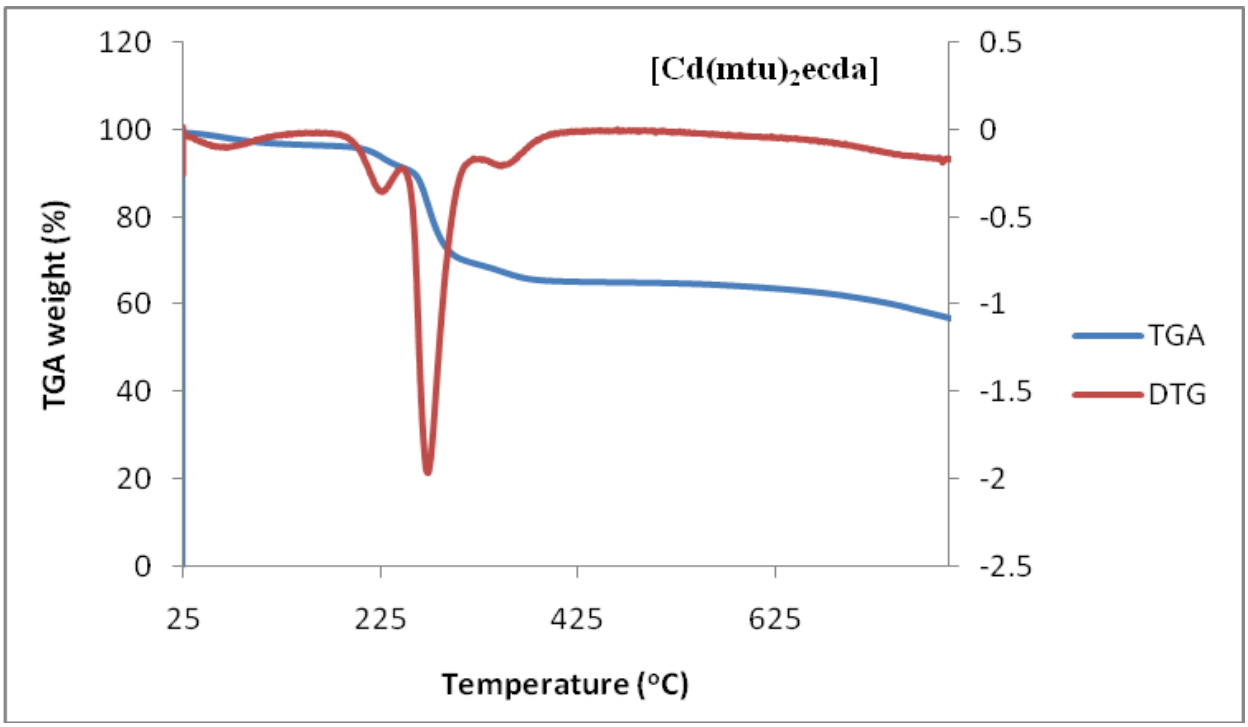

Figure 4.5: Superimposed TG/TGA of [Cd(mtu)$_2$ecda]

4.7.3 Thermal analysis of [Hg(dmtu)$_2$ecda]

The TG and DTG of [Hg(dmtu)$_2$ecda] is shown in Figure 4.6. This complex undergo a one-step decomposition between 291 and 467 ºC with about 98% weight loss. The peak temperature is 441ºC. The non availability of residue in the pan after thermal analysis showed the decomposition process was a one step volatisation giving Hg and S. Some chalcogenides of zinc and cadmium complexes undergo decomposition first to their metal sulfides and which gets oxidised to metal oxides at elevated temperatures unlike some mercury chalcogenides that volatilizes to give unstable gaseous products at temperature above 600 ºC [24]. The calculated weight loss of 98% differ slightly from the found value of 100%. The difference might be due to the volatilisation of the decomposition product.

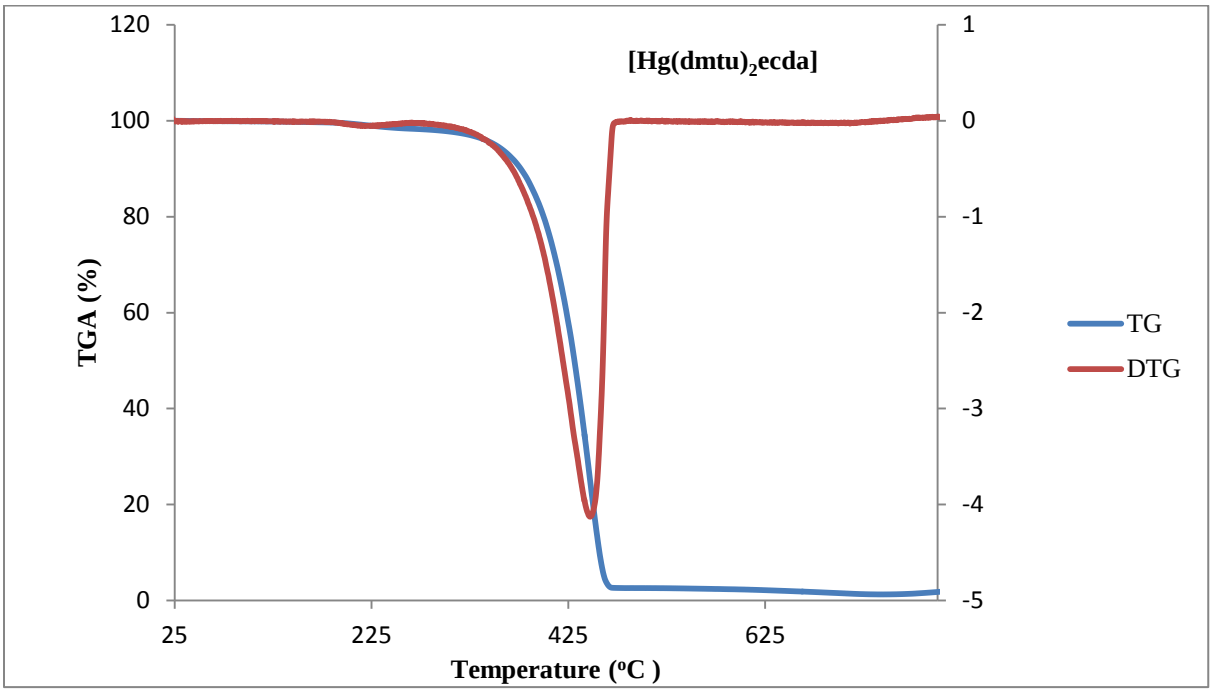

Figure 4.6: Superimposed TG/TGA of [Hg(dmtu)$_2$ecda]

4.7.4 Thermal analysis of [Hg(detu)$_2$ecda]

The TG and DTG of [Hg(detu)$_2$ecda] is presented in Fig 4.7. Three different temperatures were indentified in the thermogram. The decomposition of the complex started at about 278 ºC , the peak decomposition temperature is around 423 ºC and the thermal decomposition terminated at 460 ºC. At this temperature the complex undergoes volatalization to give Hg and S [24]. There was over 99% weight lost which was as a result of not only the loss of the organic part of molecule but also the volatilization of unstable HgS. At higher temperature HgS decomposes to Hg and S as indicated in the reaction below.

$$[Hg(detu)_2ecda]_{(s)} \xrightarrow{\triangle} HgS_{(s)} \qquad 1$$

$$HgS_{(s)} \xrightarrow{\triangle} Hg_{(g)} + \tfrac{1}{2}S_2(g) \qquad 2$$

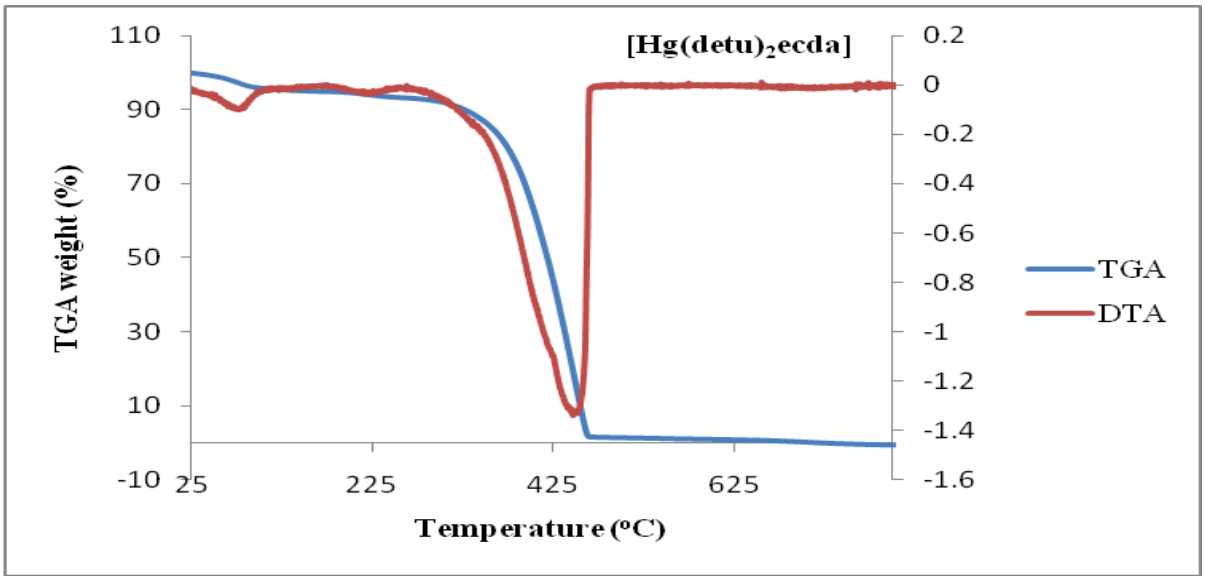

Figure 4.7: Superimposed TG/TGA of [Hg(detu)$_2$ecda]

4.7.5 Thermal analysis of [Zn(dmtu)2ecda]

The TG and DTG of [Zn(dmtu)$_2$ecda], is presented in Figure 4.8. In the complex, there was a loss of weight that might be due to entrapped water molecule at 100 ºC and the onset temperatue of decomposition was at 194 ºC. The decomposition continues till 293 ºC with a 58% weight loss to give ZnS. The reduction in percentage weight of the sample can be ascribed to the loss of the organic moeity to give grey ash residue of ZnS in the pan. The peak decomposition temperature was at 231 ºC. The weight loss of 54.03% in this complex is close to the expected value 54.03% for stoichiometry formation of ZnS: Found (Calc.) %, 54.03 (58.05). Hence the metal complex is suitable as a precursor for the synthesis of metal sulfide nanoparticles. The difference in the calculated and the experimental value is most probably due to the entrapped solvent molecule in the complex.

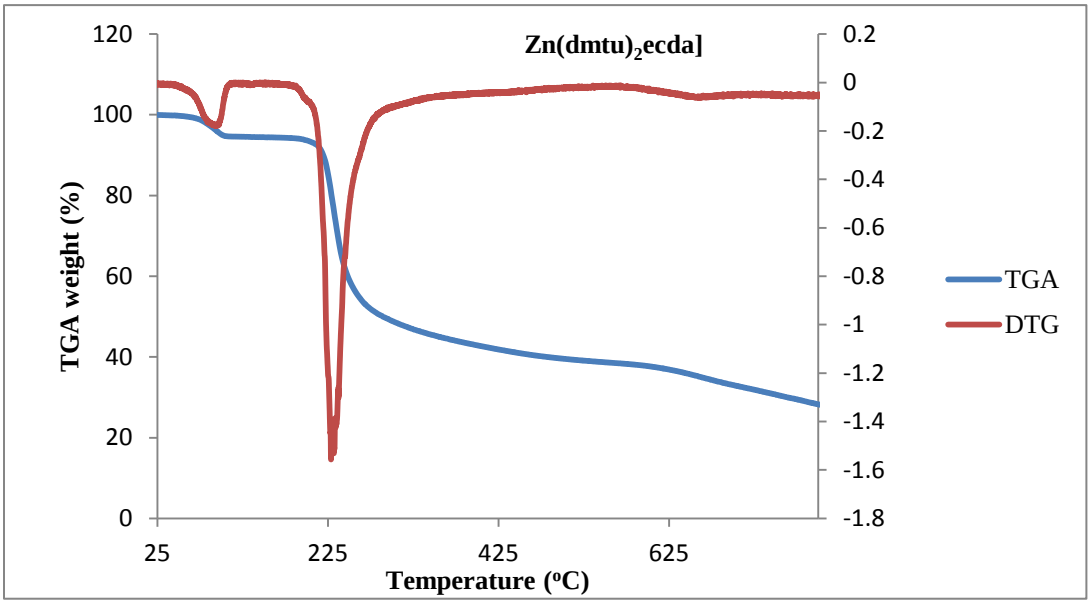

Figure 4.8: Superimposed TG/TGA of [Zn(dmtu)$_2$ecda]

4.7.6 Thermal analysis of [Hg(tmtd)ecda]

The TG and DTG of this complex, [Hg(tmtd)ecda], are presented in Figure 4.9. It is observed from the thermogram that the Hg complex has higher decomposition temperature than Zn and Cd complexes from the same ligands. The onset decomposition temperature of this complex is 329 ºC and the decomposion continued till 471 ºC with a huge loss of weight to give Hg and S. This has earlier been discussed for mercury complexes [24]. Peak temperature recorded here was 447 ºC and the actual percentage weight loss is 99.40% as shown in the thermogram below. It can be deduced in this case that the percentage weight loss vary slightly from the calculated value. The HgS volatalises giving gaseous products.

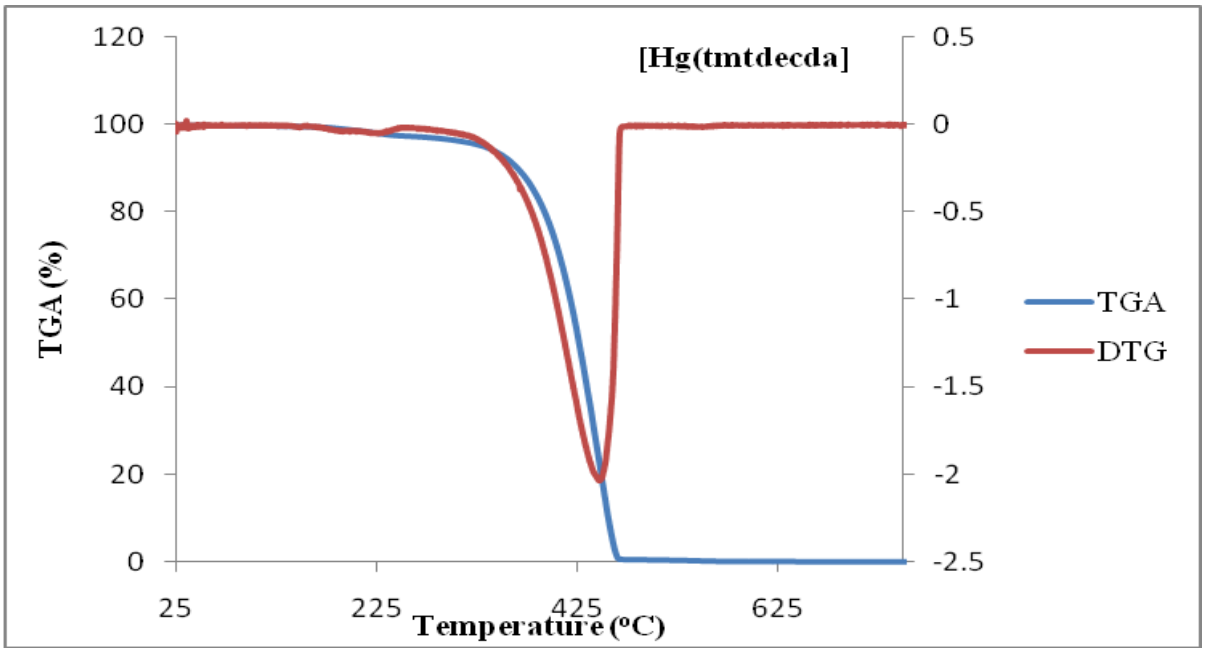

Figure 4.9: Superimposed TG/TGA of [Hg(tmtd)ecda]

4.7.7 Thermal analysis of [Zn(tmtd)ecda]

The TG and DTG of [Zn(tmtd)ecda] is presented in Figure 4.10 and the onset decomposition is at 229 ºC. The peak temperature is 346 °C at which point there was about 47% weight loss to give ZnS. The weight loss is due to the elimination of the organic moeity from the metal complex. The decomposition continued till 378 ºC. The percentage weight loss in this complex, 47.78%, agree with the calculated value of, 47.73% . The values are close to a great extent and it confirms that ZnS is the fnal product of the TGA analysis.

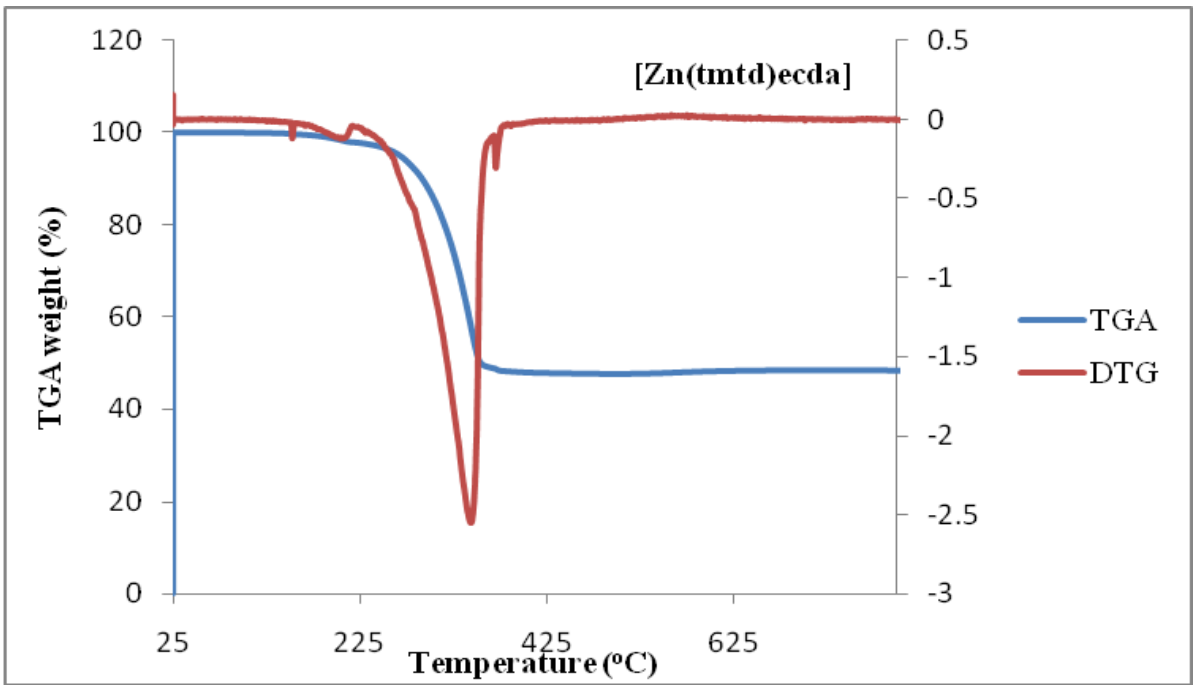

Figure 4.10: Superimposed TG/TGA of [Zn(tmtd)ecda]

4.7.8 Thermal analysis of [Cd(tmtd)ecda]

The TG and DTG are presented in Figure 4.11 for the complex, [Cd(tmtd)ecda], and three main temperatures were identified from the decomposition pathway of this thermogram. There was loss of a fragment at 200 ºC, the onset decomposition temperature at 264 ºC and the peak decomposition temperature at 384 ºC. The decomposition of this complex exhibited about 43.72% weight loss corresponding to the loss of the organic moeity in the complex. The TG curve showed plateau from 410 ºC to the end of thermal analysis leading to the formation of CdS. The calculated weight loss of the organic part of the complex was 43.10% and the experimental one was 43.72% and this is close to the stoichiometry formation of CdS.

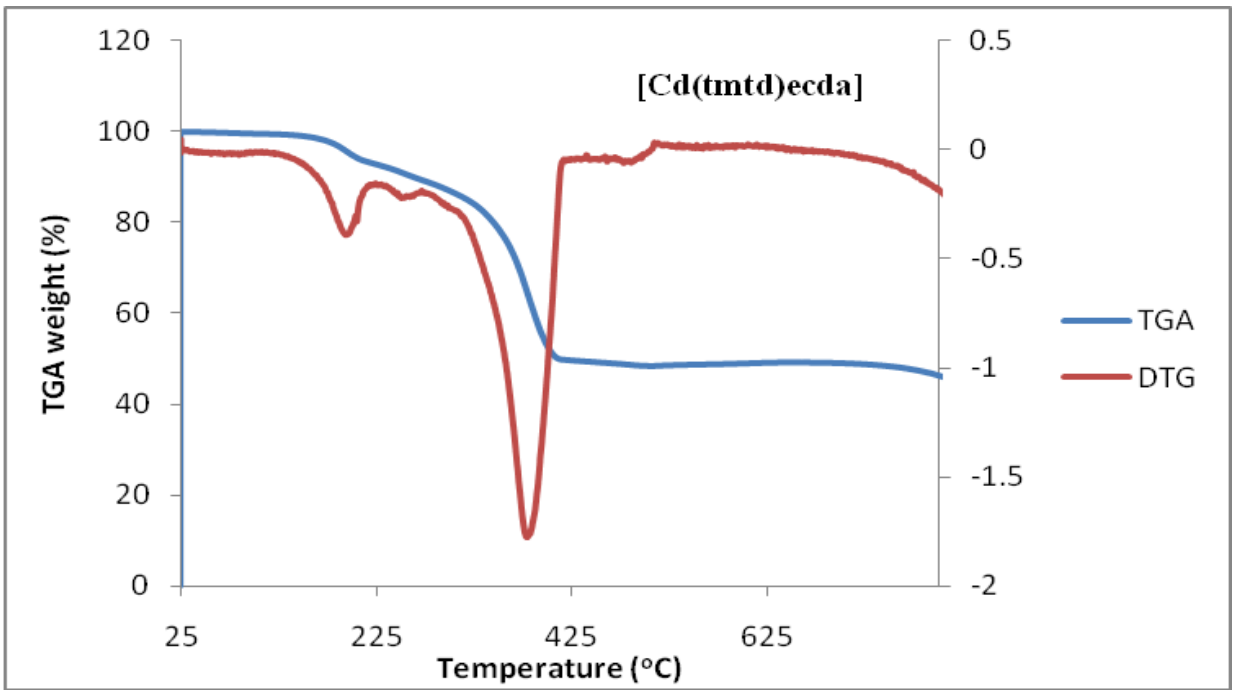

Figure 4.11: Superimposed TG/TGA of [Cd(tmtd)ecda]

References

1. Singh, N.; Gupta, S. Magnetic and electrical properties of new inorganic complex based materials derived from bis(1-ethoxycarbonyl-1-cyanoethylene-2,2-dithiolato)metalate(II) ions. *Int. J. Inorg. Mater*. **2000**, 2, 427-435.

2. Singh, N.; Gupta, S. Solid state electrical conductance properties of some newbimetallicoordination polymers derieved from bis (1-ethoxylcarbonyl-1-cyanoethylene- 2, 2-dithiolato) cuprate(II) ion. *Synth. Met*. **1999**, 107, 167-174.

3. Liu, C.W.; Liaw, B-J.; Wang, J-C.; Tai-Chiun, K. Solid state structures of $Ag_5(dppm)_4(S_2CC(CN)P(O)(OEt)_2)_2][PF_6]$ and $Ag_4(dppm)_4(S_2CC(CN)P(O)(OEt)_2)_2$: variable coordination modes of 1,1-dithiolate to silver(I). *Inorg. Chem*. **2000**, 39, 1329-1332.

4. Sarkar, B.; Llaw, B.; Fang, C.; Liu, C.W. Phosphonate and ester substituted 2 cyanoethylene-1,1-dithiolate cluster of Zinc; Aerial CO_2 fixation and unusual binding pattern. *Inorg. Chem*. **2008**, 27, 277-2785.

5. Liu, C.W.; Liaw, B-J.; Wang, J-C.; Liou, L-S.; Keng, T-C. Dithiolate clusters of copper(I): utilization of all possible coordination sites of 1-(diethoxyphosphinyl)-1-cyanoethylene-2,2-dithiolate. *J. Chem. Soc., Dalton Trans*. **2002**, 1058-1065.

6. Singh, N., Kumar, S.R. Organoheterobimetallic complexes derived from bis(1-thoxycarbonyl)-1-cyanoethylene-2, 2-dithiolatometalate(II) ion: synthesis and properties. *J. Organomet. Chem*. **2000**, 605, 102-108.

7. Singh, M.K.; Paul, A.D. Synthesis and structural characterization of mixed ligand complexes of nickel(II) with 1,1-dicyanoethylene-2,2-dithiolate and some nitrogen donors. Transition Metal Chemistry, **2005**, 30, 655-660.

8. Pearson, R.G. Hard and soft acid and bases. *J. Am.Chem.Soc*. **1963**, 85, 3533-3547.

9. Cummings, S. D., Eisenberg, R. Luminescent platinum II bis(1,1-dithiolate) complexes. *Inorg.* Chim. *Acta* **1996**, 242, 225-231.

10. Yan, Z.; Voloshin, Y.Z.; Varzatskii, O.A.; Kochubey, D.I.; Vorontsov, I. I.; Yurii, N.; Bubnov, Y.N. Synthesis and structure of monoribbed-functionalized disulfide iron(II) clathrochelates and their coordination as the ligands toward platinum(II) and platinum(IV) ions. *Inorg*. *Chim*. *Acta* **2009**, 362, 149-158.

11. Altaf, M.; Stoeckli-Evans, H.; Batool, S.S.; Isab, A.A.; Ahmad, S.; Saleem, M.; Awan, A.S. Shaheen, M.A. Mercury(II) complexes of pyrrolidinedithiocarbamate, crystal structure of bis{[μ2-(pyrrolidinedithiocarbamato-*S, S ′*) (pyrrolidinedithiocarbamato-*S, S*′)mercury(II)]}. *J*. *Coord*. *Chem*. **2010**, 63, 1176-1185.

12. Moloto, N.; Revaprasadu, N.; Moloto, M.J. O' Brien, P.; Raftery, J. N,N'-diisopropylthiourea and N, N'-dicyclohexylthiourea zinc(II) complexes as precursors for the synthesis of ZnS nanoparticles. *S. Afri. J. Sci*. **2009**, 105, 7-8.

13. Moloto, M.J.; Malik, M.A.; O'Brien P.; Motevalli, M.; Kolawole, G.A. Synthesis and characterization of some *N*-alkyl/aryl and *N, N*′-dialkyl/aryl thiourea cadmium(II) complexes: the single crystal X-ray structures of $[CdCl_2(CS(NH_2)NHCH_3)_2]_n$ and $[CdCl_2(CS(NH_2)NHCH_2CH_3)]$. *Polyhedron*, **2003**, 22, 595-603.

14. Cummings, S.D.; Eisenberg, R. Tuning the excited-state properties of mixed-ligand platinum(II) diimine dithiolate complexes. *J. Am*. *Chem*. *Soc*. **1996**, 118, 1949-1960.

15. Victoriano, L.I.; Gnecco J.A.; Carbacho, H.V Oxidation of tetramethylthiuram sulphide (II

dithiocarbamate with ferric chloride). *Polyhedron*, 1996, 15, 1315-1321.

16. Trindade, T.; O'Brien, P. A single source approach to the synthesis of CdSe nanocrystallites. *Adv. Mater*. **1996**, 8, 161-163.

17. Trindade, T.; O'Brien. P. Synthesis of CdS and CdSe nanocrystallite using novel single source molecule precursor approach. *Chem. Mater*. **1997**, 9, 523-530.

18. Haines, P.J. Principle of thermal analysis and calorimetry. *The Royal Society of Chemistry*. Great Britain, **2002**, 18-34.

19. Jona, E.; Scramko, T.; Gazo, J. Thermal properties of solid Nickel(II) coordination Compounds. *J. Therm. Analy. Calorim.* (JTAC), **2005**, 16, 213-229.

20. Madarász, J.; Bombicz, P.; Okuya, M.; Kaneko, S. Thermal decomposition of thiourea complexes of Cu(I), Zn(II), and Sn(II) chlorides as precursors for the spray pyrolysis deposition of sulfide thin films. *Solid State Ionics*, **2001**, 141-142, 439-446.

21. Bailey, R.A.; Tangredi, W.J. Thermal decomposition of metal complexes of thiourea. *J. Inorg. and Nucl. Chem*, **1976**, 38, 2221-2225.

22. Merdivan, M.; Karipcin, F.; Kulcu, N.; Aygun, R.S. Study of the thermal decompositions on N,-dialkyl- N'-benzoylthiourea complexes of Cu(ii), Ni(II), Pd(II), Pt(II), Cd(II), Ru(III) and Fe(III). *J. Therm. Analy. Calorim*. **1999**, 58, 551-557.

23. Siddiqi, K.S.; Nami, S.A.A.; Lutfullah, C.Y. Template synthesis of symmetrical transition metal dithiocarbamates. *J. Braz. Chem. Soc*. **2006**, 17, 107-112.

24. Onwudiwe, D.C.; Ajibade, P.A. Thermal studies of Zn(II), Cd(II) and Hg(II) complexes of some *N*-alkyl-*N*-phenyl-dithiocarbamates. *Int. J. Mol. Sci*. **2012**, 13, 9502-9513.

25. Khan, S.; Nami, S.A.A.; Siddiqi, K.S. Mononuclear indolydithiocarbamate of $SnCl_4$ and $R_2SnCl_2SnCl_2$: Spectroscopic, thermal characterization and cytotoxicity assay *in vitro*. *J. Organomet. Chem*. **2008**, 693, 1049-1057.

CHAPTER FIVE

5. SYNTHESIS OF METAL SULFIDE NANOPARTICLES USING SOME OF THE COMPLEXES AS SINGLE SOURCE PRECURSORS

5.1 Introduction

Physical and chemical properties of materials deviate from the bulk with the reduction of size to nanometer scale. Among the different classes of materials, nanostructured semiconductors have been extensively studied due to their potential applications and novel properties [1-5]. The particles unique chemical and optical properties are due to size dependent emission [6, 7]. Bawendi and Co-workers [8] pioneered the use of organometallic compounds for controlled synthesis of semiconductor nanoparticles, but the hazardous nature of the starting material call for the need for a safer synthetic route. The emergence of single source precursor route for the synthesis of semiconductor nanoparticles has attracted tremendous interest becauses it avoids the use of volatile and harzardous compounds such as alkyl metals at high temperatures and also helps to achieve homogeneous distribution of metal ions at molecular level [9-13]. This work entails the preparation of metal sulfide nanoparticles from metal organic complexes as single source precursor [14]. The single source precursor method has been used widely to prepare group II-VI semiconductor nanoparticles [15-18]. The method involves the use of single molecular precursor containing both the metal and the non metal in the same compound.

The single source precursor method has been widely used to prepare group II–VI semiconductor nanoparticles. It involves the decomposition of the precursor complex in a suitable coordinating solvent at appropriate temperature. The metal precursors containing different substituted alkyl

thiourea and ecda or tetramethylthiuram disulfide were used to prepared hexadecylamine capped ZnS, CdS and HgS nanoparticles. These metal sulfide (MS) were characterized by scanning electron microscopy (SEM), transmission electron microscopy (TEM), UV-Vis and X-ray diffraction (XRD). The choice of HDA as a preferred capping agent in this work arose from the fact that it is an effective capping agent with a good selectivity [19]. It decreases the growth rate, size of nanoparticles and improves the photoluminescence quantum efficiency by effectively passivating the surface defects while behaving as nonradioactive relaxing centre. These properties are attributed to its high electron donating ability and capping density as a result of its small stereochemical interference [20, 21].

5.2 Experimental

5.2.1 Chemicals

The precursor complexes used in the synthesis of the different metal sulfide nanoparticles were some of the complexes prepared and characterized as reported in Chapter Three. They include: [Zn(tmtd)ecda], [Cd(tmtd)ecda], [Hg(tmtd)ecda], [Zn$(dmtu)_2$ecda], [Cd$(dmtu)_2$ecda], [Hg$(detu)_2$ecda], [Cd$(mtu)_2$ecda], [Cd$(detu)_2$ecda] and [Hg$(mtu)_2$ecda]. The selected complexes were those with good yields. The other chemicals are: Hexadecylamine (HDA), tri-n-octylphosphine (TOP), toluene and absolute methanol were purchased from Aldrich. They were of analytical grade and used without further purification.

5.2.2 Characterization

5.2.2.1 UV-Vis spectroscopy

UV-Visible absorption spectra were recorded on a Pelkin Elmer Lamda 25 UV spectrometer. The solution spectra were obtained by measuring the absorption of dilute solutions in a quartz cell with a path length of 1 cm in toluene.

5.2.2.2 Photoluminescence spectroscopy

The photoluminescence spectra were taken by a Perkin Elmer LS 45 Fluorimeter at room temperature. The solvent used for the analysis was toluene and a Quartz glass of 1 cm was used as the cell.

5.2.2.3 X-ray diffraction (XRD)

The XRD patterns of nanoparticles were obtained on a Bruker D8 Advanced X-ray diffractometer with Cu–Kα radiation (λ=1.5418 Å). Measurements were taken by placing the samples on a silicon wafer slide. Baseline correction was performed on each diffraction pattern by subtracting a spline fitted to the curved background. The phase identification was carried out with the help of the standard JCPDS database.

5.2.2.4 Transmission electron microscopy (TEM)

TEM specimens were prepared by dissolving small samples of the nanoparticles in toluene and putting a drop of it on a 3-mm carbon-coated copper grid. Excess solution was removed by an

absorbent paper and the sample was dried for several hours in air before scanning.

5.2.2.5 Scanning electron microscopy (SEM)

The scanning electron microscopy (SEM) measurements were recorded on a Jeol, JSM-6390 LV microscope equipped with EDX unit. An accelerating voltage between 15-20 kV was used. The different magnifications used are indicated in the image.

5.2.2.6 Energy dispersive X-rays spectroscopy (EDX)

The EDX measurements on the synthesized nanocrystallite powders were performed using a Jeol, JSM-6390 LV scanning electron microscope fitted with an EDX unit. This gave a quantitative estimate of the composition of the nanocrystallites in atomic percentages.

5.2.3 Synthesis of the nanoparticles

The method used for the synthesis of the nanoparticles is a well described in literature [22]. In a typical experiment, about 0.4 g of the precursor complex was dissolved in TOP (10 mL). The obtained solution was then injected into 4 g of hot HDA at a temperature of 120 °C. A subsequent decrease in temperature of 20-30 °C was observed and the solution was allowed to stabilize at 120 °C. A further heating was done for 60 min and the reaction was terminated. The solution was then allowed to cool to about 70 °C, and about 100 mL methanol was added to remove the excess HDA. The flocculent precipitate formed was centrifuged and the supernatant was decanted, after which the isolated solid was dispersed in toluene. The above centrifugation

and isolation procedure was then repeated three times for the purification of the prepared metal sulfide nanoparticles.

5.3 Results and discussion

5.3.1 Characterization of nanoparticles from $[M(dmtu)_2ecda]$ (M=Zn, Cd) and $[M(detu)_2ecda]$ (M = Cd, Hg)

The synthesis of the precursor complexes were designed to allow for direct bonding between the sulfur donor atom and the metal. This is an important condition in precursor molecules since it is expected that upon thermolysis, the relatively stronger bond between the metal and sulfur (M-S) would remain while the organic part of the molecule (being held by weaker bond) is broken off. In all the complexes, respective metal sulfides remained as the final product upon their thermal decomposition. The thermolysis of the precursor complexes were carried out at 120 ºC to allow decomposition and appreciable growth under 1h. The choice of capping agent, hexadecylamine (HDA), is necessitated by its property. It has a great coverage of the coordinately unsaturated metal at the surface due to its high electron–donating ability and high capping density as a result of its small stereochemical interference [23-25].

5.3.1.1 Optical properties of MS nanoparticles from $[M(dmtu)_2ecda]$ (M=Zn, Cd) and $[M(detu)_2ecda]$ (M = Cd, Hg)

Absorption spectroscopy generally describes the characterization techniques that measure the absorption of radiation by a material, as a function of the wavelength. Optical properties of semiconductor nanoparticles (NPs) are of fundamental and practical interest. The excitation of electrons across the band gap is strongly allowed transitions, producing an abrupt increase in

absorptivity at the wavelength corresponding to the band gap energy. The band gap of group 12-16 semiconductors are in the UV-Visible region. This implies that the minimum energy required to excite an electron from the valence states to its conduction states, lies in the UV-Visible region.

The UV-Visible absorption spectra of the nanoparticle samples from [Zn(dmtu)$_2$ecda], [Cd(dmtu)$_2$ecda], [Hg(detu)$_2$ecda], [Cd(detu)$_2$ecda], [Cd(mtu)$_2$ecda] and [Hg(mtu)$_2$ecda] denoted as ZnS_1, CdS_1, HgS_1, CdS_2, CdS_3 and HgS_2 respectively are shown in Figure 5.1. It can be seen that the strongest absorption peak of the prepared ZnS_1 samples appear at around 284 nm which is fairly blue-shifted from the absorption edge (334 nm) of the bulk ZnS [26]. Semiconductor crystallites in the diameter range of a few nanometers show a three dimensional quantum size effect in their electronic structure. The absorption spectra of the cadmium sulfide nanoparticles (CdS_1, CdS_2, and CdS_3) show distinct excitonic shoulder around 429, 427 and 432 nm respectively which is characteristic of cadmium sulfide nanoparticles [27]. The blue-shift in relation to bulk CdS (515 nm) is indicative of the decrease in particle size [28]. The HgS nanoparticles showed reduced excitonic features. The band edge peaks observed around 294 and 297 nm are similar to reported spectra [29]. UV-Visible absorption spectra provide information relating to the band gap and size of the particles. Effective mass approximation (EMA) [30] has been used to calculate the particle size since it relates the change in band-gap energy to the radius of the particle. The particle size can be calculated, by using the following equation:

$$\Delta E_g = E_g^{nano} - E_g^{bulk} = \frac{h^2}{8r^2}\left(\frac{1}{m_e^*} + \frac{1}{m_h^*}\right) - \frac{1.8e^2}{4\pi\varepsilon\varepsilon_o r} \quad \ldots\ldots\ldots\ldots\ldots (1)$$

where E_g^{nano} is the band-gap energy of the nanoparticle as determined from the UV–Vis absorbance spectrum; E_g^{bulk} is the band-gap energy of the bulk at room temperature, ZnS (E_g^{bulk} = 3.6 eV and 2.42 eV for ZnS and CdS respectively; h is Planck's constant; r is the particle radius; m_e^* is the effective mass of conduction-band electron in the nanoparticle; m_h^* is the effective mass of valence-band hole in the nanoparticle, (ZnS: m_e^* = 0.42 m_0, m_h^* = 0.61 m_0; CdS: m_e^* = 0.21 m_0, m_h^* = 0.80 m_0) [31]; m_0 is the mass of electron [32]; e is the elementary charge; ϵ is the relative permittivity of the nanoparticle; and ε_0 is the permittivity of a vacuum. From the characteristic absorption spectra, the size of ZnS is 3.6 nm while the CdS nanoparticles were estimated to be about 2.52, 10.8, 5.46 and 9.76 nm in diameter.

The photoluminescence (PL) spectra of the as-prepared ZnS, CdS, and HgS were performed for the following complexes; [Zn(dmtu)$_2$ecda], [Cd(dmtu)$_2$ecda], [Hg(detu)$_2$ecda], [Cd(detu)$_2$ecda], [Cd(mtu)$_2$ecda] and [Hg(mtu)$_2$ecda] at room temperature. For the CdS nanoparticles, the excitation wavelength is at 370 nm and these are displayed in the Figure 5.1 below with the absorption spectra. Similar emmision peaks were observed from the nanoparticles of CdS1, CdS2, and CdS3 with the emission maximum at 399, 401, and 396 nm respectively which are considerably blue shifted compared to the optical absorption band edges. of the bulk CdS, indicating quantum confinement effects in the particles. The photoluminescence spectra of ZnS1, HgS and HgS were also obtained using the 370 nm wavelengths to excite these nanoparticles and they all have emission spectra of 402, 362 and 394 nm respectively as shown in Figure 5.2. The ZnS is red shifted relative to the bulk ZnS, (340 nm), [26] while the HgS and HgS are blue

shifted as compared with the bulk HgS.

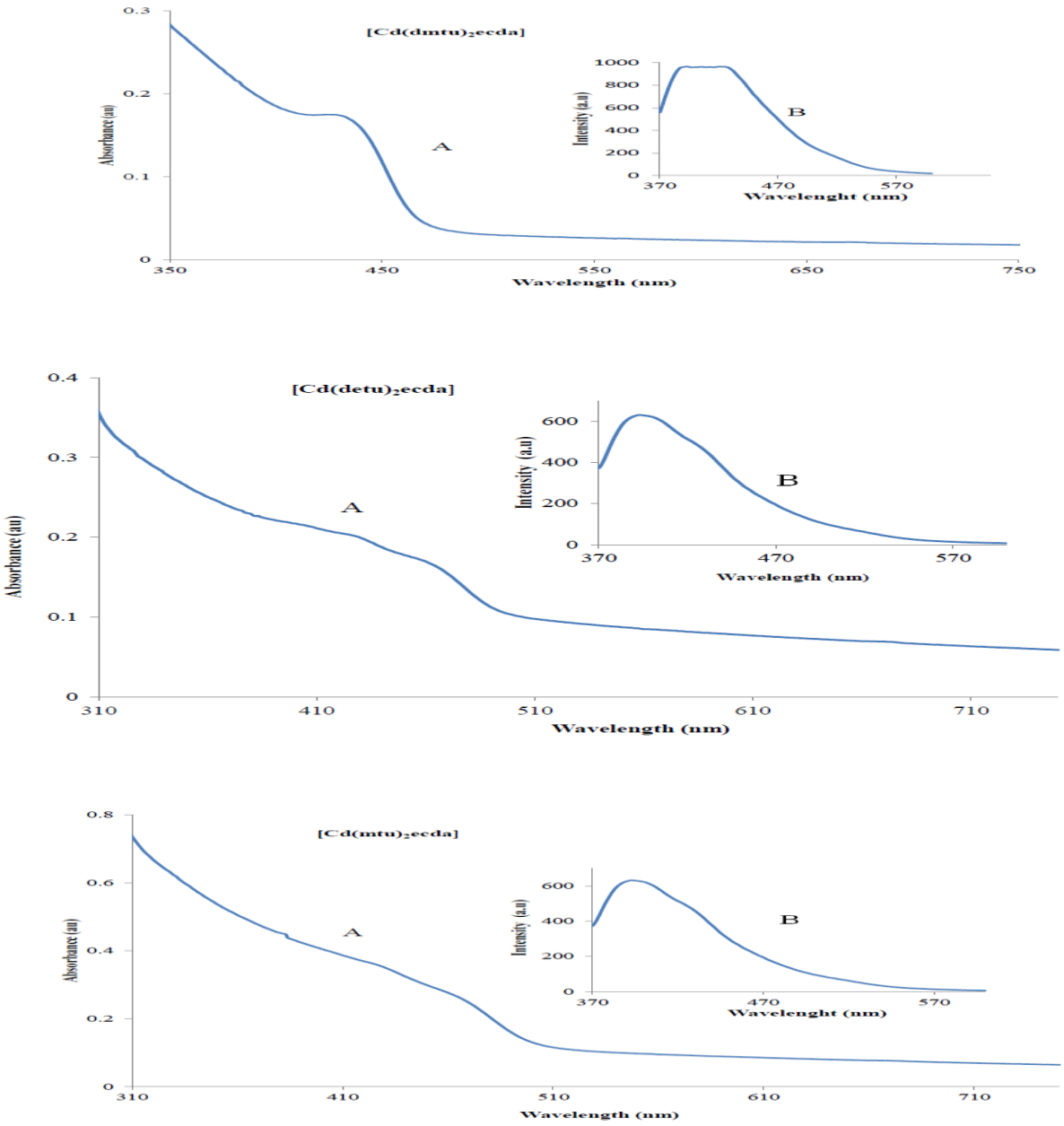

Figure 5.1: Absorption (A) and emission (B) spectra of HDA-capped CdS nanoparticles (CdS1, CdS2, and CdS3) prepared from their respective precursor complexes, [Cd(dmtu)$_2$ecda], [Cdt(detu)$_2$ecda] and [Cd(mtu)ecda] at 120 °C for 60 min.

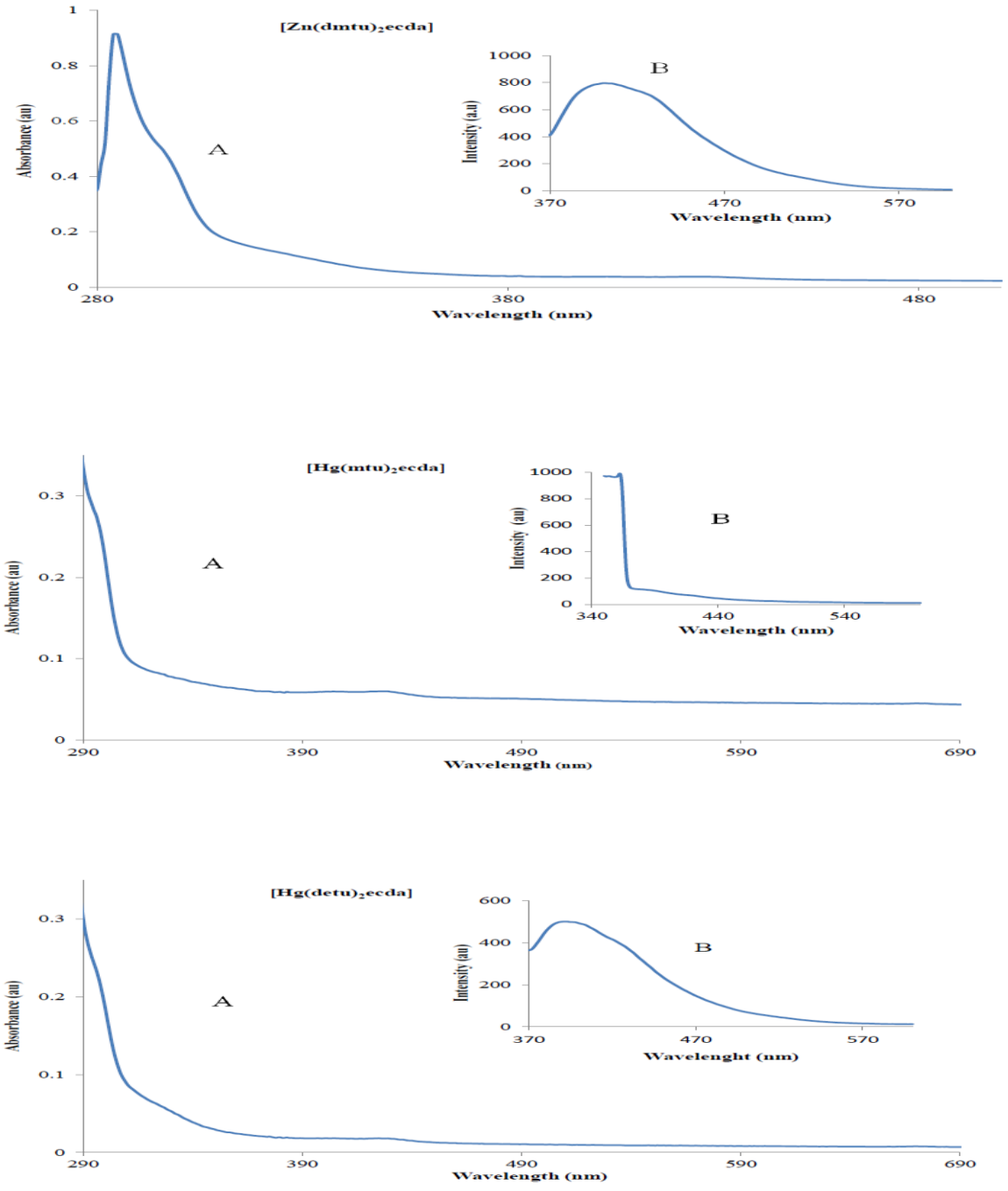

Figure 5.2: Absorption (A) and emission (B) spectra of HDA-capped ZnS, HgS1 and HgS2 nanoparticles prepared from their respective precursor complexes, [Zn(dmtu)$_2$ecda], [Hg(mtu)ecda], and [Hg(detu)$_2$ecda], at 120 °C for 60 min.

5.3.1.2 Structural properties of the metal sulfide nanoarticles

5.3.1.2.1 TEM studies of the metal sulfide nanoparticles

The TEM micrograph of the metal sulfide nanocrystal sample prepared from [Zn(dmtu)$_2$ecda], [Cd(dmtu)$_2$ecda], [Cd(detu)$_2$ecda], and [Cd(mtu)$_2$ecda] represented as (A) ZnS_1; (B) CdS_1; (C) CdS_2 and (D) CdS_3 respectively are shown in Figure 5.3. The micrograph of the ZnS_1 nanoparticles show dot shaped morphology. While the nanoparticles of samples, CdS_1 and CdS_3 have similar star shaped morphology, the morphology of the CdS_2 reveals to some extent a rice shape. The difference in the morphology of the cadmium sulfide samples could be ascribed to the variation of alkyl substituted chain of the ligand in the precursor complex. This has a significant effect on the decomposition profile of the precursor and hence influences the morphology of the metal sulphide nanoparticle [33]. In all the micrographs, the particles are monodispersed in nature.

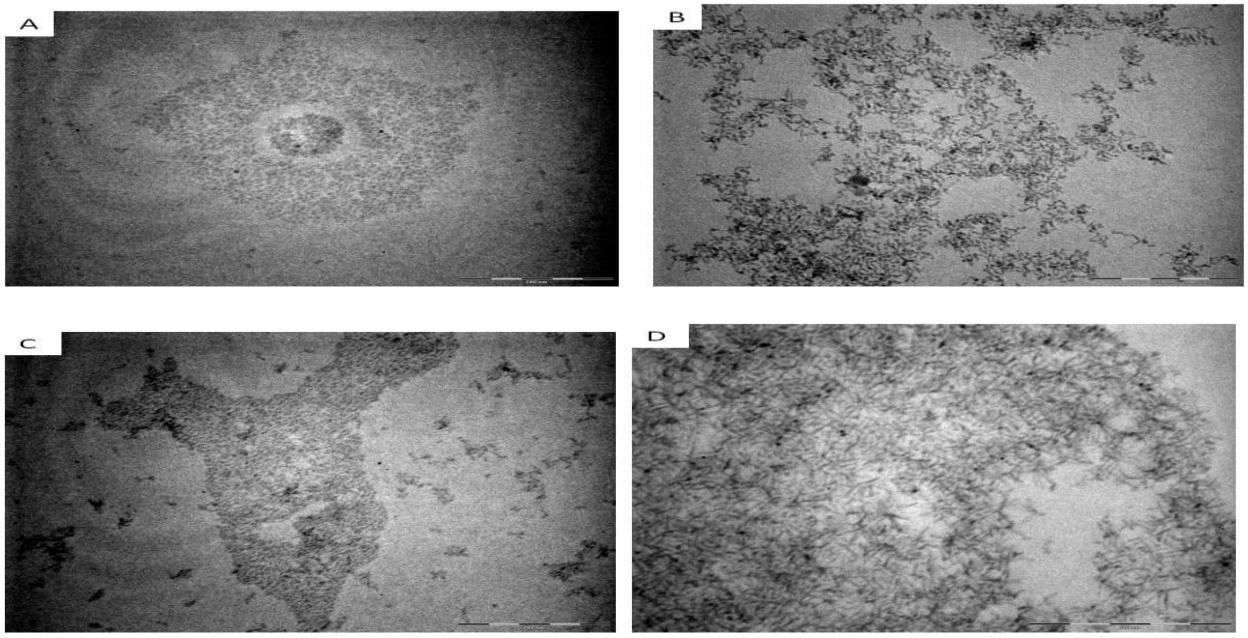

Figure 5.3: Transmission electron microgram of (A) ZnS1 (B) CdS1 (C) CdS2 and (D) CdS3 nanoparticles, prepared from their respective precursor complexes at 120 ºC.

5.3.1.2.2 TEM studies of HgS nanoparticles from [Hg(mtu)$_2$ecda], and [Hg(detu)$_2$ecda]

Figures 5.4 (A and B) shows the TEM images of the HDA-capped HgS nanoparticles, prepared from [Hg(mtu)$_2$ecda], and [Hg(detu)$_2$ecda] complexes respectively. The HgS nanoparticles, under the synthetic conditions, produced spherical and oval shapes, with some intercalated, the sizes ranging from 10 to 25 nm and with a good uniform size distribution throughout the sample. A slight stacking of nanoparticles is observed which is usually common with HgS nanoparticles

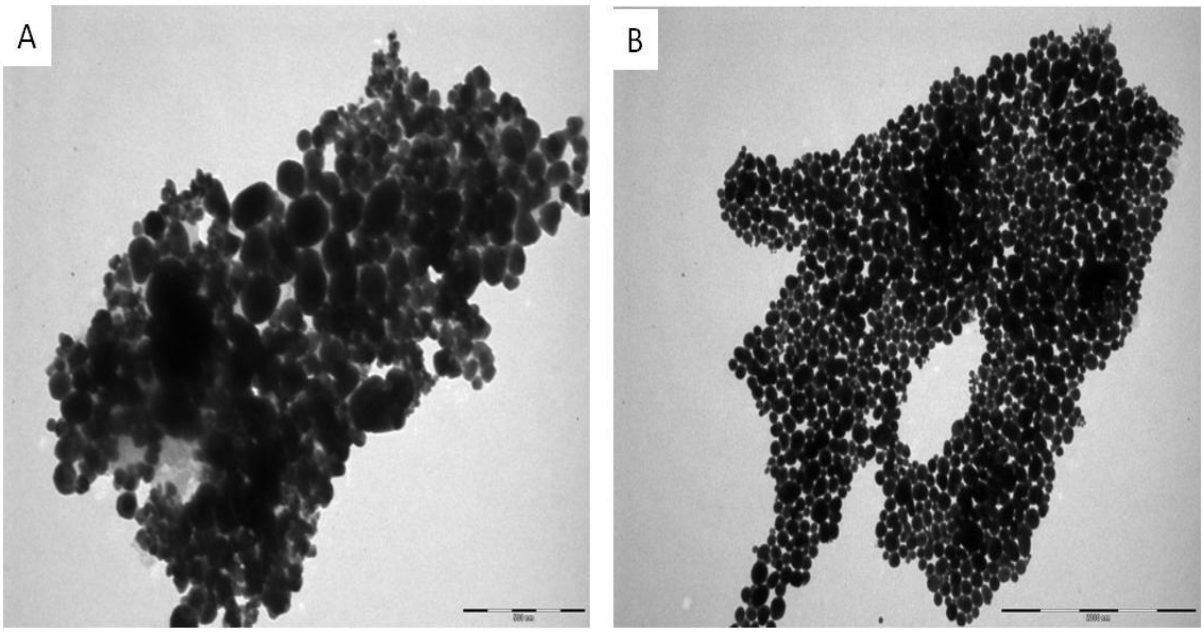

Figure 5.4: TEM micrograms of HDA-capped HgS nanoparticles, prepared from (A) [Hg(mtu)$_2$ecda], (B) [Hg(detu)$_2$ecda] at 120 °C for 60 minutes.

5.3.1.2.3 SEM studies of the metal sulfides (MS) nanoparticles from [Zn(dmtu)$_2$ecda], [Cd(dmtu)$_2$ecda], [Cd(detu)$_2$ecda], [Cd(mtu)$_2$ecda], [Hg(mtu)$_2$ecda], and [Hg(detu)$_2$ecda]

Figure 5.5-5.10 shows the SEM micrographs and EDX spectra of the as prepared ZnS_1, CdS_1, HgS_1, CdS_2, CdS_3 and HgS_2 nanoparticles. The morphology of the particles is nearly spherical.

The smaller particles can be easily seen clinging to the surface of the big particles. Because SEM can often only determine the particle size of secondary particles, it is assumed that the secondary particles of metal sulfides consist of the primary particles which are in the nanometer range, as estimated by effective mass approximation (EMA). The EDX spectra show peaks corresponding to the respective metal and sulfur with only a noticeable contaminant being phosphorus and presumably from tri-n-octylphosphine (TOP) in which the precursor metal complexes were dispersed prior to injection into hot hexadexylamine (HDA).

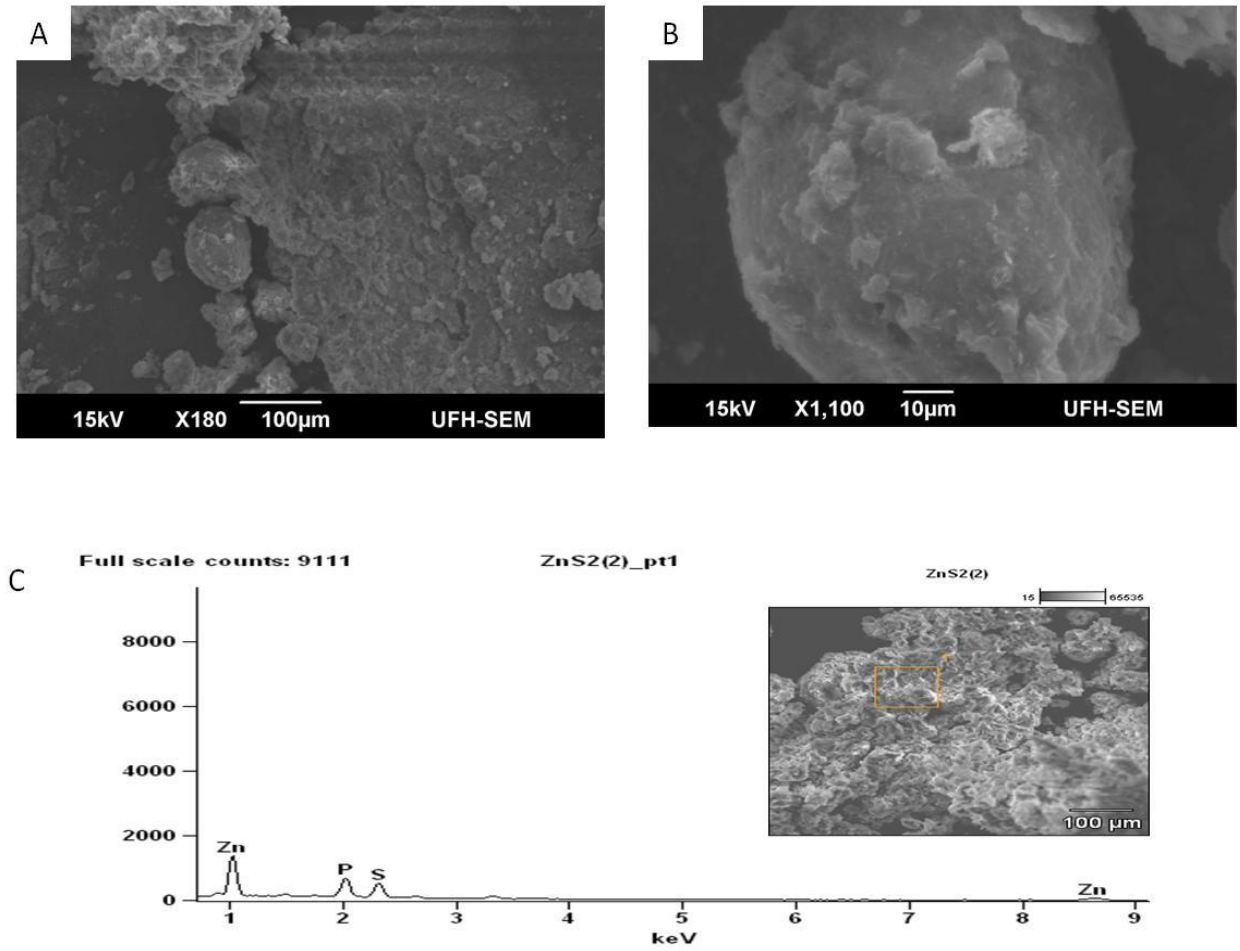

Figure 5.5: SEM micrograph of CdS nanoparticles from [Cd(dmtu)$_2$ecda] complex, at 120 ºC at (A) low magnification, (B) high magnification (C) EDX spectrum of the CdS sample.

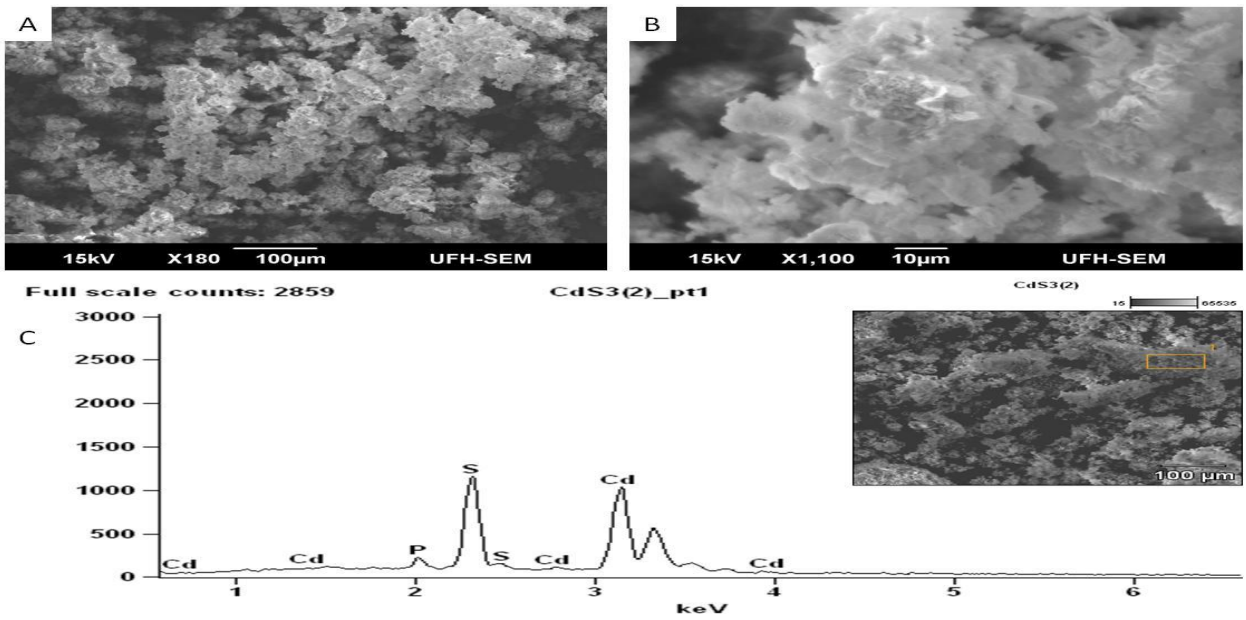

Figure 5.6: SEM micrograph of CdS nanoparticles from [Cd(detu)$_2$ecda] complex, at 120 ºC at (A) low magnification, (B) high magnification (C) EDX spectrum of the CdS sample**.**

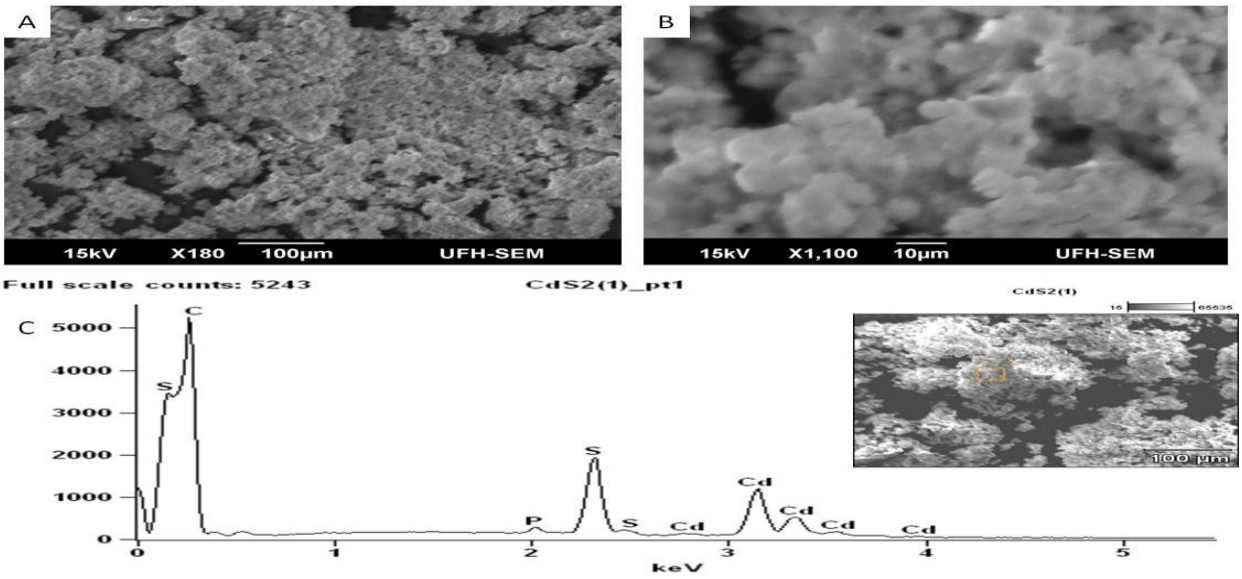

Figure 5.7: SEM micrograph of CdS nanoparticles from [Cd(mtu)$_2$ecda] complex, at 120 ºC at (A) low magnification, (B) high magnification (C) EDX spectrum of the CdS sample.

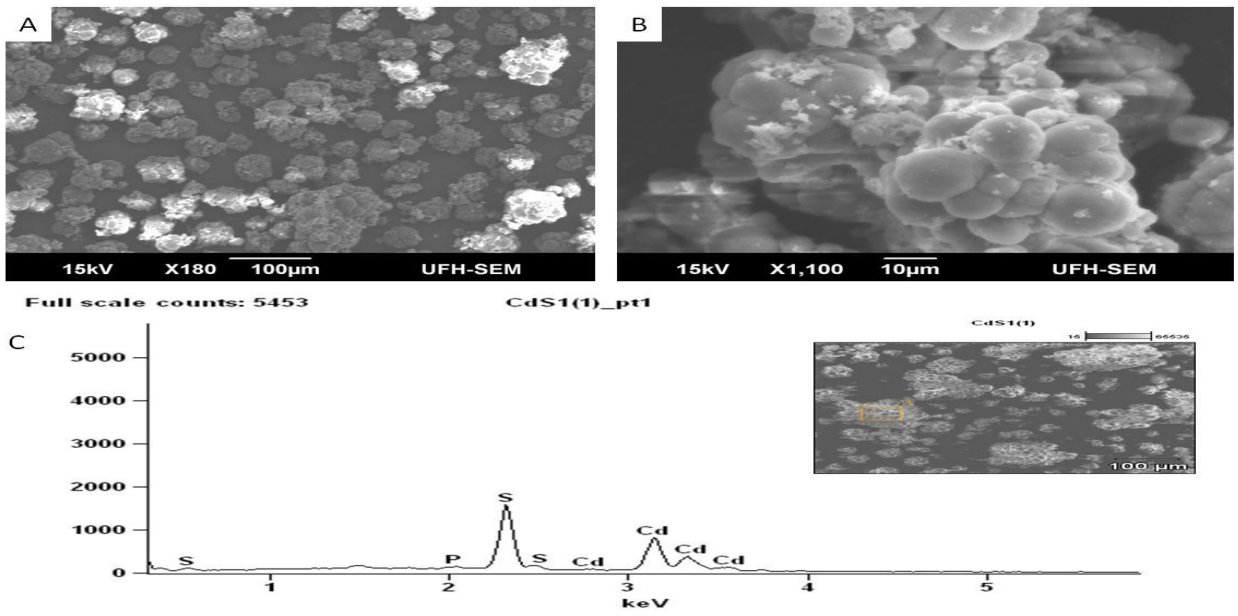

Fig 5.8: SEM micrograph of CdS nanoparticles from [Cd(mtu)$_2$ecda] complex, at 120 ºC at (A) low magnification, (B) high magnification (C) EDX spectrum of the CdS sample.

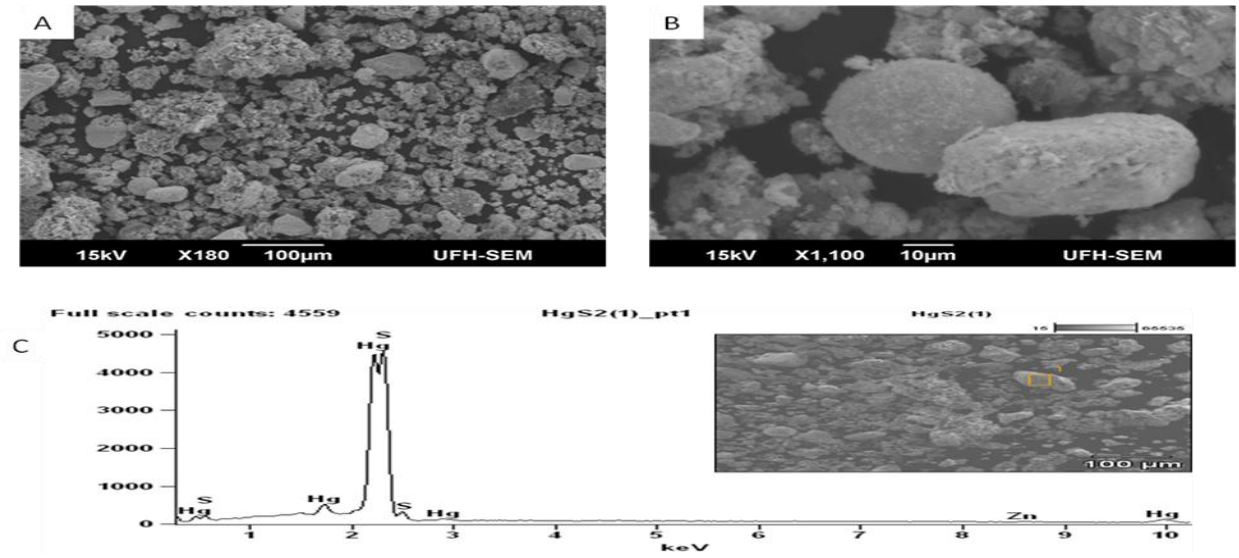

Figure 5.9: SEM micrograph of CdS nanoparticles from [Hg(mtu)$_2$ecda] complex, at 120 ºC at (A) low magnification, (B) high magnification (C) EDX spectrum of the HgS sample**.**

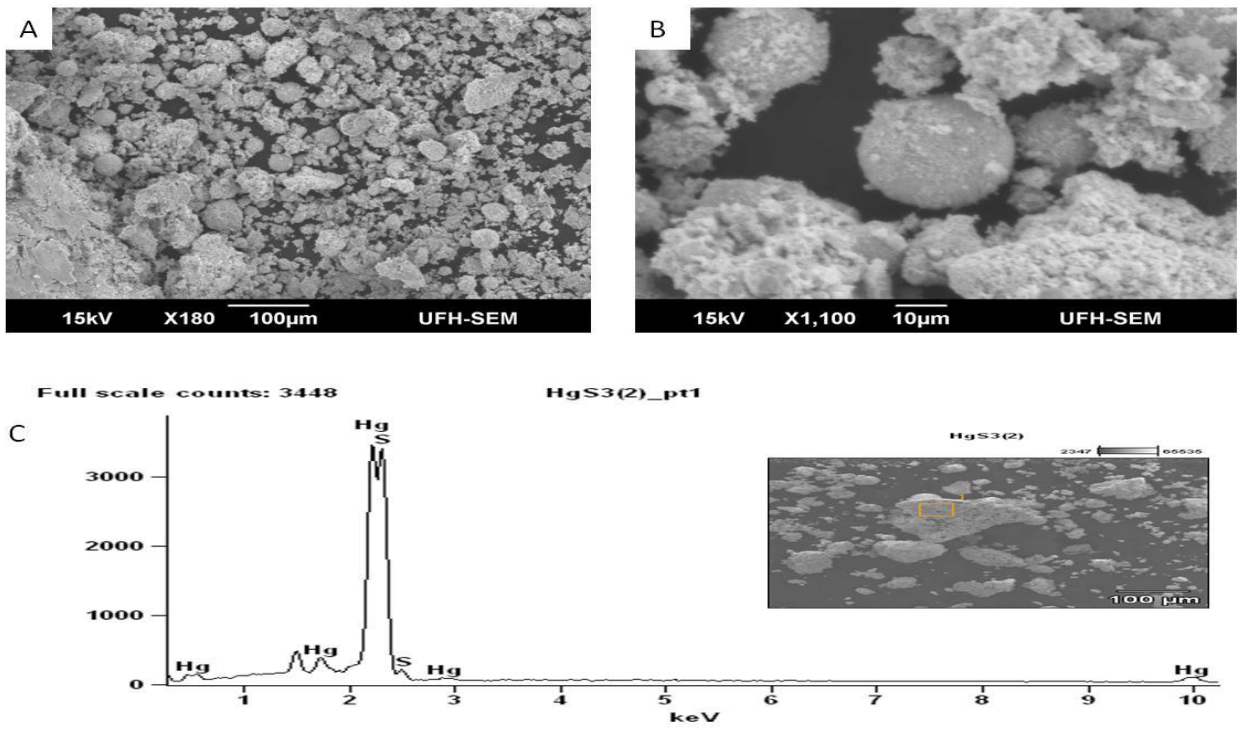

Figure 5.10: SEM micrograph of HgS nanoparticles from [Hg(detu)$_2$ecda] complex, at 120 °C at (A) low magnification, (B) high magnification (C) EDX spectrum of the HgS sample.

The presence of phosphorous peak in the EDX spectra could be due to the tri-n-octylphosphine used during the synthesis of the nanoparticles.

5.4 XRD studies of nanoparticles prepared from complexes

5.4.1 XRD studies of ZnS1 nanoparticles

XRD measurement of HDA-capped ZnS1 nanoparticles was carried out at room temperature as shown in Figure 5.11. The four peaks with 2θ values of 26.36, 35.48, 41.22, 44.22, 52.18 can be

indexed to the following planes (1 1 1) , (2 0 0), (2 2 0) and (3 1 1). A single phase sphalerite crystal structure (Zinc blende) is exhibited here.

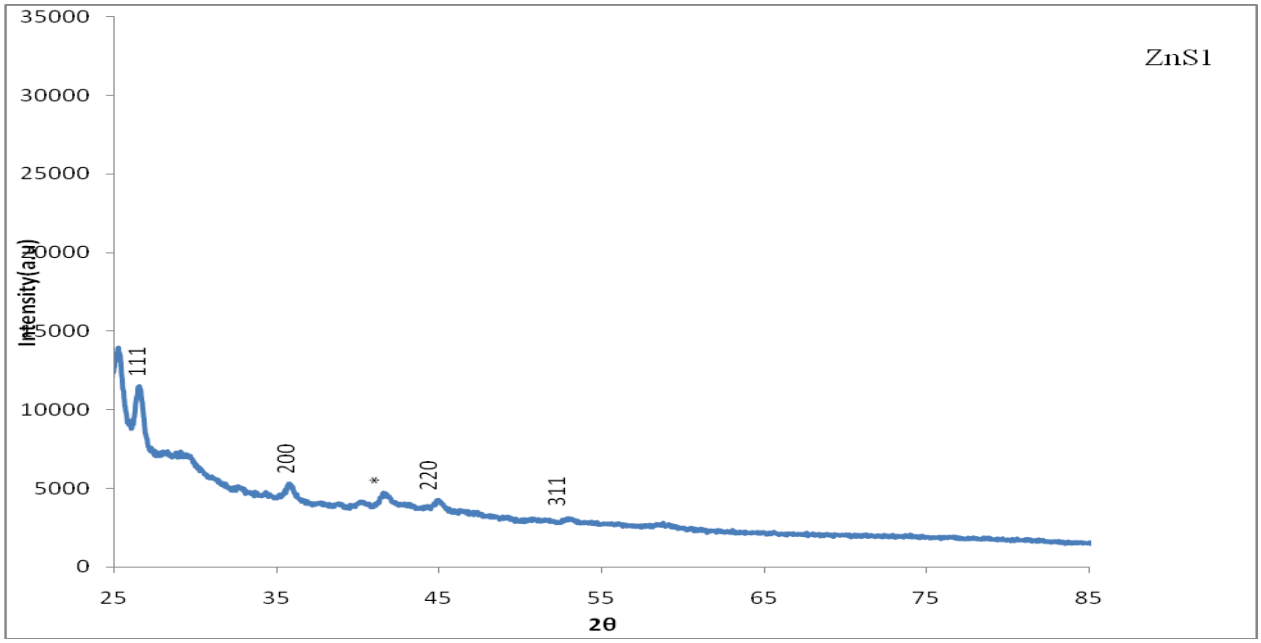

Figure 5.11: XRD pattern of HDA capped ZnS nanoparticles synthesized from [Zn(dmtu)$_2$ecda].

5.4.2 XRD studies of CDS nanoparticles

The XRD spectra of CdS1, CdS2 and CdS3 are shown in Figures 5.12-5.14 respectively. They all exhibit broad peaks at 2θ values [26.63, 43.96, 51.99, 70.98] for CdS1; [26.63, 44.09, 51.96, 71.43] for CdS2; and [26.78, 44.43, 52.36, 70.79] for CdS3 respectively and these values can be indexed to the following miller indeces ; (1 1 1), (2 2 0), (3 1 1) and (331) of cubic phase CdS. Their broad peaks are due to finite size effects or can be ascribed to the the particle sizes in nanometer range. The planes can be compared with the JCPDS file card (05-0566).

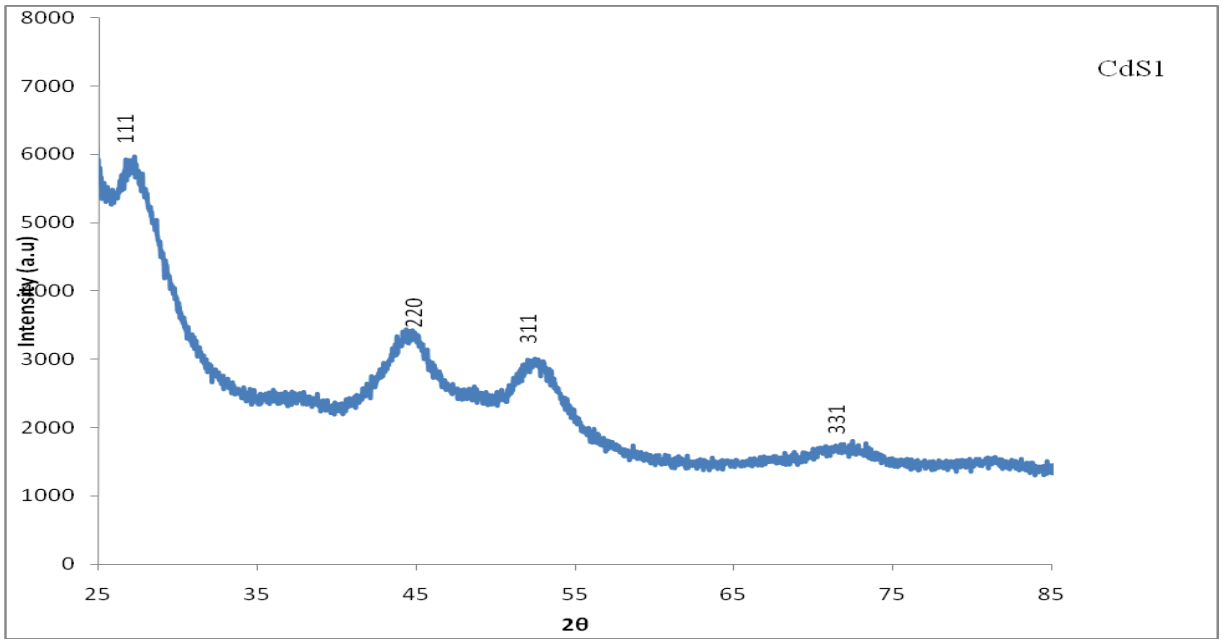

Figure 5.12: XRD pattern of HDA-capped CdS nanoparticles synthesized from [Cd(dmtu)$_2$ecda].

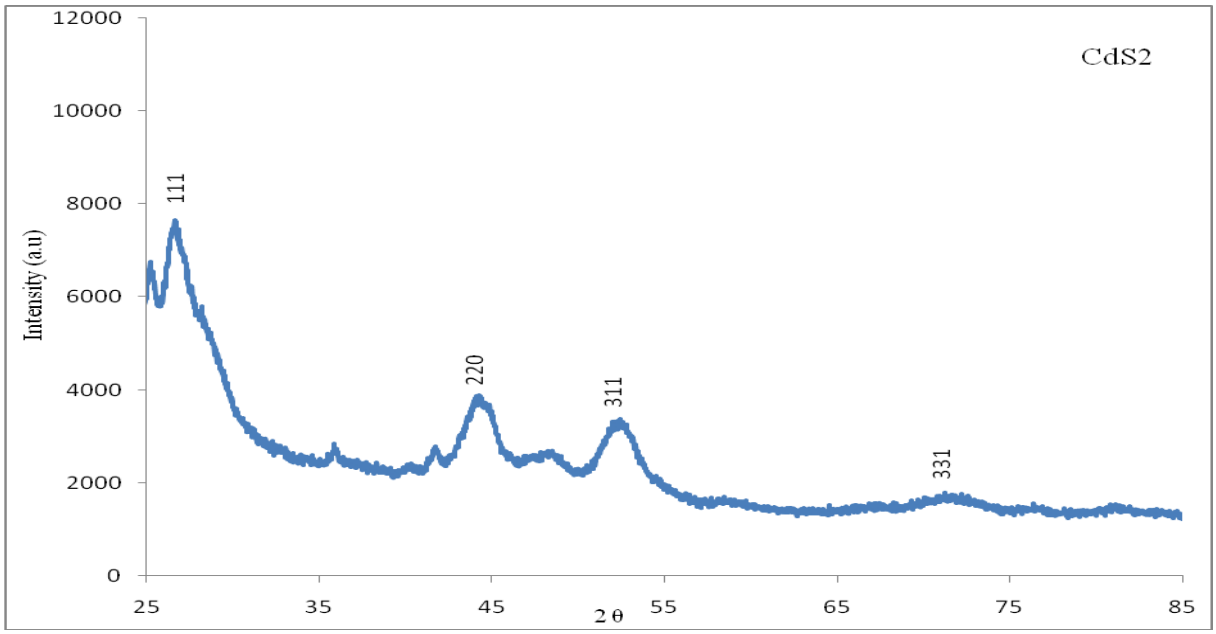

Figure 5.13: XRD pattern of HDA-capped CdS nanoparticles synthesized from [Cd(detu)$_2$ecda].

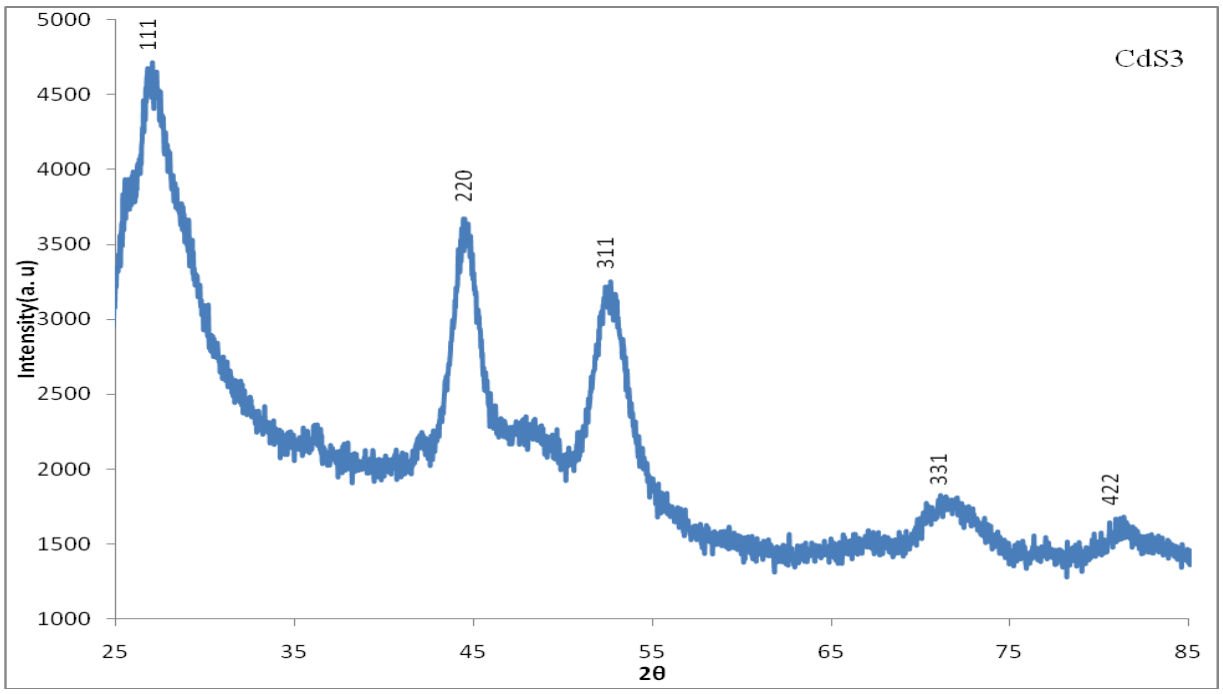

Figure 5.14: XRD pattern of HDA-capped CdS nanoparticles synthesized from $[Cd(mtu)_2ecda]$.

5.4.3 XRD studies of HgS1 and HgS2 nanoparticles

XRD measurement of HgS1 and HgS2 were carried out at room temperature and are shown below in Figure 5.15-5.16. The 2θ values are 26.39, 30.56, 43.77, 51.81, 54.25, 63.50, 70.01 80.33 and 26.60, 30.75, 43.93, 51.99, 54.44, 63.63, 70.19, 72.24, 80.4 for HgS1 and Hg2 respectively. This pattern clearly shows the characteristic of cubic HgS (β-HgS) which is also known as metacinnabar mercury sulfide [34] and the diffraction rings can be indexed to (1 1 1), (2 0 0), (2 2 0), (3 1 1), (2 2 2), (4 0 0), (3 3 1), (4 2 2), and (3 3 3).

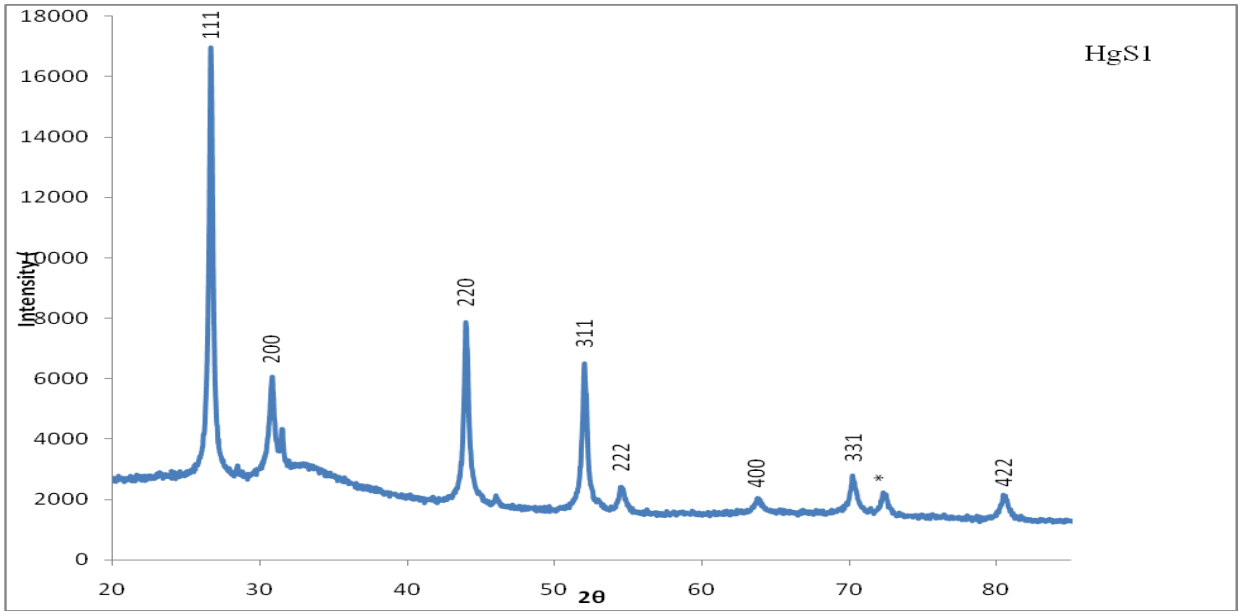

Figure 5.15: XRD pattern of HDA-capped HgS nanoparticles synthesized from [Hg(detu)$_2$ecda].

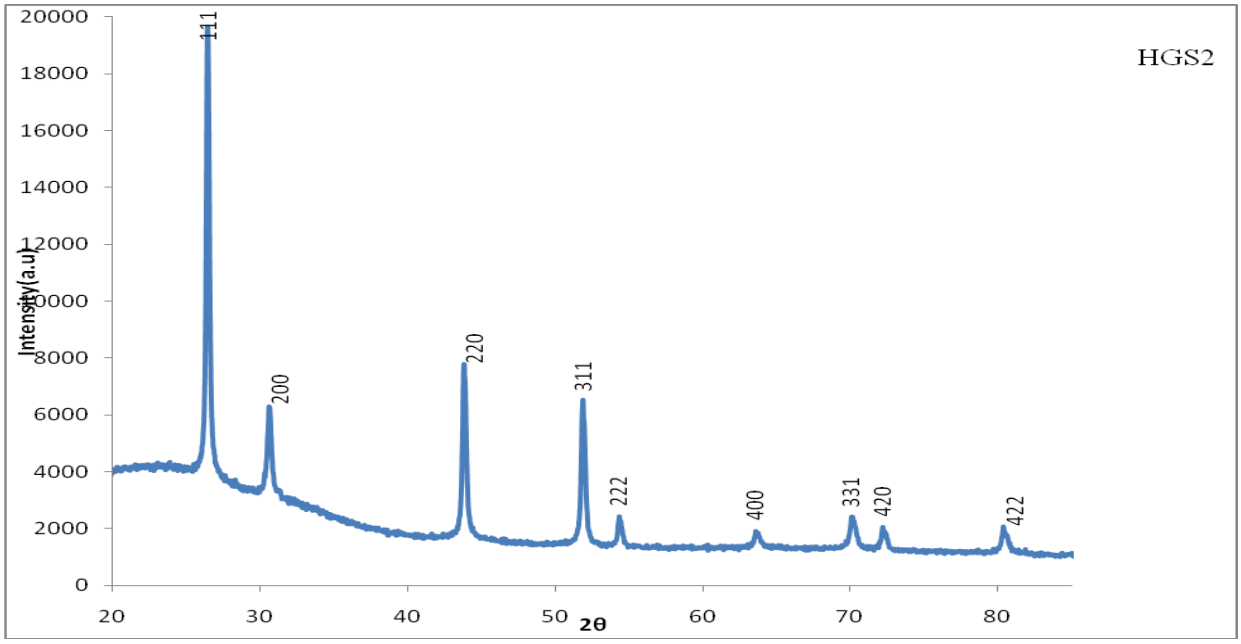

Figure 5:16: XRD pattern of HDA-capped HgS nanoparticles synthesized from [Hg(mtu)$_2$ecda].

5.4.4 Metal sulfides (MS) nanoparticles from tetramethylthiuram disulfide,

[M(tmtd)ecda], (M = Zn, Cd, Hg)

Zn(II), Cd(II) and Hg(II) complexes obtained from tetramethylthiuram disulfide and 1-ethoxylcarbonyl-1-cyanoethylene-2,2-dithiolate were thermolysed in hexadexylamine (HDA) to synthesize HDA capped ZnS, CdS and HgS nanoparticles. The nanoparticles were characterized with UV-Visible, photoluminescence, scanning electron microscopy, transmission electron microscopy and X-ray diffraction techniques.

5.4.4.1 Optical properties of metal sulfide nanoparticles from [M(tmtd)ecda] (M = Zn, Cd and Hg)

The UV-Vis absorption spectra (Figure 5.16) showed that the absorption peaks of analysed ZnS, CdS and HgS particles are at 288, 439 and 296 nm respectively, a relative blue-shift to the band gap of the bulk which are at 340, 515 and 563 nm respectively [35-36]. The peaks positions can be related with the mean diameter of the particles, smaller diameter meaning lower wavelength. The results showed the effect of quantum confinement (quantum size effect, QSE). QSE in direct gap semiconductors nanocrystals are well understood and have been reported [37]. The absorption shift represents a change in band gap along with exciton features, which can be used as a measure of particle size and size distribution. The calculated gap for the ZnS, CdS, and HgS particles are E_g = 3.78, 2.82, and 3.89 eV respectively.

In semiconductor nanoparticles, the position of absorption band edge can be taken as an

indicative of their sizes. The approach has proven very useful since the result obtained from this method has not been affected by the presence of aggregates. The electronic coupling between particles in an aggregate is sufficiently weak so that the resultant spectrum is determined by the primary particles only [38].

Brus equation [39] was used to calculate the particle size from the absorption edge. From the characteristic absorption spectra, the size of CdS and ZnS nanoparticles were estimated to be about 5.68 and 7.88 nm in diameter. The photoluminescence spectra of the as–prepared ZnS, CdS and HgS from the complexes of [Zn(tmtd)ecda], [Cd(tmtd)ecda], [Hg(tmtd)ecda] were recorded at room temperature at an excitation wavelength of 370 nm and they exhibit emission peak maxima at 398, 394 and 393 nm respectively. The ZnS is red shifted with respect to the bulk and CdS and HgS are blue shifted compared with their bulk materials as shown in Figure 5.17.

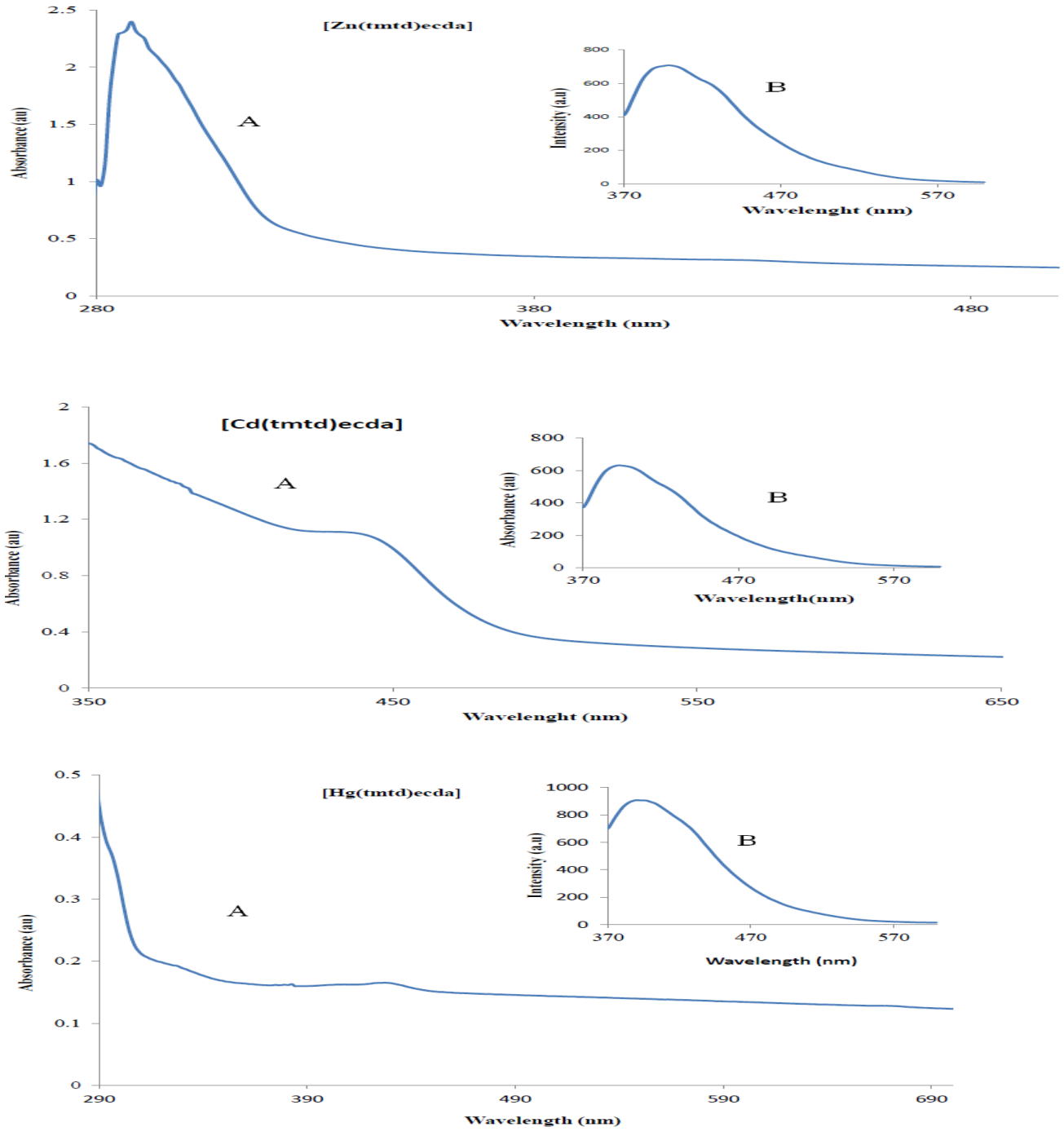

Figure 5.17: (A)Absorption and (B) emission spectra of HDA-capped ZnS, CdS, and HgS nanoparticles, synthesized from metal complexes of [M(tmtd)ecda] where (M=Zn, Cd, and Hg) at 120 ºC for 60 minutes.

5.4.4.2 Structural properties of metal sulfide nanoparticles from [M(tmtd)ecda].

5.4.4.3 TEM studies of metal sulfide nanoparticles from [M(tmtd)ecda] (M = Zn, Cd, Hg).

TEM images of the ZnS, CdS and HgS nanoparticles synthesized from [M(tmtd)ecda] (M = Zn, Cd, Hg) respectively are presented in Figure 5.18 (A, B and C). It is observed that the particles of the ZnS are dot shaped and the size is rather evenly distributed. The CdS particles display a rice-shaped morphology while in the HgS sample, agglomerated oval shaped particles were observed. TEM showed that the product was composed of 40% of isolated particles and 60% of agglomerated particles. The average size of HgS nanoparticles is in about 60 nm. It is hard to determine the exact dimension of HgS particles by only observing the TEM image because the extremely small particles aggregate to secondary particles [40].

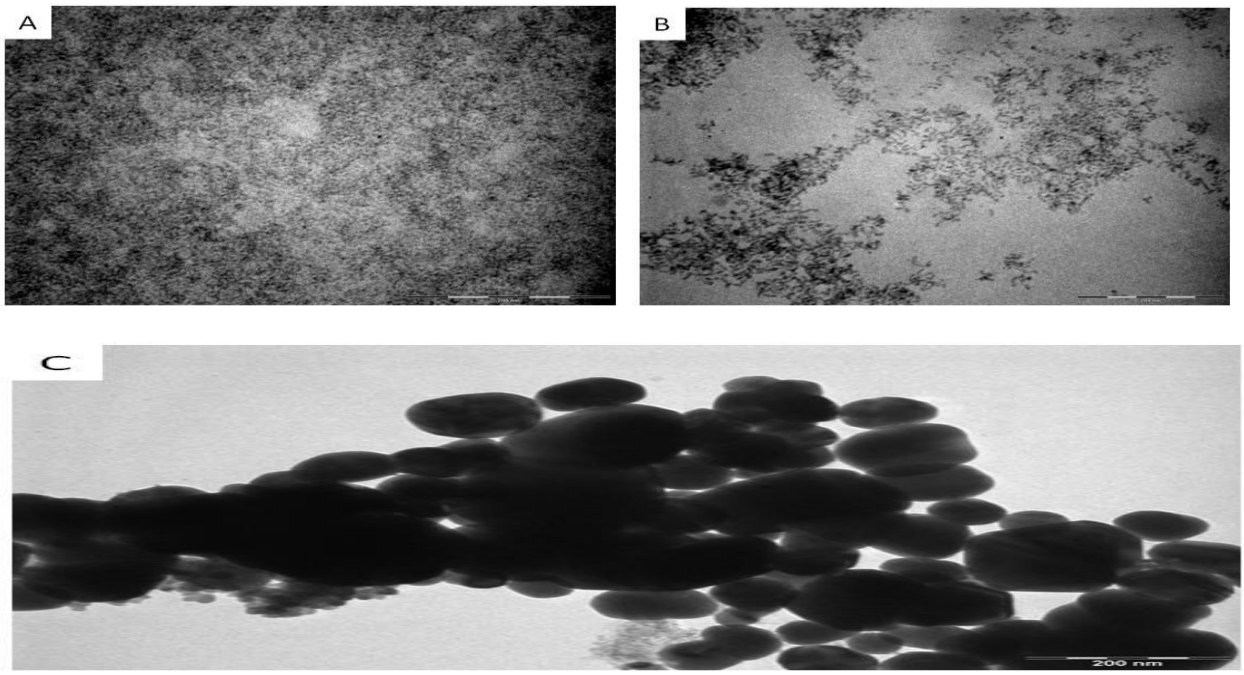

Figure 5.18: TEM images of (A), ZnS; (B), CdS; and (C), HgS nanoparticles, prepared from their respective precursor complexes at 120 ºC.

5.4.4.4 SEM studies of metal sulfide nanoparticles from [Mtmtdecda] (M = Zn, Cd and Hg).

The microstructure of the nanocrystals was examined by scanning electron microscopy (SEM) and the elemental composition of the nanoparticles formed were confirmed by energy dispersive X-ray (EDX) analysis as shown in Figure 5.19-5.21. It can be seen that the surface of the particles appears smooth and spherical like.

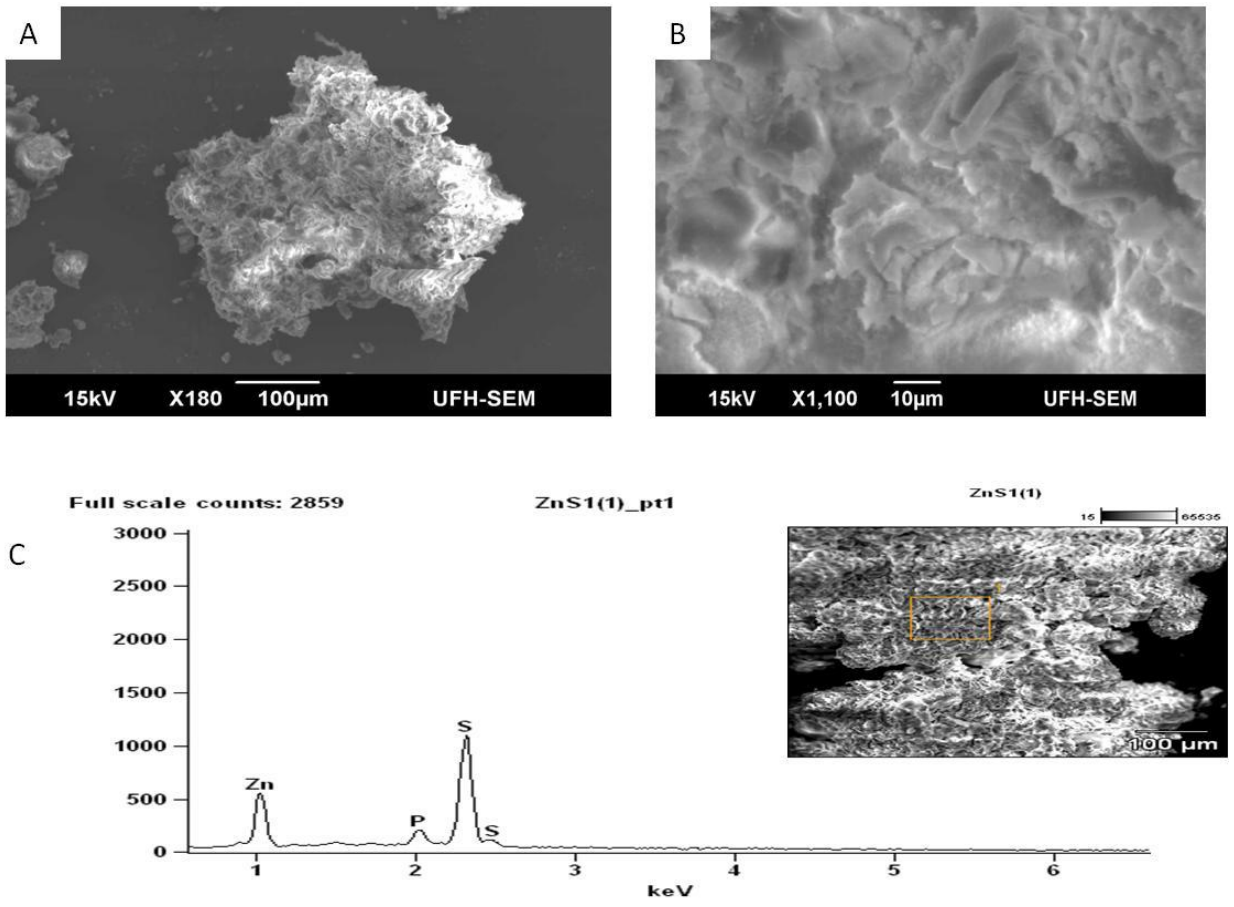

Figure 5.19: SEM micrograph of ZnS nanoparticles from [Zn(tmtd)ecda] complex, at 120 ºC at (A) low magnification, (B) high magnification (C) EDX spectrum of the ZnS sample.

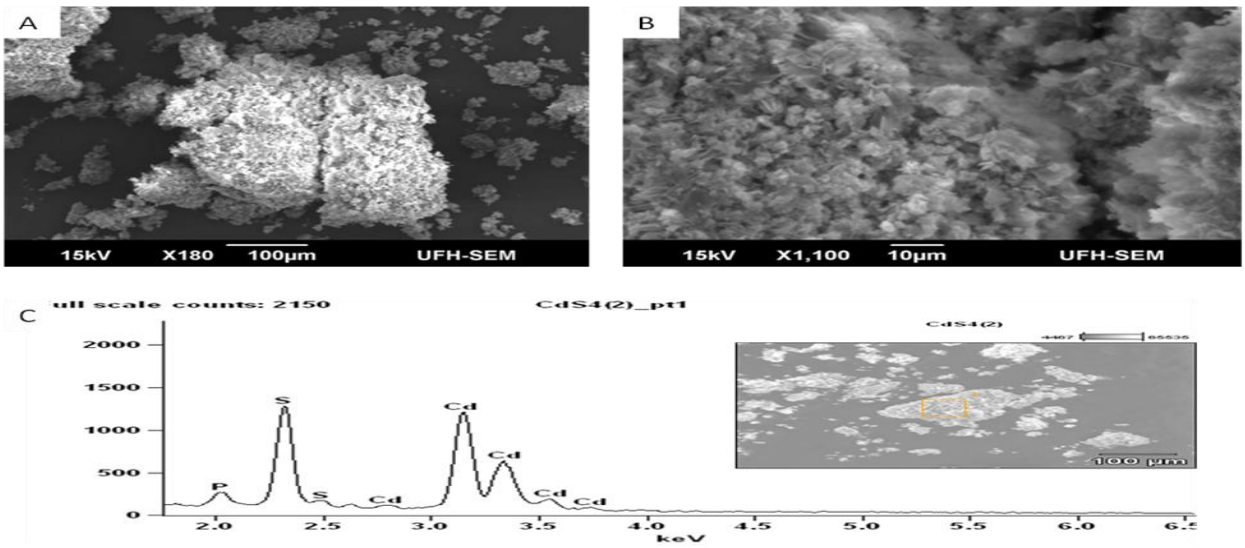

Figure 5.20: SEM micrograph of CdS nanoparticles from [Cd(tmtd)ecda] complex, at 120 ºC at (A) low magnification, (B) high magnification and (C) EDX spectrum of the CdS sample.

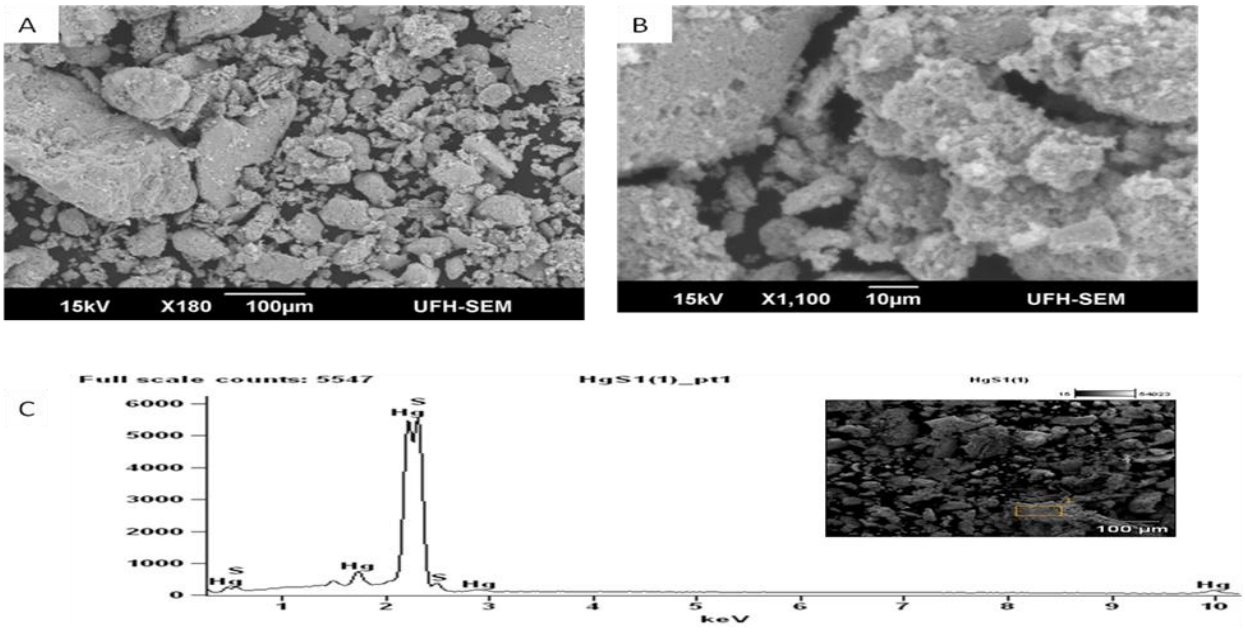

Figure 5.21: SEM micrograph of HgS nanoparticles from [Hg(tmtd)ecda] complex, at 120 ºC at (a) low magnification, (b) high magnification (c) EDX spectrum of the HgS sample.

5.4.4.5 XRD studies of ZnS, CdS, HgS nanoparticles prepared from [M(tmtd)ecda]

The powder XRD pattern of as prepared HDA-capped ZnS, CdS and HgS nanoparticles samples are shown in Figures 5.22-5.24 below. These XRD patterns of the ZnS, CdS, HgS exhibited different structures.

5.4.4.6 XRD Studies of ZnS2 nanoparticle from [Zn(tmtd)ecda].

For ZnS2, the three peaks with 2θ values 26.78, 44.43 and 52.36 correspond to the presence of hexagonal ZnS. The indicators are the peak value 26.78 plane which correspond to (1 0 1) and is in good agreement with Joint committee of powder diffraction standard (JCPDS) data belonging to hexagonal ZnS [41] and the presence of 52.36 which suggest the hexagonal phase of ZnS [42]. The broad peaks are due to finite size effects which also indicate that the particles sizes are in nanometer range.

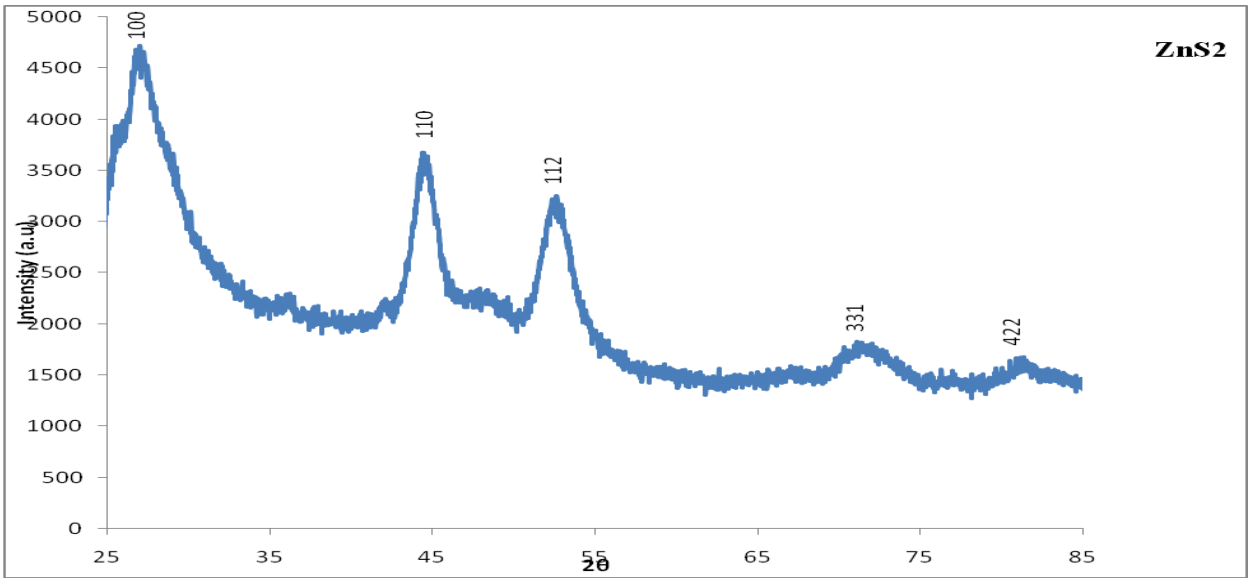

Fig 5.22: XRD pattern of HDA-capped ZnS nanoparticles synthesized from [Zn(tmtd)ecda].

5.4.4.7 XRD Studies of CdS4 nanoparticle from [Cd(tmtd)ecda].

The XRD pattern of CdS of this complex, [Cd(tmtd)ecda], is shown in Figure 5.23 and it exhibits a single phase sphalerite crystal structure [43]. The 2θ values are: 26.9, 36.16, 43.6, and 51.83 and they can be indexed to the following planes: (1 1 1), (2 0 0), (2 2 0) and (3 1 1) of the cubic phase β-CdS (JCPDS 80-0019). The peak broadening of XRD pattern indicates that small nanocrystals are present.

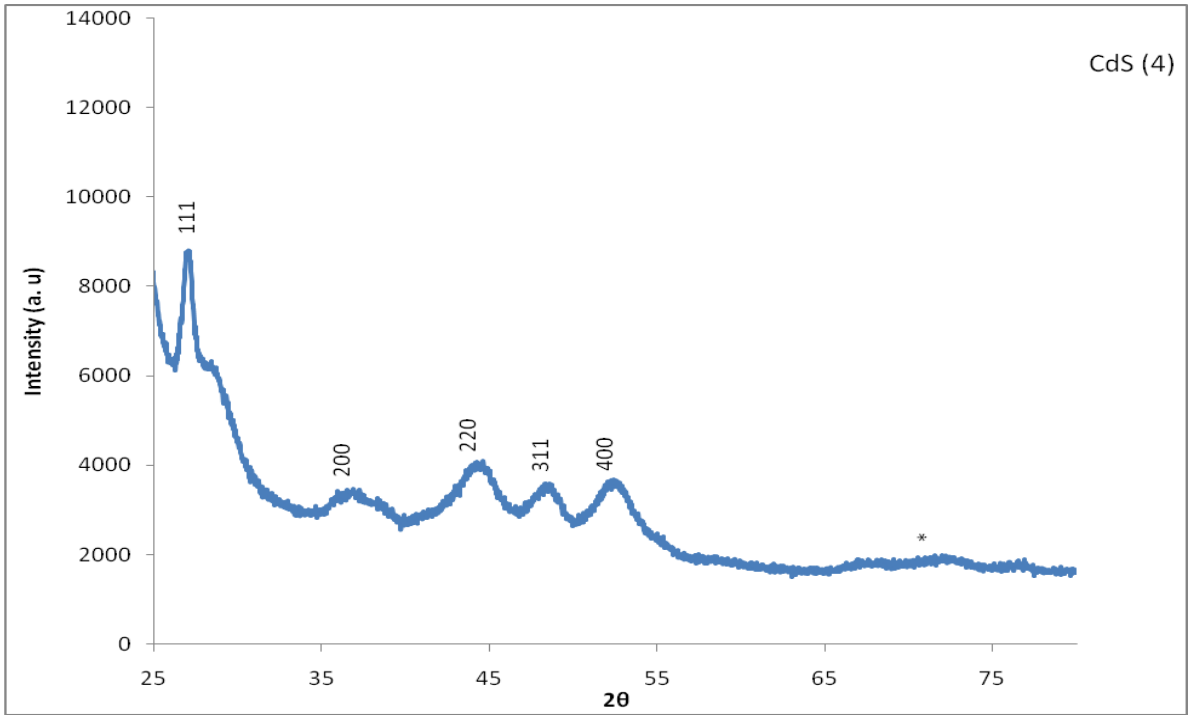

Figure 5.23: XRD pattern of HDA-capped CdS nanoparticles synthesized from [Cd(tmtd)ecda].

5.4.4.8 XRD Studies of HgS3 nanoparticle from [Hg(tmtd)ecda]

The listed peaks as observed in the XRD pattern of HgS of this complex at 2θ are: 26.49, 30.64, 43.85, 51.89 and 54.33. They match the peaks of known metaccinabar [34]. The peaks are

intense and all orient along the planes (1 1 1), (2 0 0), (2 2 0), (3 1 1), (4 0 0). All these peaks are to be indexed to face-centered cubic HgS and they are relatively broad which show that the particles are in nano size dimension.

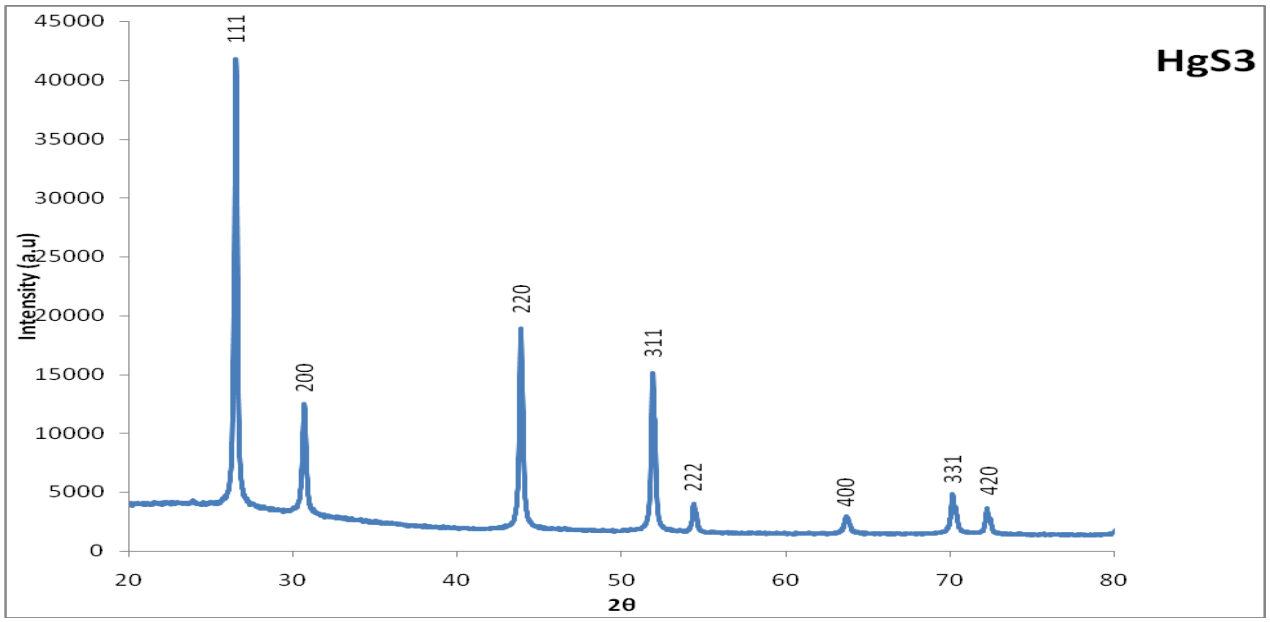

Figure 5.24: XRD pattern of HDA-capped HgS nanoparticles, synthesized from [Hg(tmtd)ecda].

References

1. Malik, M.A.; Revaprasadu, N.; O'Brien, P. Air-stable single source precursors for the synthesis of chalcogenide semiconductor nanoparticles. *Chem. Mater*. **2001**, 13, 913-920.

2. Trindade, T.; O'Brien, P.; Zhang, X.M. Synthesis of CdS and CdSe nanocrystallites using a novel single-molecule precursors approach. *Chem. Mater*. **1997**, 9, 523-530.

3. Green, M.; Prince, P.; Gardener, M.; Steed J. mercury(II) *N*,*N*′-Methyl-phenylethyl-dithiocarbamate and its use as a precursor for the room-temperature solution deposition of β-HgS thin films. *Adv. Mater*. **2004**, 16, 994-1030.

4. Matchett, M.A.; Viano, A.M.; Adolphi, N.L.; Stoddard, R.D.; Buhro, W.E.; Conradi, M.S.; Gibbons, P.C. A sol-gel route to crystalline cadmium phosphide nanoclusters. *Chem. Mater*. **1992**, 4, 508-511.

5. Lazell, M.; O'Brien, P. A novel single source precursor route to self capping CdS quantum dots. *Chem. Commun*. **1999**, 2041-2042.

6. Peng, X.G.; Wilson, T.E.; Alivisatos, A.P.; Schultz, P.G. Improved efficiencies in light emitting diodes made with CdSe(CdS) core/shell type nanocrystals and a semiconducting polymer. *J. Appl. Phys*. **1997**, 82, 5837-5842.

7. Coe, S.; Woo, W-K.; Bawendi, M.; Bulovic, V. Electroluminescence from single monolayers of nanocrystals in molecular organic device**s**. *Nature*, **2002**, 420, 800-803.

8. Murray, C.B.; Norri, D.J; Bawendi, M.G. Synthesis and character of nearly monodisperse CdE (E=S, Se, Te). *J. Am. Chem. Soc*. **1993**, 115, 8706-8715.

9. Pickett, N.L.; O'Brien, P. Synthesis of semiconductor nanoparticles using single source

precursor methods. *Chem*. *Rec*. **2001**, 461-479.

10. Rees Jr, W.S.; Krå uter, G. Preparation and characterization of several group 12 element (Zn, Cd)-*bis*(thiolate) complexes and evaluation of their potential as precursors for 12–16 semiconducting materials. *J*. *Mater*. *Res*. **1996**, 11, 3005-3016.

11. Thurston, J.H.; Ely, T.O.; Trahan, D.; Whitmire, K.H. Nanostructured Bimetallic Oxide Ion-Conducting Ceramics from Single Source Molecular Precursors. *Chem. Mater*. **2003**, 15, 4407-4416.

12. Pohl, I.A.M.; Westin, L.G.; Kritikos, M. Preparation, Structure, and properties of a new giant manganese oxo-alkoxide wheel, $[Mn_{19}O_{12}(OC_2H_4OCH_3)_{14}(HOC_2H_4OCH_3)_{10}]\cdot HOC_2H_4OCH_3$. *Eur*. *J*. *Chem*. **2001**, 7, 3438-3445.

13. Thurston, J.H.; Whitmire, K.H. Molecular Precursors for Ferroelectric Materials: Synthesis and Characterization of $Bi_2M_2(\mu\text{-}O)(sal)_4(Hsal)_4(OEt)_2$ and $BiM_4(\mu\text{-}O)_4(sal)_4(Hsal)_3(O^iPr)_4$ (sal = $O_2CC_6H_4O$, Hsal = $O_2CC_6H_4OH$) (M = Nb, Ta). *Inorg*. *Chem*. **2003**, 42, 2014-2023.

14. Ajibade, P.A.; Onwudiwe, D.C.; Moloto, M.J. Synthesis of hexadecylamine capped nanoparticles using group 12 complexes of N-alkyl-N-phenyl dithiocarbamate as single-source precursors. *Polyhedron*, **2011**, 30, 246-252.

15. Onwudiwe, D.C.; Ajibade, P.A. Zn(II), Cd(II) and Hg(II) complexes of N-methyl-N-phenyl dithiocarbamate as single source precursors for the synthesis of metal sulfide nanoparticles. *Mater*. *Lett*. **2011**, 65, 3258-3261.

16. Afzaal, M.; Malik, M.A.; O'Brien, P. Indium sulfide nanorods from single-source precursor.

Chem. Comm. **2004**, 334-335.

17. Kedarnath, G.; Kumbhare, L.B.; Jain, V.K.; Phadnis, P.P.; Nethaji, M. Group 12 metal monoselenocarboxylates: synthesis, characterization, structure and their transformation to metal selenide (MSe; M = Zn, Cd, Hg) nanoparticles. *Dalton Trans*. **2006**, 2714-2718.

18. Kedarnath, G.; Dey, S.; Jain,V.K.; Dey, G.K.; Varghese, B. 2-(N,N-Dimethylamino)ethylselenolates of cadmium(II): Syntheses, structure of $[Cd3(OAc)_2(SeCH_2CH_2NMe_2)_4]$ and their use as single source precursors for the preparation of CdSe nanoparticles. *Polyhedron*, **2006**, 25 2383-2391

19. Jin, M.; Guannan, H.; Zhang, H.; Zeng, J.; Xie, Z.; Xia, Y. Shape-controlled synthesis of copper nanocrystals in an aqueous solution with glucose as a reducing agent and hexadecylamine as a capping agent. *Ang*. *Chem*. *Inter*. *Ed*. **2011**, 50, 10560-10564.

20. Mthethwa, T.; Pullabhotla, V.S.R.; Mdluli, P.S., Wesley-Smith, J.; Revaprasadu N. Synthesis of hexadecylamine capped CdS nanoparticles using heterocyclic cadmium dithiocarbamates as single source precursors. *Polyhedron*, **2009**, 28, 2977-2982.

21. Park, J.Y.; Aliaga, C.; Renzas, R.J.; Lee, H.; Somorjai, G. The role of organic capping agents layers of platinum nanoparticles in catalytic activity of CO oxidation. *Catal*. *lett*. **2009**, 129, 1- 6.

22. Arl, D.; Dalmasso, S.; Bozzolo, N.; Zhang, Y.; Gaumet, J.J.; Laurenti, P.J. Physical and chemical analyses on single source precursor growth CdSe semiconductor nanomaterials. *Mater. Chem. Phy*. **2000**, 124, 129-133.

23. Leppert, V.J.; Risbud, S.H.; Fendorf, M.J. High-resolution electron microscopy and microanalysis of ZnSe quantum dots in glass matrices. *Phil. Mag. Lett*. **1997**, 75, 29-34.

24. Reiss, P.; Quemard, G.; Carayon, S.; Bluese, J.; Chandezon, F.; Pron, A. ZnSe nanocrystals of high colour purity: Preparation and spectroscopic studies. *Mater*. *Chem*. *Phys*. **2004**, 84,10-13.

25. Selim, M.S.; Seoudi, R.; Shabaka, A.A. Polymer based films embedded with high content of ZnSe nanoparticles. *Mater*. *Lett*. **2005**, 59, 2650-2654.

26. Nanda, J.; Sapra, S.; Sarma, D.D.; Chandrasekharan, N.; Hodes, G. Size-selected zinc sulfide nanocrystallites: Synthesis, structure, and optical studies. *Chem*. *Mater*. **2002**, 12, 1018-1024.

27. Bai, H.J.; Zhang, Z.M.; Guo, Y.; Yang, G.E. Biosynthesis of cadmium sulfide nanoparticlesby photosynthetic bacteria rhodopseudomonas palustris. *Colloids surf*. *B* **2009**, 70, 142-146.

28. Nyamen, L.D.; Pullabhotla, V.S.R.; Nejo, A.A.; Ndifon, P.; Revaprasadu, N. Heterocyclic dithiocarbamates: precursors for shape controlled growth of CdS nanoparticles. *New J.Chem*. **2011**, 35, 1133-1139.

29. Onwudiwe, D.C; Ajibade, P.A. ZnS, CdS, HgS nanoparticles via alkyl-phenyl dithiocarbamate as single source precursors. *Int. J. Mol. Sci.* **2011**, 12, 5538-5551.

30. Yoffea, A. D. Low-dimensional system: quantum size effects and electronic properties of semiconductor microcrystallites (zero-dimension system) and some quasi-two dimensional systems. *Adv*. *Phys*. **1993**, 42, 173-175.

31. Lippens, P.E.; Lannoo, M. Optical property of II-VI nanocrystal. *Semicon. Sci*. *Technol*. **1991**, 6A, 157.

32. Winkelmann, K.; Noviello. T.; Brooks, S. Preparation of CdS nanoparticle for first year undergraduate, *J. Chem. Educ*. **2007**, 84, 709-710.

33. Memon, A.A.; Afzaal, M.; Malik, A.; Nguyen, C.Q.; O'Brien, P.; Raftery, J. The N-alkyldithiocarbamato complexes [M(S_2CNHR_2)] (M=Cd(II), Zn(II); R = C_2H_5, C_4H_9, C_6H_{13}, $C_{12}H_{25}$); their synthesis, thermal decomposition and use to prepare nanoparticles and nanorods of CdS. *Dalton Trans*. **2006**, 4499-4505.

34. Downs, R.T.; Hall-Wallace, M. The American mineralogist crystal structure database. *Am*. *Miner*. **2003**, 88, 247-250.

35. Xu, W.; Wang, Y.; Xu, R.; Liang S.; Zhang, G.; Yin, D. Synthesis and florescence analysis of nanocrystal of CdS nanocrystals. *J*. *Mater*. *Sci*. **2007**, 42, 6942-6945.

36. John, R.; Sasi, S.F. Optical structural and morphological studies of bean-like ZnS nanostructures by aqueous chemical method. *Chalcogenide Lett*. **2010**, 7, 269-273.

37. Zhao, X.W.; Komuro, S.; Fujita, S.; Isshiki, H.; Aoyagi, Y.; Sugano, T. Size control of Si nanocrystallites formed in amorphous Si matrix by Er-doping. *Mat*. *Sci*. *Eng*.: *B*, **1998**, 51, 154-157.

38. Mehta, S.K.; Kumar, S.; Gradzielski, M. Growth, stability, optical and photoluminescent properties of aqueous colloidal ZnS nanoparticles in relation to surfactant molecular structure. *J*. *Colloid Interf*. *Sci*. **2011**, 360, 497-507.

39. Brus, L.E. Electron-electron and electron-hole interactions in small semiconductor crystallites: The size dependence of the lowest excited electronic state. *J*. *Chem*. *Phys*. **1984**, 80(9), 4403-4409.

40. Yin, Y.; Xu, X.; Ge, X.; Lu, Y.; Zhang, Z. Synthesis and characterization of ZnS colloidal particles via γ-Radiation. *Radiat. Phys. Chem*. **1999**, 55, 353-356.

41. Patra, J.; Mondal, S.; Mitra, P. Preparation of ZnS and SnS nanoparticles by modified Silar techniques. *J. Phys. Sci*. **2009**, 13, 227-234.

42. Thomas, P.J.; Christian, P.; Daniel, S.; Li, Y.; Wang, Y.S.; O'Brien, P. Nanorods of CoP, CdS, and ZnS. *Pure Appl. Chem*. **2006**, 78, 1651-1665.

43. R. Banerjee, R. Jayakrishnan, P. Ayyub. J. Effect of size-induced structural transformation on band gap. *Phys. Condens. Matter* 12, **2000** 10647-10654

CHAPTER SIX

6. SUMMARY, CONCLUSION AND RECOMMENDATION

6.1 Summary of the work

Zn(II), Cd(II) and Hg(II) complexes of 1-ethoxylcarbonyl-1-cyanoethylene-2,2- dithiolate with substituted thiourea (methylthiourea, diethylthiourea, dimethylthiourea) or tetramethylthiuram disulfide was synthesized and characterized. The metal complexes were synthesized by the reaction of respective metal salts with the different ligands to isolate air stable metal complexes. The complexes were characterized by elemental analyses, IR and NMR spectroscopy. Spectroscopic analysis confirmed that the metal complexes coordinate the metal ions through the sulfur atom to form a metal chalcogenide suitable as single source precursor for the preparation of metal sulfide semiconductor nanoparticles.

Due to the poor solubility of the complexes in most common solvents, efforts to recrystallize the complexes did not yield good results. The thermal decomposition of some of the complexes was studied using thermograimetry analysis. The product of the decomposition were further analysed by sanning electron microscopy (SEM) and energy dispersive X-ray spectroscopy (EDX). The thermal decomposition behavior most of the complexes proceed in one major decomposition step to give the respective metal sulfides. A second step at higher temperatures led to the oxidation of the sulfides. The thermal decomposition studies showed the formation of the metal oxides at higher temperature except for Hg complexes where volatilization took place. The TGA residues were not enough for SEM/EDX analysis. In total, twelve metals complexes were isolated and

nine metal complexes were used as single source precursors for the preparation of HDA-capped metal sulfide nanoparticles.

The dissertation is divided into six chapters. Chapter one is all about the introduction and a literature review of related work carried out on nanoparticles. This includes a brief discussion of several synthetic routes to the preparation of nanoparticles stating their advantages and drawbacks. This chapter also includes the aim and objective of this work.

Chapter two gives a short description of the various characterization techniques employed in validating nanoparticles preparation were reported. Such techniques include; UV-Vis, X-ray diffraction, transmission and scanning electron microscopy which are necessary tools for the measurement of optical, structural and morphological properties of nanoparticles. Chapter three contains the experimental for this work. Detailed synthetic methods for the preparation of the K_2ecda ligand and the Zn(II), Cd(II) and Hg(II) complexes were given.

Chapter four contains the characterization of the metal complexes using elemental analysis, IR, and ^{1}H and ^{13}C NMR spectroscopy. Based on the elemental analysis of the complexes, four coordinates square planar geometries were proposed for the metal complexes. The complexes are generally insoluble in most common solvents and hence hindered to a great extent efforts to recrystallize the complexes. Chapter four also contains thermal studies of the complexes. The

TGA/DTG studies showed that the complexes decomposed neatly to give metal sulfide as the product of the decomposition. In all the complexes, decomposition profile was in two stages, the DTG of the metal complexes were sharp and these also reveal the purity of the precursors and showed the peak decomposition temperature which was above the temperature at which the precursors were thermolysed. The final products of the thermal decomposition were studied using SEM and the decomposition determined by EDX.

Chapter five detailed the preparation and characterization of HDA-capped metal sulfide nanoparticles using some of the metal complexes as single source precursors. The complexes were dissolved in tri-n-octylphosphine and injected into hot HDA to obtain the HDA capped nanoparticles. The nanoparticles were investigated by UV-Vis spectroscopy, powder X-ray diffraction and TEM.

6.2 Conclusion

This work reports the synthesis and characterization of some group II-VI metal complexes of mixed ligands of 1-ethoxylcarbonyl-1-cyanoethylene-2,2-dithiolate as metal sulfide for semiconductor nanoparticle via single source precursor routes. The metal complexes synthesized were predicted to give metal sulfide, (MS), (M= Zn, Cd, Hg and S = S) with the thermolysis of hexadecylamine (HDA) capped metal sulphide nanoparticles at a temperature of 120 ^{0}C. The EDX spectra showed that the nanoparticles consist of mainly the metal sulfide of the precursor complexes except on few instances where there was phophosrus which is an impurity from the

tri–n-octyl phosphine (TOP) in which the precursor complexes were dissolved prior to injection in HDA. There were broadening of peaks in the powder X-ray diffraction spectra which is indication of the presence of small nanocrystal nature of the particles. The TEM analysis of the CdS showed star shaped morphology and sometimes rice shaped. That of the HgS gave oval and spherical shapes.

This dissertation contain twelve metal complexes of which nine are made up of substituted thioureas and 1-ethoxylcarbony-1-cyanoethylene-2,2-ditiolate ($ecda^{2-}$) and 3 comprise tetramethylthiuram disulphide and $ecda^{2-}$ ligand. All these complexes were characterized but nine were thermolysed and characterized for the synthesis of MS semiconductor nanoparticle. The characterization techniques of these precursor revealed that these complexes are potential single source precursor molecules for the preparation of II-VI nanoparticles.

6.3 Recommendations

Single source precursor method employed in the synthesis of semiconductor nanoparticles despite all its merits has its drawbacks. It's a complex method and it depends on factors which affects its monomer concentration, nucleation and nanocrystal growth. The preparation of nanoparticles from the precursor complex to the characterization techniques have been discussed in this dissertation. There is the need to examine the variation of thermodynamic parameters like concentration, temperature and time as they affect the nanocrystalite size of the synthesized particles. These investigations will offer insights about how these parameters affect the structural

properties of the crystallite particles.

In this work, the metal salt used in the synthesis of the precursor complexes were; $ZnCl_2$, $CdCl_2$ and $HgCl_2$. It might be necessary to embark on the use of copper and cobalt in addition to the ones employed here with the hope that it might be possible to recrystallize them. Prepation of the bipyridine adducts of the complexes in this work might also give compounds where suitable crystals for single X-ray crystallography may be obtained. This might also solve the problem associated with solubility encounter in this work. These adducts can then be used as precursors for thin films deposition.